IDA PAPER P-2207

THEORETICAL CONSIDERATIONS FOR THE MEASUREMENT OF RADIATION FROM SHOCK HEATED AIR

Deborah A. Levin
Richard T. Loda

DTIC
ELECTE
FEB 1 2 1992
S D D

February 1991

Prepared for
Strategic Defense Initiative Organization
(Innovative Science and Technology Office)

92-03413

INSTITUTE FOR DEFENSE ANALYSES
1801 N. Beauregard Street, Alexandria, Virginia 22311-1772

REPORT DOCUMENTATION PAGE

Public Reporting burden for this collection of information is estimated to average 1 hour per response, including the time for reviewing instructions, searching existing data sources, gathering and maintaining the data needed, and completing and reviewing the collection of information. Send comments regarding this burden estimate or any other aspect of this collection of information, including suggestions for reducing this burden, to Washington Headquarters Services, Directorate for Information Operations and Reports, 1215 Jefferson Davis Highway, Suite 1204, Arlington, VA 22202-4302, and to the Office of Management and Budget, Paperwork Reduction Project (0704-0188), Washington, DC 20503.

1. AGENCY USE ONLY (Leave blank)	2. REPORT DATE February 1991	3. REPORT TYPE AND DATES COVERED FINAL--April 1988 to October 1990

4. TITLE AND SUBTITLE

Theoretical Considerations for the Measurement of Radiation from Shock Heated Air

5. FUNDING NUMBERS

C - MDA 903 89 C 0003

T - T-R2-597.04

6. AUTHOR(S)

Deborah A. Levin, Richard T. Loda

7. PERFORMING ORGANIZATION NAME(S) AND ADDRESS(ES)

Institute for Defense Analyses
1801 N. Beauregard Street
Alexandria, VA 22311

8. PERFORMING ORGANIZATION REPORT NUMBER

IDA Paper P-2207

9. SPONSORING/MONITORING AGENCY NAME(S) AND ADDRESS(ES)

Strategic Defense Initiative Organization
Washington, DC 20301-7100

10. SPONSORING/MONITORING AGENCY REPORT NUMBER

11. SUPPLEMENTARY NOTES

12a. DISTRIBUTION/AVAILABILITY STATEMENT

Approved for public release; distribution unlimited.

12b. DISTRIBUTION CODE

13. ABSTRACT (Maximum 200 words)

Application of hypersonic computational fluid dynamics models for the characterizations and prediction of shock heated air-induced UV radiation from boost phase vehicles is examined. Specifically, velocities of 3-4 km/sec and altitudes of 40-80 km have been considered. Important modeling aspects, such as chemical kinetics, electronic excitation/de-excitation mechanisms, and the existence of equilibrium versus nonequilibrium conditions in the flow are examined. Comparison of theoretical flowfield predictions with recent shock tube data, for the purposes of flowfield code validation, is also shown. Flowfield properties, and in-band radiance values in the 2500Å wavelength region, in the vicinity of the stagnation stream line, are presented for a three inch hemisphere. These results were generated to provide input for instrument designers involved in an upcoming rocket experiment to measure UV radiation produced in bowshock.

14. SUBJECT TERMS

bow shock, hypersonic, computational fluid dynamics, ultraviolet instrumentation

15. NUMBER OF PAGES
108

16. PRICE CODE

17. SECURITY CLASSIFICATION OF REPORT UNCLASSIFIED	18. SECURITY CLASSIFICATION OF THIS PAGE UNCLASSIFIED	19. SECURITY CLASSIFICATION OF ABSTRACT UNCLASSIFIED	20. LIMITATION OF ABSTRACT SAR

IDA PAPER P-2207

THEORETICAL CONSIDERATIONS FOR THE MEASUREMENT OF RADIATION FROM SHOCK HEATED AIR

Deborah A. Levin
Richard T. Loda

February 1991

IDA

INSTITUTE FOR DEFENSE ANALYSES

PREFACE

The work discussed in this paper was performed for the Innovative Science and Technology Office of the Strategic Defense Initiative Organization for Dr. Leonard Caveny and monitored, in part, by Dr. David Mann of the Army Research Office. The span of the work covers a time period of about one year at a level of effort of approximately one and a half person years. This work, performed at the Institute for Defense Analyses (IDA), is part of the ongoing Boost Phase Signatures program and represents a continuation of an earlier IDA paper entitled "Prediction of Radiation from ICBMs."

The computational fluid dynamics (CFD) techniques used for this work were developed by C. Park and G. Candler at NASA/Ames Research Center. All flowfield solutions and radiations calculations presented here were made on the CRAY XMP located at NASA/Ames and accessed remotely at IDA. Additional analyses and calculations were also run on local computers at IDA.

Since the original preparation of this document, the Bow Shock Ultraviolet (BSUV) experiment referred to here was successfully launched from Wallops Island, VA. However, in this paper, the BSUV experiment will be referenced in the future tense.

Accesion For

NTIS CRA&I	☑
DTIC TAB	☐
Unannounced	☐
Justification	

By ....
Distribution /

Availability Codes

| Dist | Avail and/or Special |
| A-1 | |

iii

ACKNOWLEDGMENTS

ABSTRACT

Application of hypersonic computational fluid dynamics models for the character-
izations and prediction of shock heated air-induced UV radiation from boost phase vehicles
is examined. Specifically, velocities of 3-4 km/sec and altitudes of 40-80 km have been
considered. Important modeling aspects, such as chemical kinetics, electronic excitation/
de-excitation mechanisms, and the existence of equilibrium versus nonequilibrium
conditions in the flow are examined. Comparison of theoretical flowfield predictions with
recent shock tube data, for the purposes of flowfield code validation, is also shown.
Flowfield properties, and in-band radiance values in the 2500Å wavelength region, in the
vicinity of the stagnation stream line, are presented for a three inch hemisphere. These
results were generated to provide input for instrument designers involved in an upcoming
rocket experiment to measure UV radiation produced in the bowshock.

CONTENTS

ABBREVIATIONS

ASAT	Anti-satellite
BSUV	Bow Shock Ultraviolet
CFD	Computational Fluid Dynamics
FOV	Field of view
ICBM	Intercontinental Ballistic Missile
IDA	Institute for Defense Analyses
IR	Infrared
NASA	National Aeronautics and Space Administration
PAET	Planetary Atmospheres Experiments Test
QSS	Quasi-steady-state
SDI	Strategic Defense Initiative
SDIO	Strategic Defense Initiative Organization
SPRAP	Stagnation Point Radiation Program
STRAP	Shock Tube Radiation Program
UV	Ultraviolet
VUV	Vacuum Ultraviolet

EXECUTIVE SUMMARY

A basic technological problem that is of importance to SDI is the characterization and prediction of signatures of low-to-mid-altitude boost phase related threats. Specifically, we are considering velocities of 3-4 km/sec over altitudes from 40-80 km, which might be parameters characteristic of fast burn boosters, or rapidly accelerating direct-ascent anti-satellite (ASAT) interceptors. Much of the related research has concentrated, to date, on the signature that would be caused by plume emissions. However, for either of the above applications, the rocket would be expected to burn out at a low altitude to avoid detection. An alternative signature source that is worthy of examination is the radiation emitted from the shock heated air in front of the missile nose (bow shock). In an earlier paper, we postulated a space-based sensor potentially capable of detecting this emission. The sensor detection advantage of operating in the ultraviolet spectral region was quantified and minimum required signal radiance values were determined. Also, as part of this earlier work, a review of existing experimental results was undertaken. It was found that most of the existing research on radiation emitted from hypersonic vehicles has focused on reentry conditions with velocities on the order of 7 km/sec. Figure S-1 shows our comparison of the calculated spectra of shock heated air for velocity and altitude conditions relevant to boost phase and reentry, respectively. The spectra are integrated over temperature and species concentrations from the shock to the body along the stagnation streamline using the NEQAIR (non-equilibrium air radiation) model written by Park. Examination of Fig. S-1 shows that the lack of N_2^+ radiation at the slower speed is readily apparent, and NO is seen to be the dominant radiator for shock heated air. Hence, the chemical production and destruction mechanisms of NO are key to the correct modeling of radiation for boost phase conditions.

The IDA review also pointed to a lack of data in the boost phase flight regime specified above. This lack of experimental data has made it difficult to verify the predictive capabilities of existing theoretical models in this 3-4 km/sec, 40-80 km altitude flight regime.
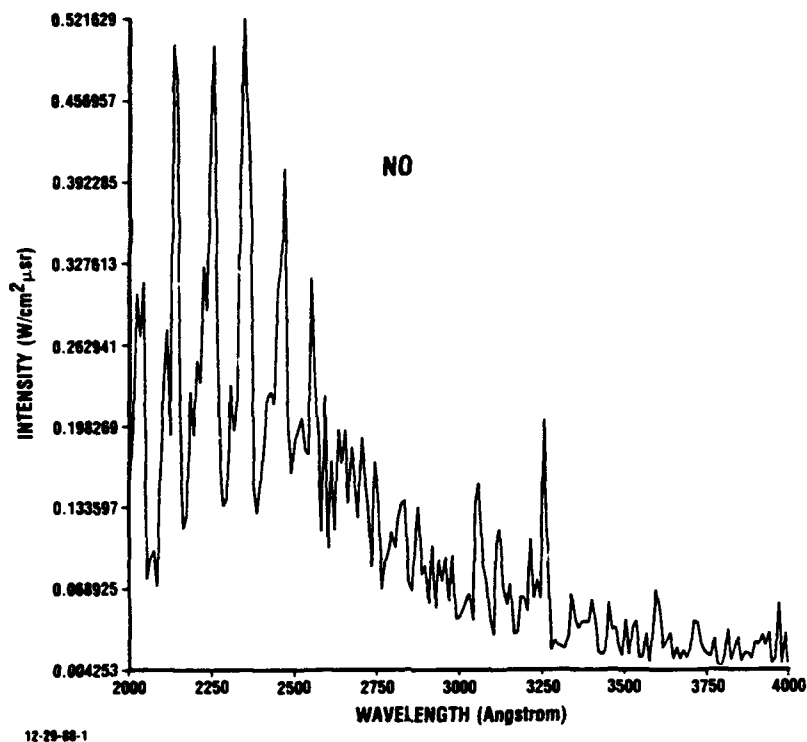
(a) v = 3.9 km/sec, 40 km altitude, 4 in. nose radius and averaged over a spectral width of 10Å.
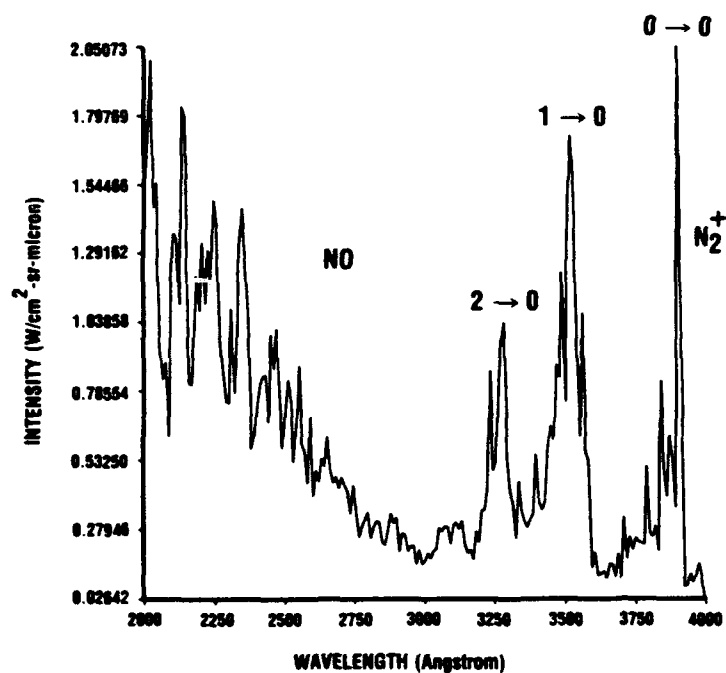
(b) v = 7.3 km/sec, h = 51.7 km, 3 in. nose radius, and averaged over a spectral width of 10Å. Peak height ratio of 1 → 0 and 0 → 0 is an artifact of the spectral range cutoff at 4000Å.

Figure S-1. Comparison of Emission Spectra, Calculated Under Different Shock Conditions.

To correct this deficiency, the Innovative Science and Technology Office of the Strategic Defense Initiative Organization (SDIO) has decided to sponsor a rocket-borne experiment [Bow Shock UV Experiment (BSUV)] that will measure in situ bow shock radiation within the velocity-altitude profile given above. They have also sponsored new shock tube measurements performed by CALSPAN. As will be shown here, this provides a unique opportunity to collect simultaneously data that is both operationally and scientifically relevant. In preparation for the rocket-borne BSUV experiment, IDA has applied computer codes, developed at NASA/Ames Research Center, to predict the signal levels to be expected. The results of these calculations are presented here, and will be used to provide guidelines to the instrument designers in order to make the appropriate choices for instrumental parameters such as wavelength and temporal response, sensitivity, dynamic range, etc.

The NASA/Ames computational fluid dynamics (CFD) and radiation codes were originally written for, and verified at, reentry velocities ($\geq$ 6 km/sec). Results from blunt body experiments such as the Planetary Atmospheres Experiments Test (PAET) have been used for code validation, but this probe has a nose radius approximately five times the value for a boost phase vehicle, and its velocity was also much greater. With the cooperation of the NASA/Ames code authors, we (IDA) applied their codes to the above boost phase flight regime for the first time. To that end, we found it necessary to examine, in detail, important modeling aspects such as chemical kinetics, electronic excitation/ de-excitation mechanisms, and the existence of equilibrium versus non-equilibrium conditions in the flowfield. Chapter II, Sections B, C, and E, provide a detailed discussion of that work. There, results of temperatures, species concentrations, and the spatial distribution of radiation are presented. Code validation, through comparison with new shock tube data taken under conditions representative of the boost phase, is described in Section II.D. Scaling with altitude was experimentally observed and also obtained in the theoretical results. Figure S-2 illustrates that the agreement between experiment and theory was a factor of 2-3, for a range of velocities and simulated altitudes.

These results, and the sensitivity analyses performed with respect to chemical kinetics and excitation/de-excitation mechanisms, lead to confidence in the modeling for 40 km altitude, 3.5 km/sec shock conditions. For lower velocities and/or higher altitudes than the above conditions, one of the NASA/Ames codes (SPRAP) began to produce unphysical results, primarily caused by improper modeling of the cool wall boundary layer
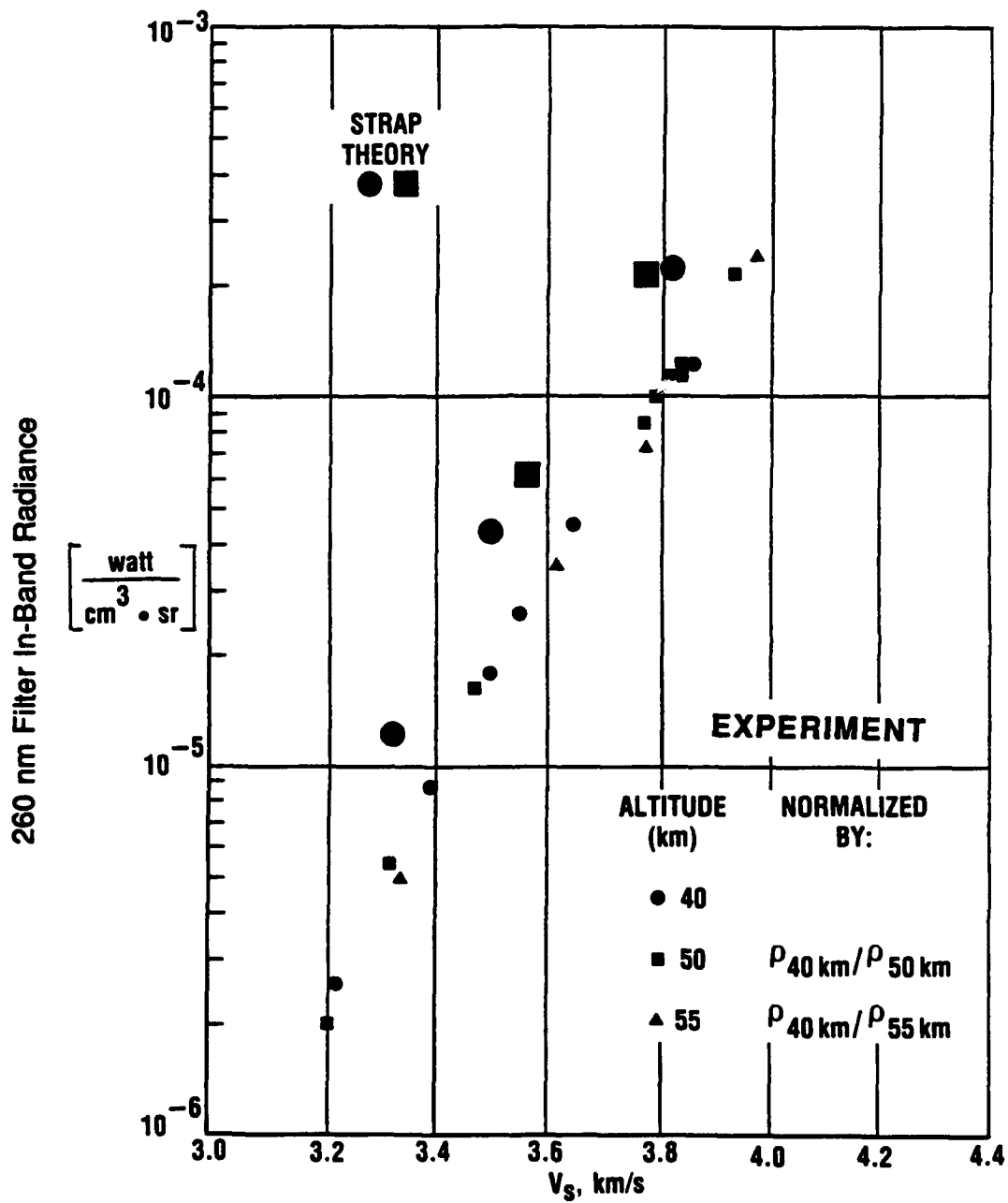
Figure S-2. Comparison of Shock Tube Experimental (CALSPAN) and Model (IDA/Ames) Results. V_s is the shock velocity, and ρ is the density.

in the bow shock-producing nose region. This led us into using an alternate NASA/Ames CFD code, which had improved modeling over both the shock thickness, and cool wall boundary layer, regions. As an added benefit, use of this alternate code also enabled the computation of a two-dimensional radiation map with which to deduce the radiating area of the bow shock region (referred to in this paper as the 2-D code).

A chemical kinetics model that incorporated the same chemical reactions as are in the 2-dimensional flow field model was developed by us, separately, to permit easier testing of the importance of trace atmospheric species concentrations and the variation of kinetic rate data found in the literature. Except for initial conditions that would correspond to very weak shock conditions, no significant differences in the concentrations of NO, O, or electrons were computed for a time scale corresponding to flow transit times. A similar result was also found when different rate constants were used, although some sensitivity to choice of equilibria constants was observed at temperatures below about 3000°K. We concluded from these results, and a smaller set of sensitivity runs computed with the entire flow field modeling, that the present chemical kinetics modeling is adequate in terms of the prediction of UV radiation. Modification of free stream boundary conditions to incorporate trace atmospheric species or use of other rate constant data does not produce significantly different results in terms of species concentrations or radiation for our flight conditions. Finally, with the simpler kinetic model, we examined the time rate of change of species concentrations to deduce the time necessary to equilibrate. We found that for the densities and temperature conditions that exist in boost phase trajectories the solution of the finite rate equations was far from equilibrium. Therefore, chemical non-equilibrium must be modeled in any flow field code used in this flight regime to predict bow shock observables. This is done in the flowfield and radiation codes used here.

In terms of electronic excitation/de-excitation mechanisms of species in the flow, we investigated the adequacy of the present radiation model used. The model, NEQAIR, is a non-equilibrium air species model, with the capability to calculate radiation from the VUV to the short wave IR. The model incorporates both electron and neutral collisional mechanisms; but, to date, has emphasized the former. In the boost phase flight regime, we found that there were typically about two orders of magnitude fewer electrons produced than under usual reentry conditions, with a lower electron temperature of about 0.5 eV. The model invokes the quasi steady state approximation, and microscopic reversibility. To shorten computational time, and due to the paucity of experimental state specific measurements at higher temperatures, the model does not directly permit inter-molecular

exchange processes. Our investigations focused on neutral impact mechanisms related to NO excitation. Modifying NEQAIR to use available experimental data, which is in itself not sufficiently adequate, we concluded that the baseline modeling is probably adequate at speeds of 3.5 km/sec and altitudes up to 50 km. At higher altitudes, the number of collisions decreases sufficiently so that the use of microscopic reversibility becomes questionable. We also found ourselves in a complicated flow regime where neither electronic or neutral collisional mechanisms dominate and both must be modeled accurately. In the 2500Å spectral region, we found the gas to be optically thin for the speed and altitude conditions used in this paper.

From the models discussed above, we computed the amount of radiation obtained in the NO gamma bands, centered at approximately 2500Å, as a function of altitude and speed, for a three-inch nose radius vehicle. The nose radius and trajectory conditions were chosen to match postulated fast burn threats. Figure S-3 shows a summary of these results. These data represent the primary results of this paper, and were used by the instrument designers for the BSUV rocket-borne experiment discussed earlier. As mentioned above, this flight regime requires both thermal, as well as chemical non-equilibrium modeling. There are many additional questions, discussed in detail in Chapter II, regarding the fidelity and necessity of the former. To demonstrate the degree to which the flowfield solutions are in thermal non-equilibrium, as well as calculate a theoretical lower bound to the amount of radiation obtainable, a special version of the 2-D code was developed and made available to us by Dr. G. Candler (the author of the code). Figure S-3 shows results of the multi-temperature and single temperature (i.e., thermal equilibrium) models. The figure shows that at faster speeds, and lower altitudes, the solutions approach thermal equilibrium, as expected. However, for much of the boost phase trajectory parameter space, orders of magnitude over prediction in the amount of radiation obtainable would be made by incorrectly assuming equilibrium conditions.

Finally, since this work is developmental, it is by its very nature incomplete. The models have been shown to be useful in generating preliminary estimates for BSUV optical instrument sensitivities. Additional work is ongoing to extend these tools to model the response of planned optical instruments in the BSUV experiment, both on and off axis, and as a function of instrument field of view. Chapter III provides a summary of these issues and topics.
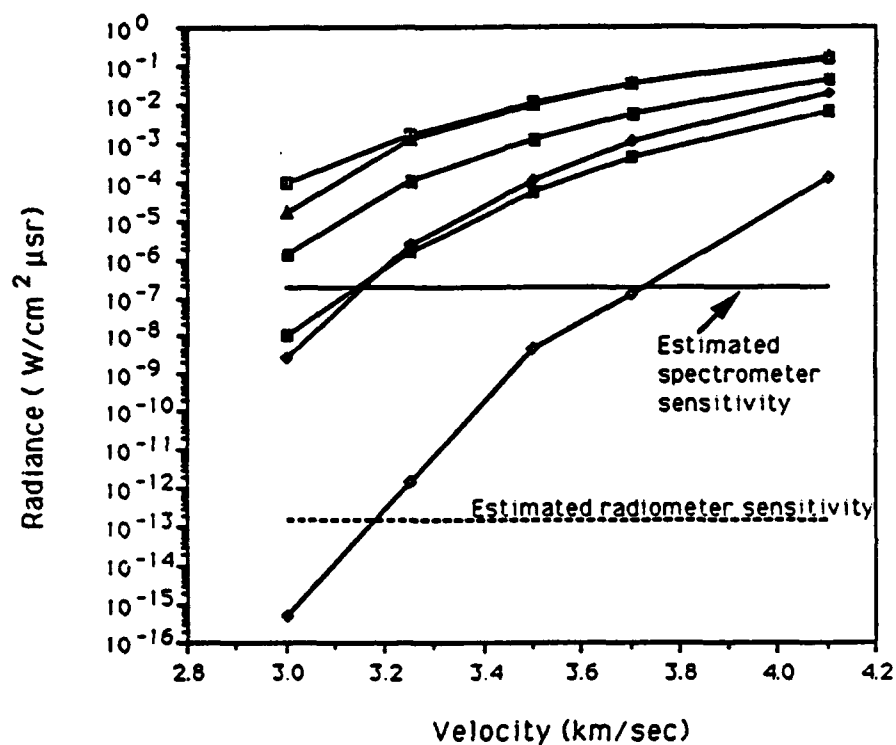
Figure S-3. Summary of three-inch nose radius calculations. Comparison between thermal equilibrium and non-equilibrium modeling is shown as a function of speed and altitude. Radiances shown are at the stagnation point on the vehicle nose.

40km, Multi-T	40km,Single-T	50km,Multi-T
50km,Single-T	60km,Multi-T	60km,Single-T

Thermal equilibrium is Single-T, and Non-equilibrium is Multi-T. Radiances are calculated from 2250 to 2750Å assuming a rectangular filter with 100% transmittance.

A separate memorandum will be issued regarding the operational utility of the bow shock signatures, based on the information to date. Again, the purpose of this paper is to summarize our research to date. Per sponsor request, we have been asked to communicate the results in this paper in an unclassified format to the university and applied laboratory community.

I. INTRODUCTION

A. OVERVIEW

A basic technological problem that is of importance to SDI is the characterization and prediction of signatures of low-to-mid-altitude boost-phase-related threats. Specifically, we are considering velocities of 3-4 km/sec over altitudes from 40-80 km, which might be parameters characteristic of fast burn boosters, or rapidly accelerating direct-ascent anti-satellite (ASAT) interceptors. Much of the related research has concentrated to date on the signature that would be caused by plume emissions. However, for either of the above applications, the rocket would be expected to burn out at a low altitude to avoid detection. An alternative signature source that is worthy of examination is the radiation emitted from the shock heated air in front of the missile nose (bow shock). In an earlier paper (Ref. I-1) we postulated a space-based sensor potentially capable of detecting this emission. The sensor detection advantage of operating in the ultraviolet spectral region was quantified and minimum required signal irradiance values were determined. Also, as part of this earlier work, a review of existing experimental results was undertaken. This review pointed to a lack of data in the flight regime specified above. This lack of experimental data has made it difficult to verify the predictive capabilities of existing theoretical models in this 3-4 km/sec, 40-80 km altitude flight regime.

To correct this deficiency, the Innovative Science and Technology Office has decided to sponsor a rocket-borne experiment that will measure in situ bow shock radiation within the velocity-altitude profile given above. They have also sponsored new shock tube measurements performed by CALSPAN. As will be shown here, this provides a unique opportunity to collect simultaneously data that is both operationally and scientifically relevant. In preparation for the rocket-borne experiment, IDA has applied computer codes, developed at NASA/Ames Research Center, to predict the signal levels to be expected. The results of these calculations are presented here, and will be used to provide guidelines to the instrument designers in order to make the appropriate choices for instrumental parameters such as wavelength and temporal response, sensitivity, dynamic range, etc. Comparison of our shock tube calculations (using NASA codes) to the CALSPAN shock tube measurements will be presented here as well.

The NASA/Ames computational fluid dynamics (CFD) codes were originally written for, and verified at, reentry velocities ($\gtrsim$ 6 km/sec). Results from blunt body experiments such as the Planetary Atmospherics Experiments Test (PAET) (Ref. I-2) have been used for code validation, but this probe has a nose radius approximately five times the value for a boost phase vehicles. The fast-burn, boost-phase condition CFD results given here have allowed us to identify altitude-velocity regions where the present modeling may be questionable, and have enabled us to suggest fruitful areas of high temperature flow research, such as collisional excitation and de-excitation and relaxation mechanisms of atomic and molecular species. As will be shown in this paper, the accuracy of the boundary layer modeling becomes very significant in the fast-burn, boost-phase flight regime. Also, due to the smaller shock stand-off distance and non-equilibrium conditions, accurate modeling of relaxation mechanisms among the translational, vibrational, and electronic energy modes in the flow is crucial to reliable radiative signature prediction.

In addition to decreasing the magnitude of radiation expected at fast-burn, boost-phase speeds, new mechanistic questions are raised. For example, Fig. S-1 shows a comparison of calculated spectra of shock heated air under different speed and altitude conditions. Although the velocity, altitude, and nose radius changes from Fig. S-1(a) to (b), the dominant factor in producing the spectral differences in the figures is caused by the velocity change. The spectra are integrated over temperature and species concentrations from the shock back to the body along the stagnation stream line. The specific computer codes are discussed in Chapter II; however, the lack of N_2^+ radiation at the slower speed is readily apparent. NO is the dominant radiator at slower speeds; hence, the chemical destruction and production reactions of NO from air are the key ones at slower speed. This point is discussed further in Chapter II.B and C. As will become evident from the results of flowfield calculations shown in Chapter II, fewer, and less energetic, are electrons produced under slower speed conditions. This in turn increases the importance of neutral collisional excitation mechanisms. As analysis of the modeling adequacy of neutral collisional processes is given in Chapter II.C.

The importance of a multi-temperature model versus a single temperature (equilibrium) model prediction, and the validity of a combined vibrational-electronic temperature at shock conditions even weaker than those that correspond to Fig. S-1(a) is also of concern. The latter question is only partially resolved in this paper.

B. ORGANIZATION

The paper is organized to present as much technical detail as possible, with parenthetical and supporting analyses and results put into appendixes. Chapter II gives detailed results regarding the subject areas mentioned above.

The principal theoretical aspects of the modeling and key physical approximations made are discussed in Chapter II.A. Our own validation of code output, as well as comparison between the one-dimensional Stagnation Point Radiation Program (SPRAP) and 2-D codes is detailed in Appendix A. In Section II.B, we discuss the sensitivity of the results to trace atmospheric spaces such as O and NO, that exist between 40 to 80 km altitude. Also, the variability in model predictions to differences in chemical kinetic rates is assessed. To test these hypotheses a kinetic model separate from the entire flowfield model was developed. The model, as well as results obtained regarding the degree to which the present flowfield solutions differ from chemical equilibrium conditions, is discussed. In Section II.C the factors that define and control the amount of radiation obtained in the UV are investigated. Alternative excitation/de-excitation rates to those programmed in NEQAIR, the non-equilibrium air radiation model used here, are explored. In Section II.D we present comparison of shock tube flowfield predictions with recent CUBRIC/ CALSPAN experimental results. In Appendix B, the present ambiguity in quantitatively assigning individual species' radiative contributions is discussed. Finally, Section II.E presents our key results generated in support of the IS&T bow shock experiment (BSUV).

In Chapter III, a summary of our conclusions regarding our work to date is given. Since this work represents a portion of an ongoing research effort, it is necessarily incomplete. Future work and calculations are identified. A separate memorandum will address operational considerations and implications for the future.

REFERENCES, CHAPTER I

A-1.   R. Collins, A. Kim, R. Loda, and D. Levin, *An Examination of Hardbody Radiation from ICBMs*, Institute for Defense Analyses, IDA Paper P-2092, September 1988.

A-2.   E.E. Whiting, J.O. Arnold, and R.M. Reynolds, *Quant. Spectros., Radiat.. Transfer*, 13, 837 (1973)

II. DESCRIPTION OF CALCULATIONS AND RESULTS

A. DESCRIPTION OF THEORY AND COMPUTATIONAL PROCEDURE

In this section we discuss the computational procedures used to derive flowfield properties such as temperatures, species concentrations, and radiances. Since we have primarily been users, not developers, of the NASA/Ames CFD and radiation codes, and since these codes have been described in great detail elsewhere (Refs. II.A-1 to -6), we present here only an overview of the basic equations solved, with the key physical approximations assumed for our problem of interest. For greater detail, the interested reader is encouraged to examine the works referenced above. In this section, we also relate our flowfield shock structure terminology to that used earlier by the reentry community (Ref. II.A-7).

The fundamental equations are solved in the Navier-Stokes approximation for mass conservation of species (i.e., N_2, O_2, NO, NO^+, N, O, e^-, and N_2^+), mass averaged momentum conservation, and total energy conservation. The requirement for total energy conservation is also coupled with the possible transfer of energy between translational, vibrational, and electron degrees of freedom for each of the species in the flow. The translational and rotational modes are assumed to be equilibrated in the flow. This assumption is based on the knowledge that the energy exchange between translational and the rotational modes is very fast under conditions of interest here.

The NASA/Ames codes used in this work basically employ a two-temperature, nonequilibrium kinetic model as a compromise between two previously studied alternatives. The first of these alternatives is a one-temperature description of the problem, which is known to be incorrect because it leads to a substantial overestimation of the rate of equilibration because of the elevated vibrational temperature (Ref. II.A-8). The second alternative is a three-temperature chemical-kinetic model (Ref. II.A-1); however, this model is quite complex and requires many chemical rate parameters that are not yet known. Thus, the two-temperature chemical-kinetic model was developed as a compromise. In this latter model, one temperature, T, is used to characterize both the translational energy of the atoms and molecules and the rotational energy of the molecules. The second temperature, T_v, is

used to characterize the vibrational energy of the molecules and translational energy of the electrons. Theoretically there should be a distinct vibrational temperature for each molecular species in the flow. For the cases considered in this work, the flow is composed of about 78 percent N_2. Hence a single T_v model was found to be adequate. A mechanism for the equilibration of the electron translational temperature (which is in the order of 0.5V or less) with the molecular vibrational temperature exists through an electron-collisional resonance.[1] The translational-vibrational relaxation rate is calculated using a modified form of the correlation formula of Millikan and White (Ref. II.A-9). The modifications (Ref. II.A-5) take into account a high temperature cross section limit and the diffusive nature of vibrational relaxation.

Figure II-1, taken from Ref. II.A-7, shows the three characteristic regions of the bow shock stand-off distance (designated shock wave, shock layer and boundary layer in the figure). Also the temperature, pressure, density, and velocity profiles, while obtained from less rigorous calculations than will be shown here, qualitatively show the correct behavior. The shock stand-off distance is on the order of a tenth of the vehicle nose radius. The thickness of the shock wave is determined by the time required for a sufficient number of collisions to occur so that species can equilibrate, in the translational-rotational excitation modes, to the conditions behind the shock.

The shock layer is qualitatively described as an inviscid flow that is unaffected by the shock wave and boundary layer, and the boundary layer must be described as viscous flow over the body. The influence of the cooler boundary layer on radiation strength will be seen in the results shown in this report, particularly in the case where it subsumes a larger portion of the shock stand-off layer (i.e., for weaker shock conditions).

Three NASA/Ames CFD codes have been used in the work reported here. Two of these are the Shock Tube Radiation Program (STRAP), and the Stagnation Point Radiation Program (SPRAP), both written by C. Park at NASA/Ames Research Center (Refs. II.A-2, -5). The STRAP program computes theoretical results for nonequilibrium flow behind a normal shock wave in a constant area duct, and SPRAP computes the flow properties along the stagnation streamline[2] in the shock stand-off layer for spherical bodies

---

[1] Such a resonance exists for the $N_2 - e^-$ system (labeled as the $^2\Pi_g$ shape resonance) with a cross-section enhancement of almost two orders of magnitude.

[2] Streamline at $\theta = 0$ deg in Fig. II-1.
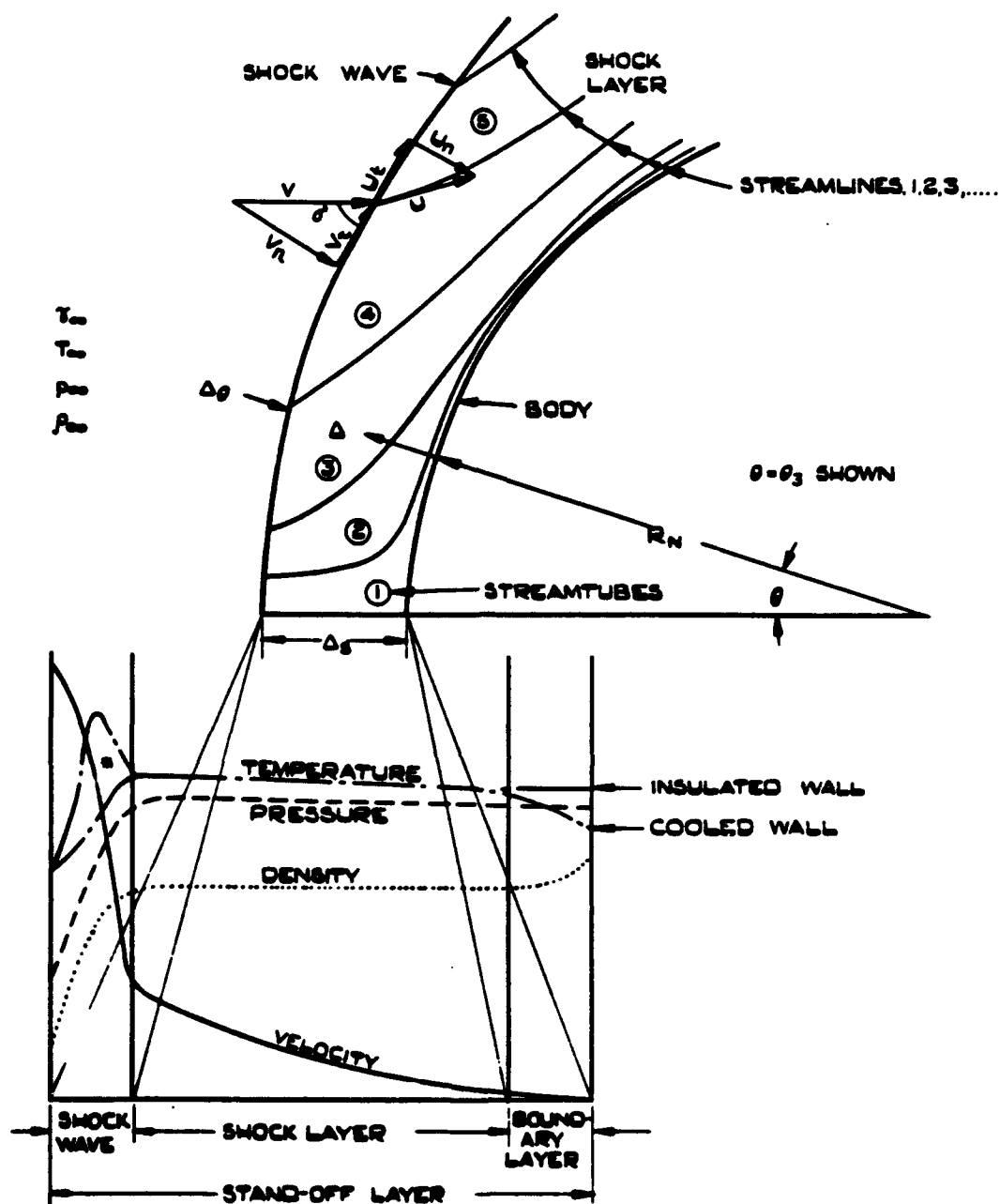
* Contains discrete temperature distributions for translational (upper limit), rotational, vibrational, electronic, chemical, and ionization excitation as appropriate to v.

Figure II-1. Summary of Bow Shock Structure (Ref. II.A-7)

moving at hypersonic speeds. They are both one-dimensional (1-D) programs in that they calculate the flow properties only along the axis of shock propagation (STRAP), or the stagnation stream line (SPRAP). The third CFD code used in this work was developed by G. Candler (Refs. II.A-3, -4). This code contains a number of improvements over the STRAP and SPRAP codes and may be applied to an arbitrary two-dimensional (2-D), or axisymmetric body with a shock stand-off layer that is in thermochemical nonequilibrium and weakly ionized. Using this program, one can predict how the flowfield properties will vary over the nose cone area of a rocket. The Candler code was ultimately determined to be the most appropriate for use in the velocity-altitude profile in the work given here (see discussion below). It will hereafter be referred to in this paper as the "2-D code."

Once the flowfield solutions have been obtained from either of the three CFD codes discussed above, the flowfield radiation is calculated using the norequilibrium air radiation (NEQAIR) module (Ref. II.A-6), which is common to all three CFD codes.

Figure II-2 provides a schematic of the interrelationship of the different computational tools used in our calculations. Initial conditions include those corresponding to the body's speed (v_∞), nose radius (r_n), and ambient altitude conditions such as free stream density (ρ_∞) and temperature (T_∞), as well as ambient conditions of major and minor species concentrations such as atomic oxygen and free electrons. Figure II-2 shows that one can obtain from the flowfield codes state variables of the gas such as species concentrations and temperatures as a function of spatial location behind the shock. In Section E, examples are shown to illustrate the change of these parameters as a function of shock conditions. In total, Fig. II-2 demonstrates the procedure for calculating bow shock UV passive signatures from first principles.

The flow calculations are initially done assuming that there is no energy loss by radiation. In the 1-D code, radiation loss can be accounted for in an iterative procedure. We have depicted this possibility with the dotted line shown interconnecting the two main program modules in Fig. II-2. This option was not exercized with the 2-D code. For the weak shocks produced under the velocity-altitude profile considered here, accounting for radiation losses in the flow has a negligible effect on the predicted radiation levels that might be observed by optical sensors in the UV spectral region.

The STRAP program calculates the properties of a viscous flow in a constant area duct behind a normal shock wave. The calculation uses a time-marching technique: an initial starting solution is first assumed, and its relaxation with time is computed. The time

Input

v_∞
r_n
ρ_∞
T_∞
$[N_2]_\infty$
$[O_2]_\infty$
$[e]_\infty$
$[O]_\infty$
$[O_3]_\infty$

Flow field Solver

Models:

STRAP (1-D)
SPRAP (1-D)   C. Park
2-D   G. Candler

Significant Features:
- Multiple temperatures
- Finite rate chemistry coupled to the flow

Species concentrations Temperatures as a function of location in the shock

Calculation of Radiation
Model: NEQAIR
Significant Features:
- QSS approximation used
- Neutrals as well as electronic excitation mechanisms
- Line by line spectral computational capabilities from .15 to 2. μ
- Line broadening effects included

Bow shock irradiance Detectivity

DAL.:dlg:#1
Fig 1 2/6/89

Figure II-2. Schematic Bow Shock Calculations

dependent solution eventually reaches a steady state, which is the required solution (Ref. II.A-2). Thirty-one reactions of air and its related decomposition products are modeled in the chemically reacting flow. In the kinetics modeling, it is assumed that all species are in their electronic ground states, i.e., no excited state chemistry is included. Since the kinetic parameters used in the code come from a best fit to high temperature shock tube data, this assumption should not produce large errors.

The nonequilibrium thermodynamic properties obtained from the above steady-state solution are next passed to the NEQAIR module, where the number densities of the various electronic states for the species in the flow are calculated. To do this, the quasi-steady-state (QSS) condition is invoked. This condition is based on the assumption that the electronic state population and depopulation rates are much faster than the difference between them, and is believed to be valid up to altitudes of 60 km. A separate effective electronic excitation temperature for each atomic and molecular species is obtained by a Boltzmann fit to the QSS-derived populations.

For our flow conditions, neutral as well as electron-collisional-induced excitation mechanisms are important. The former is not treated with the full state specificity as might be desirable; however, as is discussed in Section C, it is probably adequate for our conditions of interest.

II-5

The SPRAP code is actually an extension of the STRAP program in that the thermodynamic properties at each node point along the stagnation streamline in SPRAP are assumed to be the same as the flow properties of STRAP, taken at the same residence time. This concept is illustrated in Fig. II-3, taken from Ref. II.A-5. To obtain a transformation of the velocity/enthalpy profiles of the gas from the shock tube solution to the bow shock stand-off region, the following assumptions are made. The modeling in the shock layer of the shock stand-off region assumes a perfect gas. For the first iteration, the density in the shock layer is assumed to be constant and a factor of ten higher than that of the free stream, with a Prandtl number of 0.7 used. The second iteration uses the density profile obtained in Step 1 to match and solve for the solution in the inviscid portion of the shock layer. This procedure makes a correction for the presence of viscous terms in the mostly inviscid shock layer. As some of the results will show, there is sometimes a small numerical discontinuity visible in the plots of species concentrations versus location in the shock stand-off region at the location of the viscid-inviscid boundary. The density profile in the boundary layer is obtained by assuming that chemical reactions are frozen, i.e., the species concentrations are constant in the boundary layer. A wall temperature is specified as input to the code. From these series of calculations, made in the perfect gas approximation, the flow resident times in the gas are stored. They are then used to map the thermodynamic properties calculated in the nonequilibrium constant-area duct flow into the bow shock region (Fig. II-3). After this transformation is performed, the radiation heat flux is obtained by integrating the emission power along the stagnation stream line.

The techniques used in the 2-D code developed by Candler (Ref. II.A-3, -4) borrow from much of the work initiated by Park (Ref. II.A-5). In spite of longer computational times, it was decided to utilize this code because fewer assumptions are made in the derivation of the governing flowfield equations. Under our flight conditions, inclusion of viscous terms in the boundary layer is important. A viscosity model for reacting air is utilized in the 2-D code and is valid up to temperatures of 10,000°K, and for weak ionization. This modeling is lacking in the one dimensional model of Park. The fully coupled set of equations are integrated in a time marching fashion to solve for a steady-state solution. The 2-D model also assumes (as does that of Park) that the continuum formulation is valid. The continuum formulation begins to break down at (high) altitudes where the true thickness of the shock wave becomes comparable to the thickness of the shock layer. The continuum formulation being valid, in turn, requires that the Knudsen number (i.e., the ratio of the mean-free-path in the flow to the characteristic length scale of
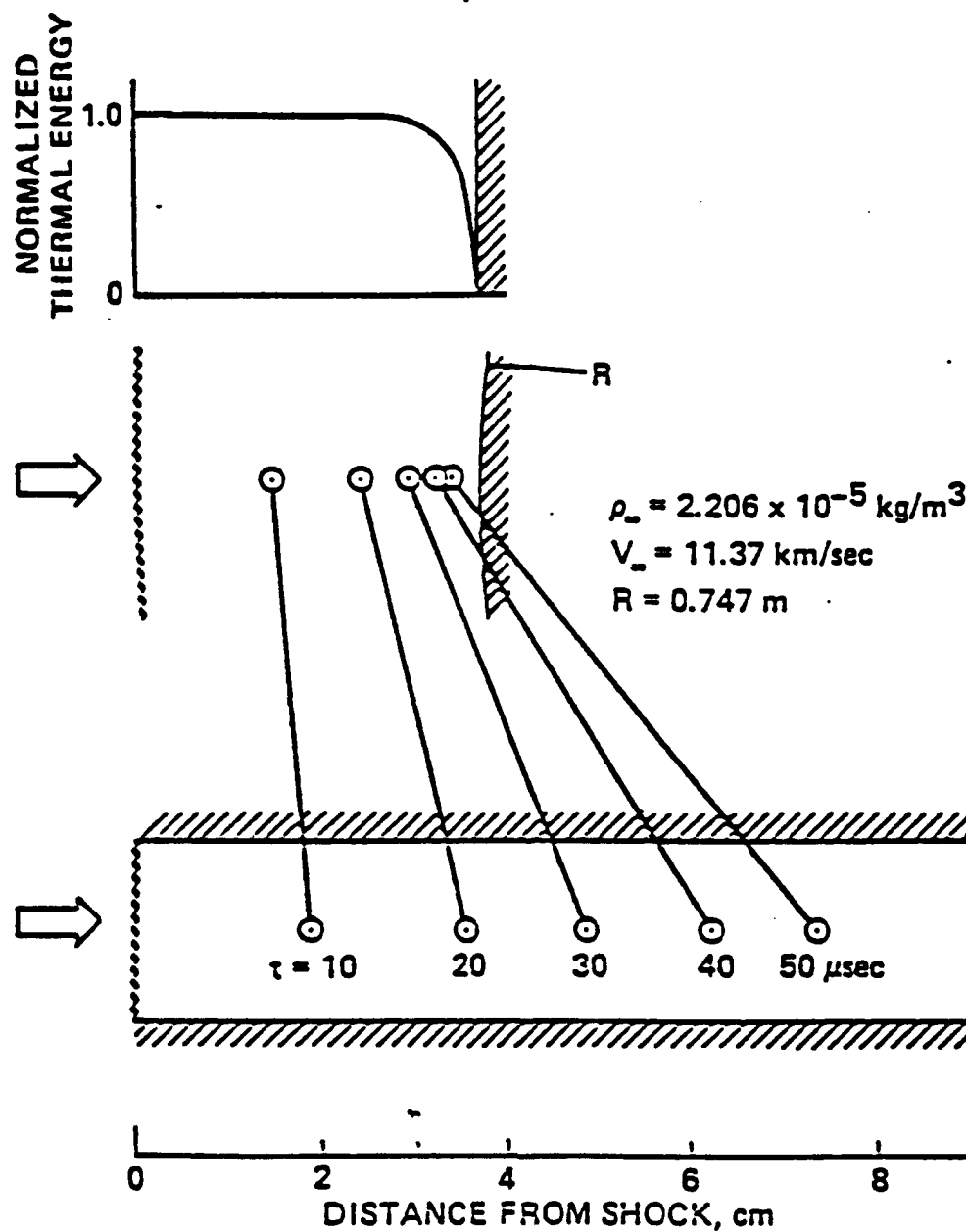
Figure II-3. Schematic showing the correspondence between the flow along the stagnation streamline and the flow through a constant-area tube. The case chosen is for Fire 2 vehicle at 79.1 km altitude. (Taken from Ref. II.A-5.) ρ_∞, V_∞, R are the free-stream density, velocity, and nose radius of the vehicle.

the body or flow) be much less than one. For nose radii such as we used, this criteria was found to hold for all the altitude and velocity conditions examined here.[3]

Table II-1 provides a comparison between the 1-D and 2-D codes.

Table II-1.   Comparison of Computational Fluid Dynamics Codes

1-D (C. Park, Refs. II.A-2, -5, -6. -8)	Versus	2-D (G. Candler, Refs. II.A-3, -4)
Rankine-Hugoniot Conditions: Infinitely thin, no reacting chemistry in the shock	Versus	Finite thickness shock with reacting chemistry
Chemical Reactions: 31	Versus	7
Flow field coupling to reacting chemistry: Loosely coupled	Versus	Fully coupled
Wall Region Boundary Conditions: No Boundary Layer Chemistry	Versus	Reacting chemistry
Radiation losses: Coupled to flow field solution	Versus	Uncoupled
2-Temperature Model: T, T_v [a]	Versus	3-Temperatures: T, T_v, T_e [b]

[a] T and T_v are the gas heavy particle translational and vibrational electron temperatures, respectively.

[b] T, T_v, T_e are the gas heavy particle translational, vibrational, and electron translational temperatures, respectively. Note that although three distinct temperatures are possible in this model, results presented here were obtained with $T_v = T_e$. This is based on arguments given in Appendix A.

Spectral as well as radiometric calculations have been made using the NEQAIR model. To save computational time an optically thin gas was assumed. The validity of this assumption is examined in Section C of this Chapter.

The output of NEQAIR obtained from the 2-D flowfield provides a two-dimensional radiation profile for an axi-symmetric geometry. From this, bow shock radiance and ultimately, off board detectivity can be determined. Radiance predictions for various wavelength bands will be discussed in the upcoming sections with various results presented as a function of trajectory input.

---

[3] Based on the experience of the 2-D code author, converged solutions can be obtained conditions such as that the mean free path divided by the nose radius is less than 0.1. For a 3-inch nose radius this will hold up to 80 km altitude.

The above computational tools are sufficiently complex[4] and new that, despite efforts to document the codes for outside users, the process is still incomplete. Also, as mentioned earlier, these codes have not been exercised extensively before under the Knudsen conditions of interest here. As such, we proceeded in a manner to use the SPRAP code to reproduce selected portions of the optical data obtained from the PAET probe as a check against the work of Park. When it was recommended that we proceed to using the 2-D code for our problem, we obtained a solution of that code to compare directly with SPRAP. The salient results of that process, as well as some new aspects of the codes that we (as well as the original authors) discovered in this process, are reported in Appendix A.

The key result demonstrated in Appendix A is that the present electron temperature model in the 2-D code is not correct at 4.1 km/sec, 40 km altitude or weaker shock conditions. Hence, the 2-D model was used in a manner analogous to the 1-D model in terms of assuming a single combined vibrational and electron temperature for the results shown in this paper. This latter assumption enabled us to obtain 2-D code radiation prediction results that agreed with the 1-D code values, which had been favorably compared to the PAET experimental probe data.

---

[4] It requires approximately 0.5-2 hours of Cray X-MP CPU time to do a single converged flowfield and radiation calculation at a given velocity and altitude for the codes discussed here.

REFERENCES, CHAPTER II.A

II.A-1. J.H. Lee, AIAA-96, 3-53 (1985).

II.A-2. C. Park, *User's Manuals for SPRAP and STRAP*.

II.A-3. G. Candler and R. MacCormack, *The Computation of Hypersonic Ionized Flows in Chemical and Thermal Non-equilibrium*, AIAA-88-0511.

II.A-4. G. Candler, dissertation thesis, Dept. of Aeronautics and Astronautics, Stanford University, June 1988, *The Computation of Weakly Ionized Hypersonic Flows in Thermo-Chemical Non-equilibrium*.

II.A-5. C. Park, *Assessment of Two-Temperature Kinetic Model for Ionizing Air*, AIAA-87-1574.

II.A-6. C. Park, "Calculation of Non-equilibrium Radiation in the Flight Regimes of Aero-Assisted Orbital Tansfer Vehicles," *Thermal Design of Aero-Assisted Orbital Transfer Vehicles: Progress of Astronautics and Aeronautics*, by H.F. Nelson, Ed., 96, 1985.

II.A-7. J.J. Martin, *Atmospheric Reentry*, Prentice-Hall Space Technology Series, 1966.

II.A-8. C. Park, "Problem of Rate Chemistry in the Flight Regimes of Aero-Assisted Orbital Transfer Vehicles," *Thermal Design of Aero-Assisted Orbital Transfer Vehicles: Progress in Astronautics and Aeronautics*, Vol. 96, H.F. Nelson, Ed., American Institute of Aeronautics, New York, NY, 1985, pp. 511-537.

II.A-9. R.C. Millikan and D.R. White, "Systematics of Vibrational Relaxation," *J. Chem. Phys.*, 39, 3209 (1963).

B. KINETIC RATE ANALYSIS OF THE FLOWFIELD CHEMICAL EQUATION

The abovementioned CFD codes utilize finite rate chemistry coupled to the flow instead of assuming equilibrium conditions. For the flight regime for which they were originally developed, the chemical reaction time scale is on the order of the convection time scale of the flow. When we began applying these models to boost phase trajectories several questions were raised regarding the adequacy of the chemical kinetics incorporated in the models. We developed a simple kinetics model that allowed us to explore issues, such as (1) the degree to which chemical reactions were unequilibrated, (2) sensitivity to rate and equilibria constants, and (3) sensitivity to free stream boundary conditions due to the presence of trace atmospheric species. The chemical kinetic model that we used incorporated the following six reactions:

$$N_2 + M \rightleftarrows 2N + M \tag{1}$$

$$O_2 + M \rightleftarrows 2O + M \tag{2}$$

$$NO + M \rightleftarrows N + O + M \tag{3}$$

$$N_2 + O \rightleftarrows NO + N \tag{4}$$

$$NO + O \rightleftarrows O_2 + N \tag{5}$$
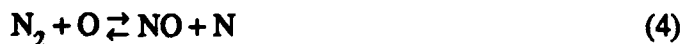
$$N + O \rightleftarrows NO^+ + e^- \ , \tag{6}$$

where M represents a collision partner and includes the seven following species: N_2, O_2, NO, N, O, e^-, and NO^+. A system of first order ordinary differential equations was solved to obtain concentration as a function of reaction time for each of the seven species using standard kinetic rate formalism (Ref. II.B-1). Gear's Method (Ref. II.B-2) was employed since the equations are stiff. To analyze our results we used species concentrations at a representative time of 10 μsec as a significant measure. This time was chosen because it roughly approximates the time required for a gas molecule to move through the shock layer produced at 40 km altitude and a velocity of 4 km/sec. An important caveat about the results to be presented is that, due to the limited number of chemical reactions modeled, the analyses would not be valid for temperatures higher than 8000°K (that are, e.g., produced at orbital velocities).

Figure II-4(a) shows the change in species mole fraction for the N_2, O_2, NO, O and e^- as a function of reaction time. The conditions were chosen to approximate those behind a 40 km altitude, 4 km/sec shock produced by a three-inch radius nose cone. Figures II-4(b)-(g) show the rate of change of the same species concentrations. At a reaction time of 100 μsec, the solutions are still not equilibrated. Basically, the time to reach chemical equilibrium will depend on the pressure (maximum order cubic) and temperature.

Reaction times of 10^3-10^4 μsec were required before species such an [N_2] and [O] were seen to equilibriate. Clearly, Fig. II-4 shows that we are in a non-equilibrium chemistry regime over time periods corresponding to shock layer residence times in the flow. The equilibrium mole fraction values corresponding to conditions specified in Fig. II-4 are 0.617, 7.99×10^{-4}, 1.17×10^{-2}, 4.19×10^{-2}, 0.329, and 4.47×10^{-5} for species N_2, O_2, NO, N, O, and e^-, respectively.

The importance of choosing chemical processes and their respective rate constants consistent with the high temperature flow environment has been examined extensively by Park (Refs. II.B-3, -4, -5). Due to the reinterpretation by Park (Ref. II.B-3) of the high temperature rate data, the STRAP/SPRAP and 2-D flowfield codes do not have the same kinetics data base. The former set of codes uses values given in Ref. II.B-6, whereas the latter code uses values taken from Refs. II.B-4 and -7. Hence, a comparison of species concentrations, obtained at 10 μsec with our kinetic model using the two different sets of rate data and equilibria constants, demonstrates the importance of these differences in our flight regime. The differences in the Park and Candler models are dominated by dissimilar equilibria constants. The largest difference was found with respect to O_2 dissociation at temperatures of 2000 to 3000°K. When the latter set of equilibria constants are used, predictions obtained with either set of rate data agree within factors of two, above 4000°K, for 40 through 60 km altitude free stream conditions.

The results discussed here are specific to this simple kinetics study only. When the chemical kinetics are coupled to the flow properties, the impact of the differences observed could be reduced, since there are other competing effects. For example, in the actual flowfield, the temperature will not be constant over the temporal/spatial profile in the flow (i.e., refer to Fig. A-4 in Appendix A). The amount of radiation emitted also depends on both temperature and species concentrations. Because of these considerations, it was decided to use the original rate data in each of the respective CFD codes.

Finite Rate Chemical Solutions
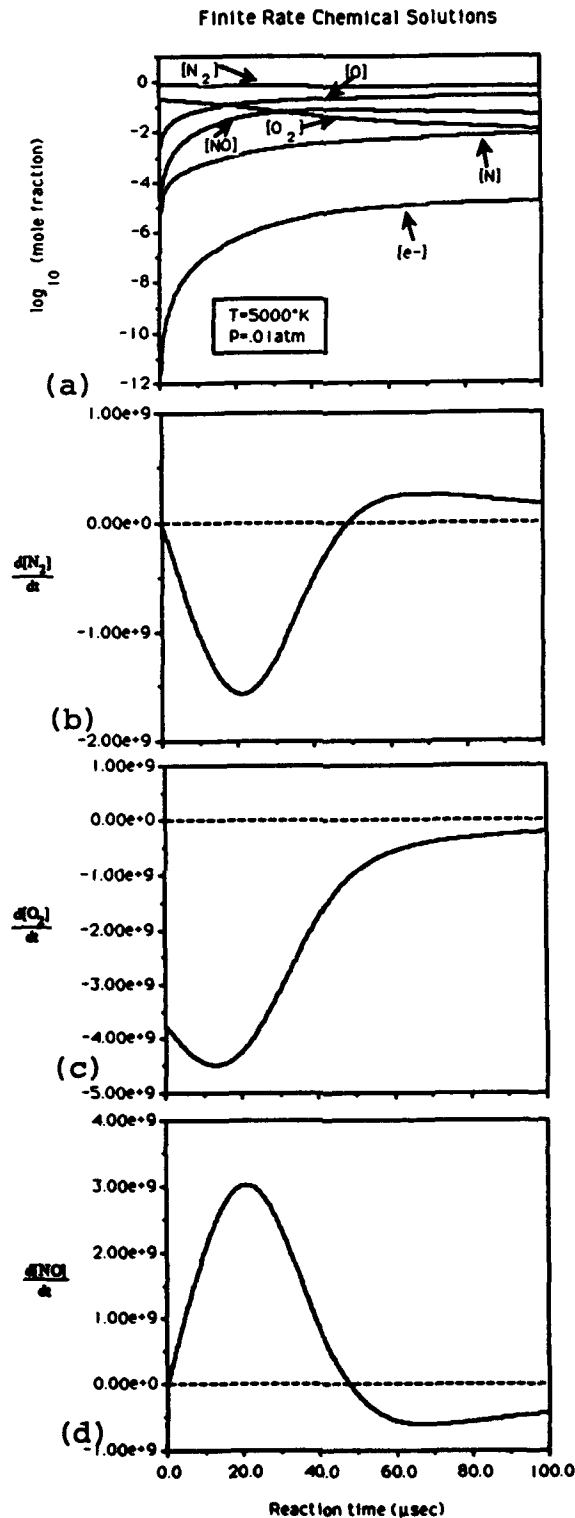
(continued)

Figure II-4. Finite Rate Kinetics for a Gas Temperature of 5000°K. Initial Conditions 79 percent N₂, 21 percent O₂.

II-13

2e+8

1e+8

5e+7

0e+0

$\frac{d[N]}{dt}$

(e)

8.00e+9

6.00e+9

4.00e+9

2.00e+9

0.00e+0

$\frac{d[O]}{dt}$

(f)

4.00e+5

3.00e+5

2.00e+5

1.00e+5

0.00e+0

$\frac{d[e^-]}{dt}$

(g)

0.0   20.0   40.0   60.0   80.0   100.0

Reaction time (μsec)
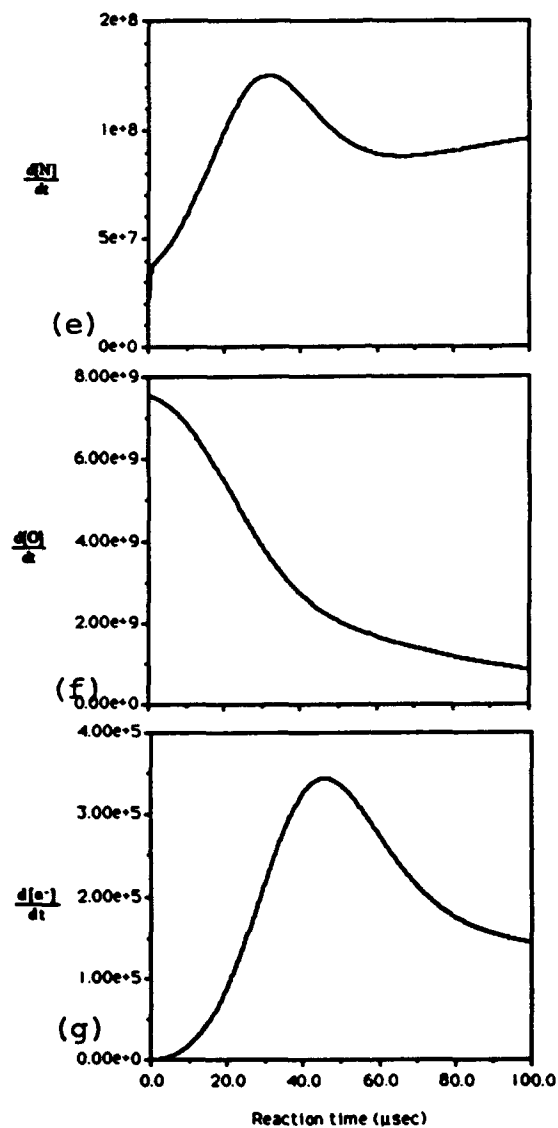
Figure II-4.   (Continued)

The kinetics results shown so far were generated assuming that, initially, there are only N_2 and O_2 present. Standard atmospheric models (Refs. II.B-8, -9, -10), however, show that at 40 km there are trace amounts of O, NO, and O_3 present. The effect that these species would have on the NO concentration was examined. Since ozone will be dissociated at a temperature of 1000°K or greater (Ref. II.B-11), its principal effect is to increase the atomic oxygen concentration in the free stream. The calculations were repeated with free stream conditions chosen to correspond to the above referenced atmospheric models. At temperatures of 5000°K and higher, no differences were observed in species

concentrations produced by 10 μsec of reaction time, regardless of the atmospheric model chosen. Yet comparison of kinetic model results obtained with only N_2 and O_2 initially present, versus trace atmospheric species initially present, showed significant differences. At a temperature of 4000°K or higher, atomic oxygen was found to be the initial chemistry initiator, with about two orders of magnitude more NO formed by 10 μsec.

Since the kinetic modeling indicated a sensitivity to atomic oxygen concentration, the full flowfield and radiation calculation were repeated with the free stream mass fraction of O and NO increased from 10^{-12} to 10^{-6} at 50 km altitude. At a speed of 3.5 km/sec, we obtained no difference in the NO gamma-band radiation calculated. At a weaker shock condition of 3.0 km/sec, a factor of 4 difference was obtained. This is probably due to the effect of lower temperatures, and less NO being produced. Thus, the majority of radiation is produced by the NO initially present. Under weaker shock conditions the flowfield solution was found to be more sensitive to initial boundary conditions or equivalently, initial trace species.

In conclusion, the examination of the kinetics as presently incorporated in the models shows the continued need for full finite rate chemistry for our flight regime of interest. Differences in rate constants that exist in the literature do not appear to cause large differences in a pure kinetic analysis and, therefore, are unlikely to be large factors in the flow modeling.

REFERENCES, CHAPTER II.B

II-B.1 G.V. Candler, *The Computation of Weakly Ionized Hypersonic Flows in Thermo-Chemical Nonequilibrium*, dissertation for Ph.D. in Aeronautics and Astronautics, Stanford University, June 1988.

II-B.2 IMSL, Inc., *MATH/LIBRARY*, Vol. 2, p. 640, Version 1.0, April 1987.

II-B.3 C. Park, *Problems of Rate Chemistry in the Flight Regimes of Aero-Assisted Orbital Transfer Vehicles*, AIAA-84-1730, June 1984.

II-B.4 C. Park, *On Convergence of Computation of Chemically Reacting Flows*, AIAA-85-0247, January 1985.

II-B.5 C. Park, *Two-Temperature Interpretation of Dissociation Rate Data for N_2 and O_2*, AIAA-88-0458, January 1988.

II-B.6 C. Park, *Assessment of Two-Temperature Kinetic Model for Ionizing Air*, AIAA-87-1574, 1987.

II-B.7 T.R. Bussing and S. Eberhardt, *Chemistry Associated with Hypersonic Vehicles*, AIAA-87-1574, 1987.

II-B.8 E. Bauer, The Structure of the Earth's Atmosphere-Lecture Notes," Institute for Defense Analyses, IDA Paper P-811, January 1972.

II-B.9 M. Bortner and R. Kummler, *The Chemical Kinetics and the Composition of the Earth's Atmosphere*, GE-9500-ECS-SR-1, 24 July 1968.

II-B.10 *Suggested Natural Variations in Atmospheric Minor Neutral Species*, prepared by General Electric Company, Contract Report ARBRL-CR-00375, July 1978.

II-B.11 R.J. Kee, F.M. Rupley, J.A. Miller, *The Chemkin Thermodynamic Data Base*, Sandia Report SAND87-8215•UC-4, April 1987.

C. DESCRIPTION AND SENSITIVITY ANALYSES OF THE RADIATION MODEL

1. Introduction

As shown in Fig. II-2, the model used to calculate bow shock irradiance for both flowfield codes is called NEQAIR (Refs. II.C-1 and -2). In this section, the specific physical mechanisms used in determining the excited electronic state populations, and hence the amount of UV radiation computed, is discussed.

As Fig. S-1 shows, the flowfield and aforementioned radiation model NEQAIR predict predominantly NO (γ) band radiation in the UV spectral region, under our flight conditions. In our examination of the radiation modeling in the 2500Å spectral regime we explored three issues: (1) conditions that produce the maximum radiation, (2) adequacy of a presently modeled recombinative excitation mechanism, and (3) neutral collisionally induced excitation of NO. The results of these investigations are presented in this section. Electron excitation/de-excitation mechanisms of NO have been considered elsewhere (Refs. II.C-1 and -2), and for our purposes were assumed adequate.

The NO molecule is modeled in NEQAIR as a three-level system comprised of the X, A, and B electronic states. X is the designation for the ground electronic state, and NO γ and β band UV emission originates from the A and B electronic excitation states, respectively.

References II.C-1 and -2 describe NEQAIR in detail. The emphasis, however, in both these references is on electron-atom and electron-molecule excitation and de-excitation mechanisms that predominate at reentry velocities. Since, in our flight regime, neutral collisional mechanisms are also potentially significant relative to electron excitation mechanisms, we present here the explicit equations used in the code to elucidate all the mechanisms used for NO excitation and de-excitation. The relative importance of different mechanisms were checked by varying the different rates involved.

The solution of the Navier-Stokes equations in the flowfield codes utilizes chemical kinetics of ground state chemistry only. The distinct gas temperatures from the flowfield computation, and the ground state species densities are input to NEQAIR. The quasi-steady state (QSS) approximation is invoked to calculate the electronic excited state population distribution separately for each atomic and molecular species in the flow. This approximation assumes that the electronic state excitation and de-excitation rates are much

faster than the difference between them. It is believed to be valid for the flight conditions of interest to us here. Thus, it can be assumed that the time rate of change of the population of the excited state atoms or molecules is zero (although the population in the excited state does not necessarily have to be Boltzmann). Once the excited state population is obtained, the emission intensity can be calculated using standard transition probability values for the species of interest. The NEQAIR code has the detail to provide line-by-line emission predictions including collisional broadening effects. To date, we have assumed self absorption effects to be negligible. It will be shown (Section II.C.4) from an analysis of the properties of the flow to be a valid assumption. This approximation allowed us to reduce significantly the computational time expended.

2. Quasi-Steady State Equations for NO

Following the formalism and notation given in Refs. II.C-1 and -2, the QSS equations for molecular NO are given as

$$\left\{ \sum_j \left(K_{ij}^e + \sum_l K_{ij}^{n_l} \frac{n_l}{n_e} \right) + \left(K_{ic} + K_{im_{tot}} \frac{n_{m_{tot}}}{n_e} \right) + \frac{\sum_j A_{ij} + A_{ic} + \sum_l A_{il}}{n_e} \right\} \rho_i$$

$$- \left\{ \sum_j \left(K_{ij}^e + \sum_l K_{ij}^{n_l} \frac{n_l}{n_e} + \frac{n_{jE}}{n_{iE}} \right) \rho_j \right\} = \left(K_{ic} + K_{im_{tot}} \frac{n_{m_{tot}}}{n_e} \right) \tag{1}$$

$$+ \left(A_{ci} N^+ + \sum_m A_{mi} \frac{n_o n_N}{n_e} \right) \frac{1}{n_{iE}} \quad ,$$

where

n_e is the number density of electrons (cm^{-3}).

n_l is the number density of heavy or neutral particle of the lth species (cm^{-3}).

$n_{m_{tot}}$ is the total number density of neutral species (cm^{-3}).

N^+ is the number density of ions (cm^{-3}).

K_{ij}^e is the electron induced excitation rate coefficient from the j to ith electronic state of NO (cm^{-3}/sec--binary, cm^6/sec--ternary).

$K_{ij}^{n_l}$ is the corresponding excitation rate coefficient by neutral particle collisions.

K_{ic} is the rate coefficient for ionization of a bound excited electron of an atom or molecule by electron impact from the ith electronic state into the continuum (denoted c).

$K_{im_{tot}}$ represents the corresponding neutral collisionally induced dissociation of NO in its "i^{th}" electronic state by a third body type to form N and O.

A_{ij} is the radiative transition probability from electronic state i to j (sec $^{-1}$).

A_{ic} is the same as above for an electron ejected from the ith electronic state of NO into the continuum to form NO$^+$.

A_{il} is the corresponding term for molecular decomposition to form N and O.

The subscript E represents equilibrium on Boltzmann conditions. Also,

$$\rho_i \equiv n_i / n_{iE} \quad \quad (2)$$

The convention used in the above terms is as follows:

$$\frac{dn_i}{dt} = K_{ji}^e \, n_e n_j \quad \quad (3a)$$

$$\frac{dn_i}{dt} = K_{ci} \, N_+ \, n_e^2 \quad \quad (3b)$$

$$\frac{dn_i}{dt} = K_{ji}^{n_l} \, n_l n_j \quad \quad (3c)$$

$$\frac{dn_i}{dt} = K_{m_{tot}i} \, n_O \, n_N \, n_{m_{tot}} \quad , \quad \quad (3d)$$

where the corresponding excitation mechanisms are, respectively,

$$e^- + NO(j) \rightarrow e^- + NO(i) \quad \quad (4a)$$

$$NO^+ + e^- + e^- \rightarrow NO(i) + e^- \quad \quad (4b)$$

$$n_l + NO(j) \rightarrow NO(i) + n_l \quad \quad (4c)$$

$$N + O + M \rightarrow NO(i) + M \quad . \quad \quad (4d)$$
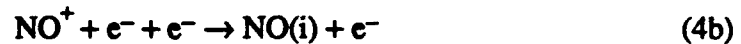
In NEQAIR there is no explicit coupling between the NO electronic state distribution and those of other species in the flow. In the implementation of Eq. (1), in fact, the terms involving a summation over the 1 neutral species is replaced by a generalized

ramp cross section, which is a good approximation in part of our flight regime. Also, terms such as A_{ic}, A_{il}, and A_{ci} are neglected.[5]

Invoking the mass conservation relationship

$$n_{tot} = \sum_i n_i \quad , \tag{5}$$

coupled with Eq. (1) for the ith excited state, yields a matrix of liner equations which are solved to determine each ρ_i

$$\rho_i = \left[M_{ij} \right]^{-1} \left(C_j + D_j \frac{n_{tot}}{n_{totE}} \right) \quad , \tag{6a}$$

where

$$C_1 = 0 \tag{6b}$$

$$C_j \underset{j>1}{=} K_{jc}^e + K_{jm_{tot}} \frac{n_{m_{tot}}}{n_e} \tag{6c}$$

$$D_1 = \frac{n_{tot}}{n_e} \tag{6d}$$

$$D_j = 0 \qquad j \neq 1 \quad . \tag{6e}$$

For $i = 1$,

$$M_{1j} = \frac{n_{jE}}{n_e} \quad , \tag{6f}$$

and for $i \neq 1$,

$$M_{i,i} = \sum_{\substack{j=1 \\ j \neq 1}}^{m} \left\{ K_{ij}^e + K_{ij}^{nl} \frac{n_1}{n_e} \right\} + \sum_{j=1}^{m} \frac{A_{ij}}{n_e} + K_{ic} + K_{im_{tot}} \frac{n_{m_{tot}}}{n_e} \tag{6g}$$

$$M_{ij} = - \left\{ K_{ij}^e + K_{ij}^{n_1} \frac{n_1}{n_e} + \frac{n_{jE}}{n_{iE}} \frac{A_{ji}}{n_e} \right\} \quad . \tag{6h}$$

---

[5] These are the types of processes, i.e., NO + hυ $\xrightarrow{A_{ic}}$ NO$^+$ + e$^-$, which for our velocity regime are not significant.

While the forms of equations (6a) through (6h) explicitly show only the forward excitation mechanisms, the reverse de-excitation mechanisms are related to the former through the equilibria constants. The equilibria constants are calculated using standard molecular and atomic system energy levels and degeneracy parameters. All equilibria constants related to electron induced mechanisms as well as equilibrium number densities are calculated with temperatures from the flow field. The interrelationship between neutral collisional induced forward and reverse reactions utilizes the heavy particle translational temperature, T.

Since NO is modeled as a three-level system, the relative magnitudes of electron and neutral contributions to the excitation/de-excitation processes can easily be examined. Table II-2 shows an example of the various rate coefficients for flowfield conditions corresponding to a grid point along the stagnation streamline where the peak radiation was observed. Under these conditions the translational, and vibrational-electronic vibrational, gas temperatures were 4412°K, and 4761°K, respectively. Examination of these values provides a number of interesting observations: (1) de-excitation mechanisms predominate, (2) electron and neutral induced mechanisms are roughly the same order of magnitude (at least for X → A), and (3) decomposition mechanisms which are destructive in terms of upper state population are competitive with excitation by neutrals.

Table II-2. Rate Coefficient Values For Excitation Mechanisms[a,b]

Transition	Electron Contribution	Neutral Contribution
	COLLISIONAL EXCITATION/DEEXCITATION K_{ij}^{e}	K_{ij}^{nl}
X → A	$7.02 \times 10^{-17}/1.21 \times 10^{-10}$	$1.06 \times 10^{-17}/5.24 \times 10^{-11}$
X → B	$8.67 \times 10^{-15}/3.09 \times 10^{-9}$	$3.62 \times 10^{-18}/6.02 \times 10^{-12}$
A → B	$0.0/0.0$	$5.03 \times 10^{-12}/1.09 \times 10^{-12}$
	DECOMPOSITION K_{ic}	DEEXCITATION $K_{im_{tot}}$
X	3.36×10^{-17}	7.97×10^{-16}
A	9.37×10^{-12}	1.38×10^{-12}
B	1.59×10^{-11}	2.50×10^{-12}

[a] Units are in cm^3/particle sec.

[b] This corresponds to 3.5 km/sec, 40 km, r_n = 3-in. conditions, T = 4412°K, T_v = 4761°K.

Table II-3 gives the populations obtained in the QSS approximation solution. These are obtained by solving Eqs. (6a) through (6h) using the values from Table II-2. The equilibrium population is also given and is shown to be approximately 30 percent higher for excited states than that predicted by QSS. While it cannot be proven in a rigorous sense, it is reasonable to argue that, under these gas conditions, the Boltzmann population represents the maximum A and B state populations achievable. Any additional changes in specific excitation cross sections proposed will have less than a proportional effect on increasing the excited state population, and hence radiation. The results presented so far were obtained using the original version ("base case") of NEQAIR provided to us by C. Park. Per recommendations suggested by G. Smith of SRI and C. Park of NASA/ Ames, additional changes were examined which will be enumerated below.

Table II-3. QSS Solution from Table II-5 Results

Population (molecules/cm^3)

	X ($^2\Pi$)	A ($^2\Sigma^+$)	B ($^2\Pi$)
QSS	3.07×10^{16}	1.401×10^{10}	5.08×10^{10}
Boltzmann	3.07×10^{16}	1.78×10^{10}	8.59×10^{10}

The ratio of QSS to Boltzmann excited state populations were also found to hold at other grid points along the stagnation stream line where appreciable radiation was produced. Figure II-5 provides specific examples of this for the same conditions given in Table II-2. Radiance numbers are integrated from 2250 to 2750 Å, with all relevant radiating species included. Values are given for spatial locations starting near the body and proceeding out towards the shock wave. Temperature values T and T_v are obtained from inversion of the translational and vibrational conservation of energy relationships.

Finally, the excitation mechanisms of the NO molecule cannot really be examined in isolation from the rest of the gas. Since N$_2$ composes roughly 78 percent of the flow, examination of its population distribution is of importance. Under the conditions given in Table II-2, for the brightest part of the flow, the QSS and Boltzmann N$_2$ number density distributions are:

Values in molecules /cm^3		X	A($^3\Sigma_u^+$)	B($^3\Pi g$)	a($^1\Pi g$)
QSS	:	5.58×10^{17}	7.41×10^{11}	6.48×10^{10}	1.22×10^9
Boltzmann	:	5.58×10^{17}	11.65×10^{10}	9.50×10^{10}	1.78×10^9
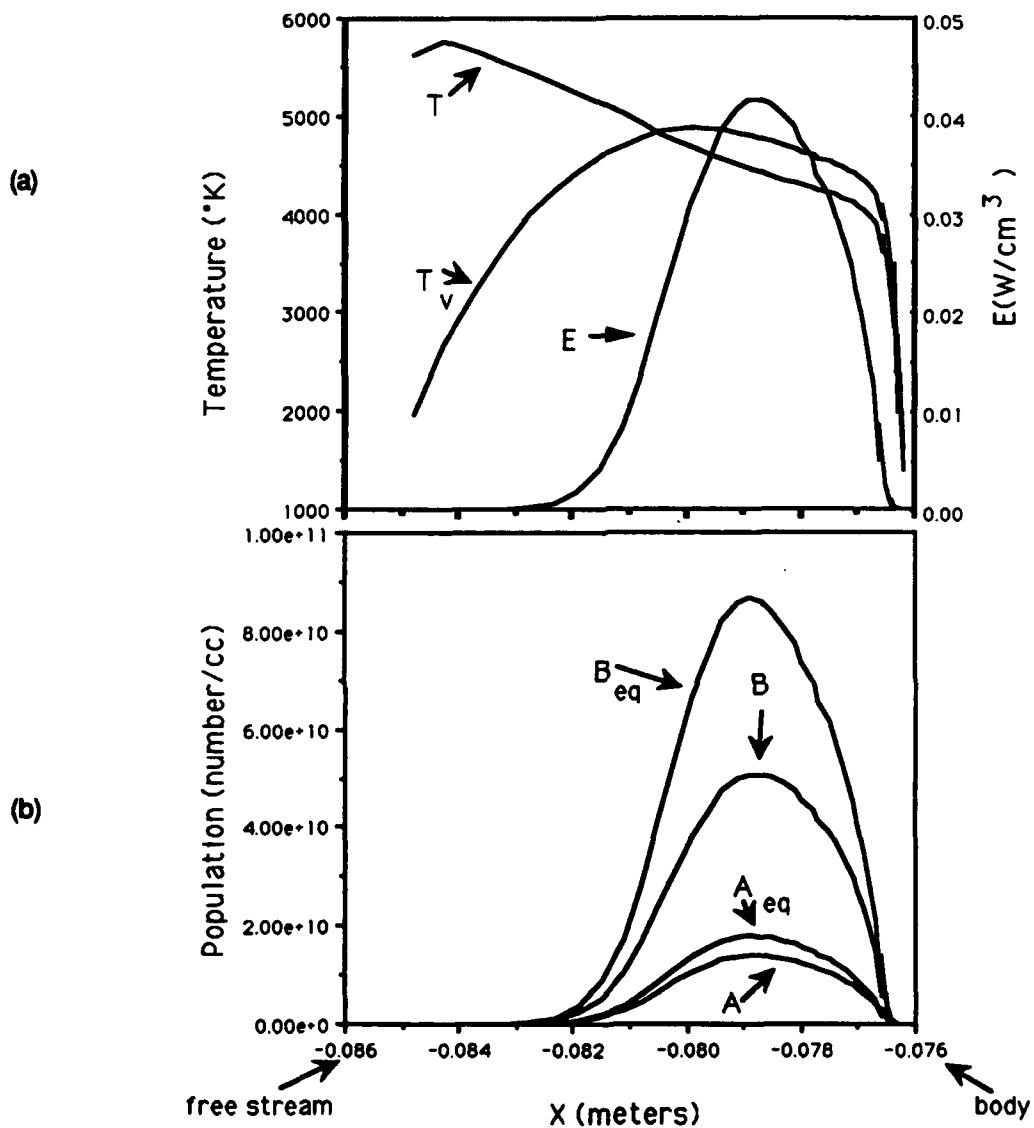
(a) Comparison of heavy particle temperature, T, vibrational temperature, T_v, and radiance, E.

(b) Comparison of A and B state populations in the QSS versus Boltzmann equilibrium models.

Figure II-5. Baseline Comparison of QSS Versus Equilibrium Population Distributions for Different Locations Along Stagnation Streamline.

The fact that the species present in the largest concentration is so close to Boltzmann equilibrium conditions argues that it is unlikely that there will exist any physical processes large enough to create an excited state population larger than the Boltzmann limit.

3. Sensitivity Analyses

During the course of our work, a number of suggestions were generated regarding possibly important excitation mechanisms that *may have* been neglected in NEQAIR (summarized in Ref. II.C-3). The three mechanisms that were singled out were:

$$N + O + M \rightarrow NO^* + M \tag{7a}$$

$$N_2(A) + NO(X) \rightarrow N_2(X) + NO(A) \tag{7b}$$

$$NO^+ + e^- \rightarrow NO^* \quad . \tag{7c}$$
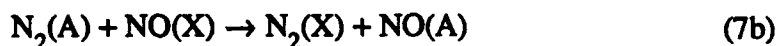
On closer inspection, we determined that, in fact, all of these mechanisms are included in NEQAIR in a semi-empirical approach which appears to work at conditions of 3.5 km/sec and 40 km altitude. However, because the NO^+ concentration in the flow is small, we decided to concentrate on investigating the impact of changing rate parameters in Eqs. (7a) and (7b). In the above equations, M represents a third body and NO^* denotes an excited state of that molecule. In addition to these specific changes, other general sensitivities were also examined, and will be summarized in this subsection below.

Equation (7a) represents a mechanism to populate excited states of NO through a three body recombination process. As already shown in Eqs. (3a) and (4b) above, this mechanism is approximated in the solution of Eq. 6. The specific rate data that is programmed in NEQAIR was taken from Ref. II.C-4. Alternative rates were proposed by Gross and Cohen (Ref. II.C-5) from their experiments in a glow discharge shock tube. They assessed their presented rates to be valid over a temperature range of 300 to 2000 °K. Under the conditions of their experiment, NO gamma and beta band radiation was measured. Excited and ground dissociation rates can be inferred from these measurements. The rate for formation of NO in the ground state, and production of a gamma band photon is

$$N + O + (N_2) \rightarrow NO + (N_2) + h\upsilon(\gamma) \quad , \tag{8a}$$
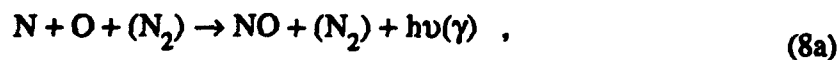
where all species are in the ground state and

$$\frac{d[NO]_i}{dt} = \left\{ 10^{-16.9} \left(\frac{300}{T}\right)^{0.35} + 10^{-33.8} \left(\frac{300}{T}\right)^{1.24} [N_2] \right\}$$

$$\times [N][O] \frac{particles}{cm^3 \; sec} \quad , \tag{8b}$$

where i denotes either the X or A state. Determination of the population of the B state from measurement of beta band radiation is not as straightforward. The presence of other closely lying electronic states complicates the analysis. The following equation (Ref. II.C-5) can be used specifically for the B state.

$$\frac{d[NO]_i}{dt} = \frac{1}{35} \times 10^{-33.52} \left(\frac{T}{300}\right)^{-1.4} [N][O][N_2]$$

$$particles/cm^3 \; sec \quad . \tag{8c}$$

The subscript i is as defined above. To compare with NEQAIR (where the reverse rate, a dissociation rate, is given) Eqs. (8b) and (8c) must be multiplied by the respective equilibria constants.

The dissociation rate coefficient used in NEQAIR is of the form

$$k_{dissoc} = \chi_{atom} \times (0.184) + \chi_{molec} \times (4.56 \times 10^{-7}) \times T^{-1.6} \exp(-[D_e - T_e]/kT) \quad , \tag{8d}$$

where χ_{atom} and χ_{molec} are the fraction of atomic and molecular species in the flow, D_e and T_e are the dissociation limit and term value of the excited state level, respectively. The numerical values given in Eq. (8d) (i.e., .0184 and 4.56×10^{-7}) are specific to NO and are independent of electronic level.

Table II-4 gives a summary of the calculations and a direct comparison for the two sets of rates. The molecular parameters taken for D_e and T_e conform to those shown in potential energy curves of Gilmore (Ref. II.C-6). The first conclusion one can draw is that the rate presently given in NEQAIR for the A state dissociation is actually almost an order of magnitude *less* than that given by Gross and Cohen. Hence the former would tend to predict slightly more radiation, rather than less (as was thought earlier by the people who proposed changing these rates) since population is being lost more readily from the A state through dissociation. Table II-4 also shows that there is a larger difference in the A and B state dissociation rates predicted by Gross and Cohen, versus Park (NEQAIR). There is even a reversal in the relative sizes. Examination of Eq. (8d) and the footnotes of

Table II-4 shows that two A and B state rates of Park are explicitly related to each other by a factor of exp $[-(D_{eA} - D_{eB})/kT]$ or .5475 at T = 4700°K. If the Gross and Cohen values were assumed correct and the B state value was adopted, this would also tend to decrease the amount of gamma band radiation through the coupling of the three electronic states in Eq. (6). The magnitude of the decrease would be mitigated because of the lower transition probability of radiation for the B, versus the A state.

Table II-4. Tabulation of Comparison Between Collisional Dissociation Rates of NO in NEQAIR and Gross and Cohen.[a]

T = 4700 °K, $\chi_{atom} \cong 0.1$, $\chi_{molec} \cong 0.9$

Equilibrium Constant	Gross & Cohen $k_{dissoc.}$	Park $k_{dissoc.}$
A State		
7.10×10^{23}	4.89×10^{-12}	5.0×10^{-13}[b]
B State		
1.49×10^{23}	2.74×10^{-14}	9.1×10^{-13}[c]

[a] All units are in molecules/cc.

[b] D_e, T_e used were 71,718 and 43,965 cm^{-1}, respectively.

[c] D_e, T_e used were 71,718 and 45,933 cm^{-1}, respectively.

In summary, a comparison between the dissociation rates as predicted by experiment and theory was made. The comparison, however, could not be made exactly. To implement rigorously the proposed Gross and Cohen mechanistic interpretation of their data in NEQAIR would require further generalization of the QSS equations to include coupling between all atomic and molecular systems in the flow. For example, note that the present implementation of Eq. (7a) in NEQAIR is not NO(A) formed from the ground state atomic levels but rather from the A state dissociation limit. In making this comparison we are using the approximation, which we feel is valid here, that the details of the total mechanism are dominated by the potential energy barrier of the NO excited states. For energetic reasons, we ignore the next highest C state as well.

The second potentially important mechanism examined was energy exchange from the $N_2(A)$ state exciting NO in its ground state through collisions, Eq. (7b). The K_{ji}^{ne} rate coefficient [see Eq. (3c)] for neutral collisional induced excitation is represented in NEQAIR as a generalized ramp cross section

$$K_{ij}^{nl} = 4057 \, kT^{1/2} \, \sigma e^{-x} \left\{ \frac{x^2 + 2.334733x + 0.250261}{x^2 + 3.330657x + 1.681534} \right\} \quad , \qquad (9a)$$

where

$$x \equiv \frac{T_e^u - T_e^l}{kT} \quad , \qquad (9b)$$

and T_e^u, T_e^l, and T are the energy term values for the upper and lower electronic states, and T is the heavy particle temperature, respectively. The present value used for σ in NEQAIR is 1.0×10^{-16} cm^2 and is the same for all molecular systems. Figure II-6 shows a plot of Eqs. (9a) and (9b). For NO, however, other work (Ref. II.C-7) indicates that such a collisional excitation process is more efficient, i.e., σ is about a factor of ten higher.
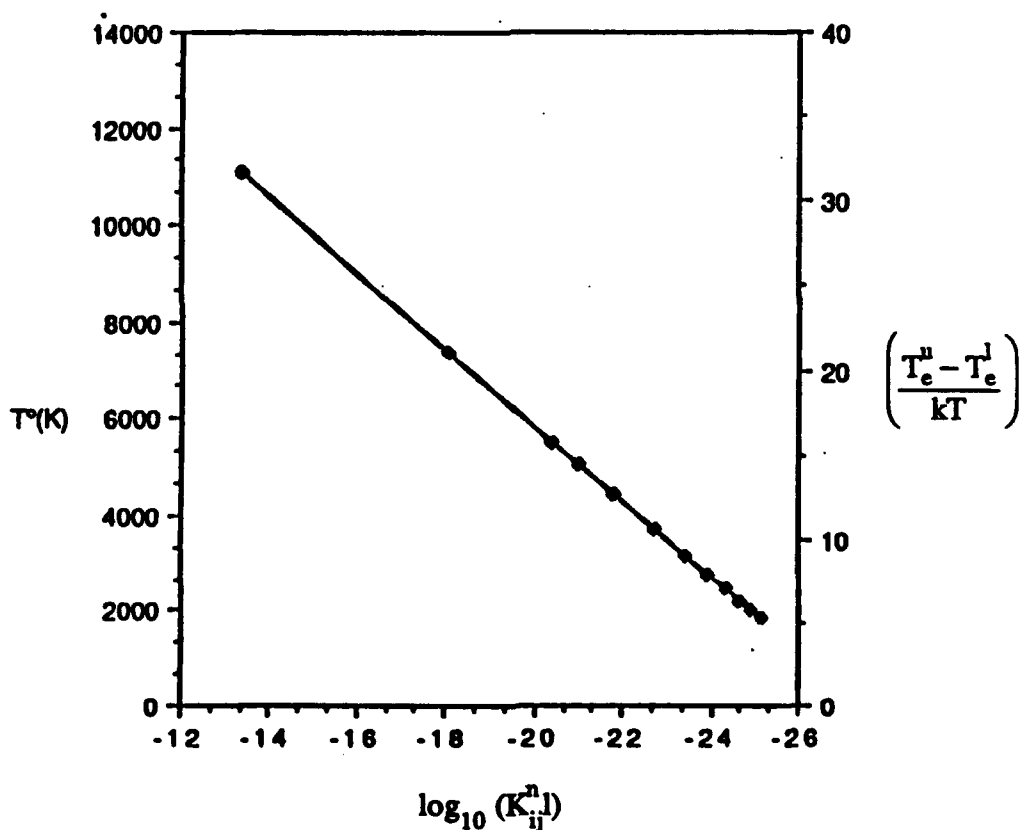

Figure II-6. Ramp Cross Section Functional Form

Results from one such experiment (Ref. II.C-7), although at room temperature, gives a value of $K_{X \to A}^{nl}$ equal to $(10 \pm 3) \times 10^{-11} \frac{cm^3 molec}{sec}$. While this rate

coefficient is many orders of magnitude larger than the value given in Table II-2 $\left(\text{namely, } 1.06 \times 10^{-17} \frac{cm^3 molec}{sec}\right)$, its use is different. If Eq. (3c) represents the forward rate equation for (7b) then n_i, n_j, and n_l are the concentrations of NO (X), NO(A), and $N_2(A)$ states, respectively. However, when Eq. (9) is used, n_l is the total molecular concentration in the flow. Using the earlier values of $N_2(A)$ obtained from the QSS solution, $7.41 \times 10^{11} \frac{molec}{cm^3}$, the total flow molecular density of $7.422 \times 10^{17} \frac{molec}{cm^3}$ provides a comparison of the ratio, $\frac{1}{n_{NO(X)}} \frac{dn_{NO(A)}}{dt}$, computed using the value of Ref. II.C-7, or the presently programmed Eqs. (9a) and (9b) as

$$\frac{1}{n_{NO(X)}} \frac{dn_{NO(A)}}{dt} = \begin{cases} 10 \times 10^{-11} \times 7.41 \times 10^{11} = 7.41 \ (\text{Piper}) \\ 1.1 \times 10^{-17} \times 7.42 \times 10^{17} = 8.2 \ (\text{ramp cross section}) \end{cases} \quad . \quad (10)$$

From the result of Eq. (10), the σ value used is about an order of magnitude too low. Estimates of rates coefficients related to the above comparison were also given in Ref. II.C-5. However, the state specific conditions were not well specified.

Table II-5 summarizes the sensitivity of in-band NO radiation to changes in the rate coefficients discussed above. The reader can also see the effect in populating excited states under hypothetical flow conditions (see rows below the dashed line). One interesting case is for election concentration increased by a factor of 10^4 and no neutral collisional mechanisms; the election impact dissociative mechanisms dominate. This is in agreement with the relative magnitudes shown in Table II-2. *The net result, however, is that except for large changes in T_v and T_e, the changes in radiation are not large.* Further work is needed to investigate the validity of these results, particularly since they may be predetermined in the sense that the model is sufficiently constrained by the use of the QSS approximation.

It should also be re-emphasized that the detailed analysis presented here was done for one velocity/altitude condition, representative of our region of interest, and that the comparison in Table II-5 was done for a single spatial location along the stagnation streamline.

Table II-5. Summary of NEQAIR Sensitivity Runs[a]

Case Description			Population (molec/cc) (W/cm³)			In-Band Radiance
X	A	B				
Base line			3.07×10^{16}	1.40×10^{10}	5.08×10^{10}	0.0416
Gross & Cohen, $K_{im_{tot}} \rightarrow K_{im_{tot}} \cdot 10$			3.07×10^{16}	1.19×10^{10}	4.99×10^{10}	0.0376
Ramp cross section increased from 10^{-16} to 10^{-15} $\left(K_{ij}^{n_i} \text{ term} \right)$			3.07×10^{16}	1.73×10^{10}	8.04×10^{10}	0.0571
Electron collisional mechanisms only $\left(K_{ij}^{n_i} , K_{im_{tot}}^{n_i} \text{ set} = 0 \right)$			3.07×10^{16}	1.65×10^{10}	8.55×10^{10}	0.0573
Neutral Collisional Mechanisms only $\left(K_{ij}^{e} , K_{ic} \text{ set} = 0 \right)$			3.07×10^{16}	1.69×10^{10}	6.32×10^{10}	0.0509
$K_{im_{tot}} \rightarrow K_{im_{tot}} /10.$			3.07×10^{16}	1.44×10^{10}	6.33×10^{10}	0.0464
$n_e \rightarrow n_e \times 10^4$, all other terms as in base case			3.07×10^{16}	1.43×10^{10}	6.65×10^{10}	0.0472
$n_e \rightarrow n_e \times 10^4$, electron collisional mechanisms only.			3.07×10^{16}	5.52×10^{8}	7.06×10^{10}	0.0243
$T \rightarrow T = 8000°K, T_v, T_e$ as in base case (4761°K)			3.07×10^{16}	1.47×10^{10}	5.53×10^{10}	0.0404
$T, T_v, T_e \rightarrow 8000°K$			3.07×10^{16}	2.22×10^{12}	3.54×10^{12}	4.034

[a]   Calculations done at grid location corresponding to maximum radiation (E) in Fig. II-5.

4. Optical Thickness of The Gas

In this subsection, the case of an optically thin limit for calculations relevant to this bowshock radiation experiment is justified. This was done to significantly reduce the computational time necessary to calculate radiance values.

Using a straightforward analysis from standard textbook treatments of radiative transport (Ref. II.C-8), the ratio of the exiting to entering radiation, I/I_0, passing through a gas of thickness Δx may be expressed as

$$\frac{I(E)}{I_0} = e^{-\zeta/(1+(E/E_0)^2)} \quad , \tag{11}$$

where

$$\zeta = \frac{v n_1 \Delta x A(u, l)}{8 \pi^2 C^2 E_0^4} \quad , \tag{12}$$

and n_1 is the population of the lower electronic or final state, $A(u, l)$ is the probability of transition from the upper to lower electronic state and v and v_0 are the exiting and incident light frequencies corresponding to energies E and E_0. In our analysis we assumed that v and v_0 are identical. We examined the optical thickness contributions from the species most prominent in the gas for a shock generated at a speed of 6.3 km/sec at 40 km altitude at 2500Å. Table II-6 shows a summary of the analyses. From the table it is easily seen that the largest absorption is due to O_2. The species present in largest concentrations, potential transitions of interest, radiative lifetimes quoted in the literature as well as the optical thickness, $\zeta/2$, are given. The peak mole fraction column does not add to unity since the species concentrations peak at different spatial locations in the flow. The lifetimes given, which are the reciprocal of $A(u, l)$ of Eq. (12), are not necessarily the exact values given in NEQAIR. The values shown in the table were obtained from Refs. II.C-9 and -10 and serve to summarize the values used in the chemistry and high temperature communities. The values actually used in NEQAIR fall within the range of numbers suggested by the above two references.

The results of Table II-6 show that only a one percent error is made in ignoring absorption in the gas at speeds of 6.3 km/sec. At the slower speeds of interest to us, less O_2 will be dissociated, which would increase the optical thickness of the gas. However, we estimate that, in the worst case, the error would only be a few percent.

5. Conclusions

The above subsections addressed the adequacy of the present NEQAIR model as well as optical thickness conditions in the gas.

Table II-6. Major Flow Field Species and Transitions Optical Thickness Conditions for $v = 6.3$ km/sec, $H = 40$ km, $r_n = 7.62$ cm at 2500Å

Major Species	Peak Mole[a] Fraction	Strong Transitions at 2500Å (sec)	Typical Lifetime	$N_i \Delta X$, Peak (molec/cm^2)	$\zeta/2$
NO	0.075	Gamma Bands[b] $(A)^2\Sigma^+ \rightarrow (X)^2\pi$ @ 44,078 cm^{-1}	2×10^{-7}	2.75×10^{14}	4.53×10^{-6}
		Beta Bands[b] $(B)^2\pi \rightarrow (X)^2\pi$ @ 45,394 to 45,481.7 cm^{-1}	1.9 to 1.8 $\times 10^{-6}$	2.75×10^{14}	4.53×10^{-7}
N	0.5	None	N/A	N/A	N/A
N$_2$	0.8	Vegard-Kaplan bands @ 49,755 cm^{-1} $(A)^3\Sigma_u^+ \rightarrow (X)^1\Sigma_g^+$	1.5	7.9×10^{17}	1.74×10^{-9}
O	0.275	None	N/A	N/A	N/A
O$_2$	0.2	Schumann-Runge[c] $(B)^3\Sigma_u^- \rightarrow (X)^3\Sigma_g^-$ @ 49,363 cm^{-1}	1.3×10^{-9} to 1.1×10^{-8}	4×10^{15}	0.01 to 0.001

[a] Peak mole fractions of N$^+$, O$^+$, N$_2^+$, NO$^+$ were 6.5, 3.0, 0.475, 0.35, and 6.8×10^{-4}, respectively.

[b] K.P. Huber and G. Herzberg, *Molecular Spectra and Molecular Structure*, Vol. IV, Constants of Diatomic Molecules, 1979.

[c] N.C. Nardone and Breene, *Radiance of Species in High Temperature Air*, DTIC #408564.

From the analyses, we would recommend that the values obtained from the Gross and Cohen measurements for the formation of NO in the ground and excited states be incorporated into the model. In addition, the ramp cross section value of 10^{-16} cm^2 should be enlarged by an order of magnitude for NO only, per the work of Piper and co-workers. Their two changes will roughly cancel each other out in terms of predicting excited state populations for the flight regime considered in this paper. Because of this we decided to use the codes in their original form.

From the remainder of the sensitivity runs made it appears that:

* The use of a generalized ramp cross section to represent the details of neutral-neutral collisional excitation is adequate for low altitudes and vibrational temperatures on the order of 5000°K.

* The population values are very close to equilibrium conditions and, as such, probably represent the maximum limit of radiation achievable.

It should be noted that for future applications, if found necessary, the QSS formalism can be generalized to permit explicit coupling between electronic levels of different species. This, of course, has a negative impact on computational time.

As was also discussed above, the NO molecule is modeled as a three-level system here. In terms of NO's capability as a radiating source, it is degraded by the presence of the B excited state. As Table II-6 shows, the oscillator strength (related to lifetime) of the B state (beta bands) is about one-tenth of the A state. Energetically, however, the two are roughly comparable in terms of accessibility. The rates in Table II-2 reflect this. Any new collisionally induced rates would also show the same trend. As a result, the population distributions always predict comparable amounts of population in the two excited states. The OH radical, in contrast, has an electronic structure without the near degeneracy observed in NO. With its large oscillator strength and smaller energy gap (3060Å versus 2270Å) it might be another important candidate for bowshock radiation. The present version of the flowfield codes, however, does not have the capability to model this species.

Finally, the assumption of an optically thin gas is valid in the wavelength range under consideration for our selected flight conditions. For future work, particularly in the VUV, this would not be expected to be valid, however. The NEQAIR model transport equations and data base will be reexamined, if required, at that time.

REFERENCES, CHAPTER II.C

II.C-1. C. Park, "Calculation of Non-equilibrium Radiation in the Flight Regimes of Aero-Assisted Orbital Transfer Vehicles," *Thermal Design of Aero-Assisted Orbital Transfer Vehicles: Progress of Astronautics and Aeronautics*, 96, 1985.

II.C-2. C. Park, *Nonequilibrium Hypersonic Aerothermodynamics*, John Wiley & Sons, 1990.

II.C-3. D. Levin, IDA Memorandum for the record, 1 November 1988, "Summary of 7 October (IDA) and 18 October (Space Data Corporation) Meetings."

II.C-4. C. Park and G.P. Menees, *J. Geophys. Res.*, 83, No. 8, p. 4029, August 1978.

II.C-5. R. Gross and N. Cohen, *J. Chem. Phys.*, 48, 2582 (1968).

II.C-6. F.R. Gilmore, *J. Quant. Spectros. Rad. Transfer*, 5, 369 (1965).

II.C-7. L.G. Piper, L.M. Cowles, and W.T. Rawlins, *J. Chem. Phys.*, 85, 3369 (1986).

II.C-8. E.U. Condon and G.H. Shortley, *Theory of Atomic Spectra*, Cambridge University Press, 1985.

II.C-9. K.P. Huber and G. Herzberg, *Molecular Spectra and Molecular Structure*, Vol. IV, Constants of Diatomic Molecules, 1979.

II.C-10. N.C. Nardone and Breene, *Radiance of Species in High Temperature Air*, DTIC # 408564.

D. SHOCK TUBE RADIANCE CALCULATIONS AND COMPARISON WITH EXPERIMENT

1. Introduction

As mentioned earlier, one of the major difficulties in verifying the calculation of boost phase bow shock signatures was the lack of flight or laboratory data in our flight regime. To partially correct this deficiency, Dr. W. Wurstor at CUBRC/CALSPAN conducted survey shock tube measurements. The summary of their data and analyses are given in Refs. II.D-1 and -2. Using the STRAP program described in Section II.A, we tested the model predictions against this new data. Our results are given here. Again, most of the relaxation mechanisms modelled in STRAP are the same as those used in the SPRAP and 2-D codes. Therefore, comparison of the shock tube experimental data with the STRAP/NEQAIR theory is a first order test on how well one can expect to make accurate bowshock radiance predictions. The major technical difference between the shock tube and bowshock is the cool body wall and associated boundary layer present in the latter. The advantage of the shock tube experiments (compared to bowshock experiments) is that they are more easily done in the laboratory.

The results shown here were obtained with minor modifications to the STRAP and NEQAIR modules to conform with the CALSPAN experimental configuration (Ref. II.D-2).

The CALSPAN experiments used a three-inch diameter shock tube. Relative intensity spectra were obtained with an optical multichannel analyzer. Absolute intensity measurements were made with a 260-nm radiometer. Both devices viewed the shock perpendicular to the gas flow. The advantage of this configuration is that it provided us with spatially resolved data along the longitudinal axis of the shock tube. Since we were primarily interested in quantitative comparison of theory and experiment, we concentrated our efforts on the 260-nm radiometric data. However, the spectra obtained brought up some interesting questions on the role of the O_2 (B) state relative to NO(A), which we also comment on. Details of the spectral assignments are given in Appendix B.

2. Comparison with 260 nm Radiometer

Figure II-7 shows a plot of the transmission of the 260 nm filter as a function of wavelength as given by CALSPAN (Ref. II.D-1). Figure II-8 shows the Gaussian filter

function we used in NEQAIR to calculate the total in-band radiance. The function was obtained using a form

$$T = T_o \exp\left(- (\lambda - \mu_o)^2/2\sigma^2\right) \ ,$$ (13)

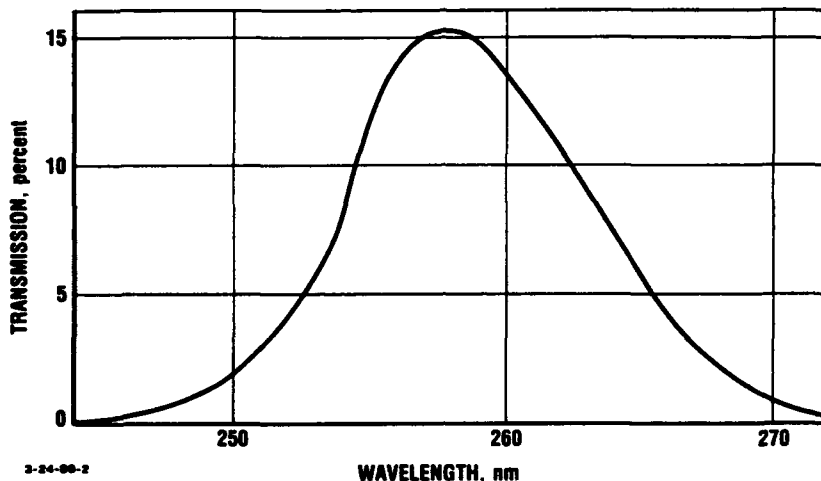where $T_O = 0.15$, $\mu_O = 2590\text{Å}$, and $\sigma = 42.466\text{Å}$.

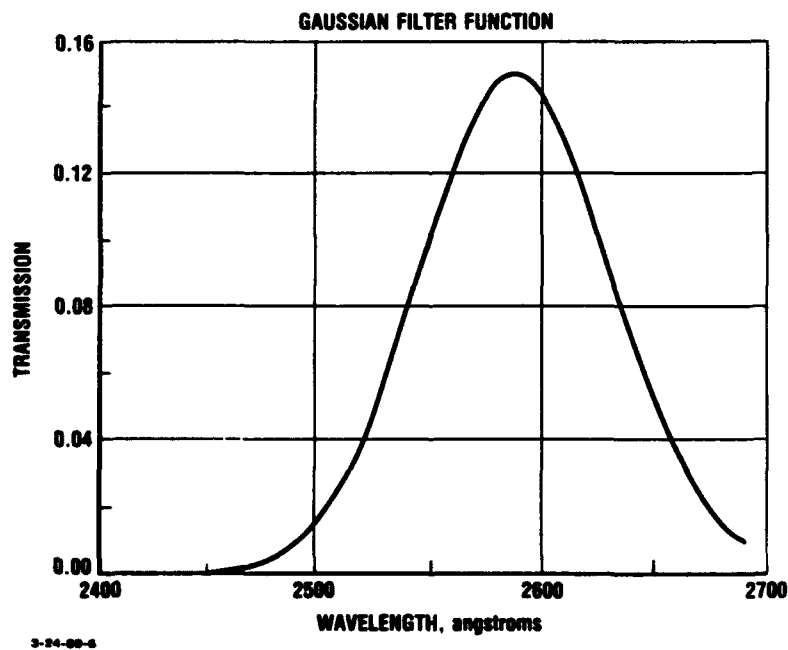**Figure II-7. Transmission of the 260-nm Filter (Fig. 3 of Ref. II.D-1)**

Figure II-8. Filter Function Used in NEQAIR

II-35

The STRAP/NEQAIR calculations were performed at the shock tube axial locations defined by a user supplied grid. Since the experimental radiometer views the shock perpendicular to the gas flow, one must take the finite field of view (FOV) of the radiometer into account when making the theory-experiment comparison. This is done using a spreading function routine in the STRAP/NEQAIR code. The spatial extent corresponding to the radiometer FOV was quoted as 0.3-0.5 cm (Ref. II.D-1), and we used a value of 0.4 cm in the calculations which were directly compared to experiment. However, we also discuss the sensitivity of the absolute magnitude of this function as well.

Table II-6 provides a summary of the runs that were made. The CALSPAN run number index is provided to permit coordination with Ref. II.D-1. Except where noted, the viscous calculation was permitted to extend out to χ_r of 1.5 cm from this shock. χ_r denotes the length of the domain over which the viscous part of the calculation was done. For the weakest shock case examined it was observed that the peak radiation was substantially further (compare 3.46 cm versus 0.982 cm) from the shock front. Hence, χ_r was doubled to test the sensitivity of this parameter. Comparison of the final radiation showed no sensitivity to the χ_r parameter. Except for the second row of the table, the total radiation is given at the peak radiation location from the shock front. *Comparison of theory and experiment shows agreement on the order of a factor of two to three.*

Table II-6. Shock Tube Experiment Compared with Theory[a]

260 nm filter In-band Radiance

Calspan Run	v (km/sec)	h (km)	location (cm)	Exp. (W/cm^{3}sr)	Theory (W/cm^{3}sr)	Theory Exp.
62	3.81	40	0.982	1.1×10^{-4}	2.25×10^{-4}	2.05
62	3.81[b]	40	3.91	1.5×10^{-5}	3.33×10^{-5}	2.22
50	3.50	40	1.50	1.8×10^{-5}	4.41×10^{-5}	2.45
42	3.32	40	2.13	5.4×10^{-6}	1.26×10^{-5}	2.33
48	3.56	50	3.59	5.9×10^{-6}	1.58×10^{-5}	2.68
48	3.56[c]	50	3.46	5.9×10^{-6}	1.57×10^{-5}	2.67
53	3.77	50	2.30	2.2×10^{-5}	5.60×10^{-5}	2.55

[a] Spatial width = 0.4 cm (W. Wurster quoted 0.3 to 0.5 cm), χ_r = 1.5 cm, except as noted peak radiation values in the shock, are given.

[b] Equilibrium portion of shock.

[c] Run with χ_r = 3.0 cm.

Figure II-9 shows a theory/experiment comparison of the peak radiation values using a scaling relationship suggested in Ref. II.D-1. Again, the good agreement for the 260-nm radiometric data can be seen. The scaling that is observed to hold for experiment and theory was not obtained with the theoretical bow shock calculations of the 2-D code (as will be seen in the next section). The results in Table II-6 show that under weaker shock conditions the location of the peak radiances moves further from the shock front, which is also consistent with the results discussed in Appendix A. In the presence of a cool wall, the peak radiation will then be suppressed. Thus, the bow shock data should not provide as straightforward a scaling relationship as do the shock tube results.

In addition to comparing the absolute magnitude of radiation, we also verified the spatial profile of radiation predicted by theory. The actual radiance profile, as a function of location from the start of the shock front, is a complicated function of chemical kinetics, energy exchange relaxation, and excitation/de-excitation processes. Hence, comparison of theory and experiment in this case cannot provide in-depth validation of the modeling, but rather provides qualitative assessment. To compare radiation profiles, we transformed from time (in the laboratory reference frame) to distance (in the reference frame) of the shock (which is what is used in the calculations). The experimental radiance versus time data, for a 3.81 km/sec, 40 km altitude shock tube experiment, was digitized and transformed by multiplying the abscissa by the known shock velocity. In Fig. II-10, the experimental data (dotted line), the unspread theory (infinite simile field of view, solid line) and the spread theory (dashed line) are shown. The theory has been spread with a Gaussian width of 0.4 cm. The relative origins along the abscissa for the three curves are arbitrary and have been shifted for comparison. The actual magnitude of the shift is basically determined by the radiometer window placement in the shock tube. The unspread theory and experimental data vary by a factor of four, whereas when the spreading function is used, the theoretical result is in agreement with experiment by a factor of two (as is shown in Table II-6). This is the proper trend, since accounting for the field of view effectively renormalizes and increases the denominator of the in-band radiance values, thereby lowering the latter. The width of the peaks are in qualitative agreement, with the experimental peak appearing to be slightly broader. Due to other uncertainties in the comparison discussed in Appendix B, we did not try to vary the spreading function any further to obtain better agreement between experiment and theory.
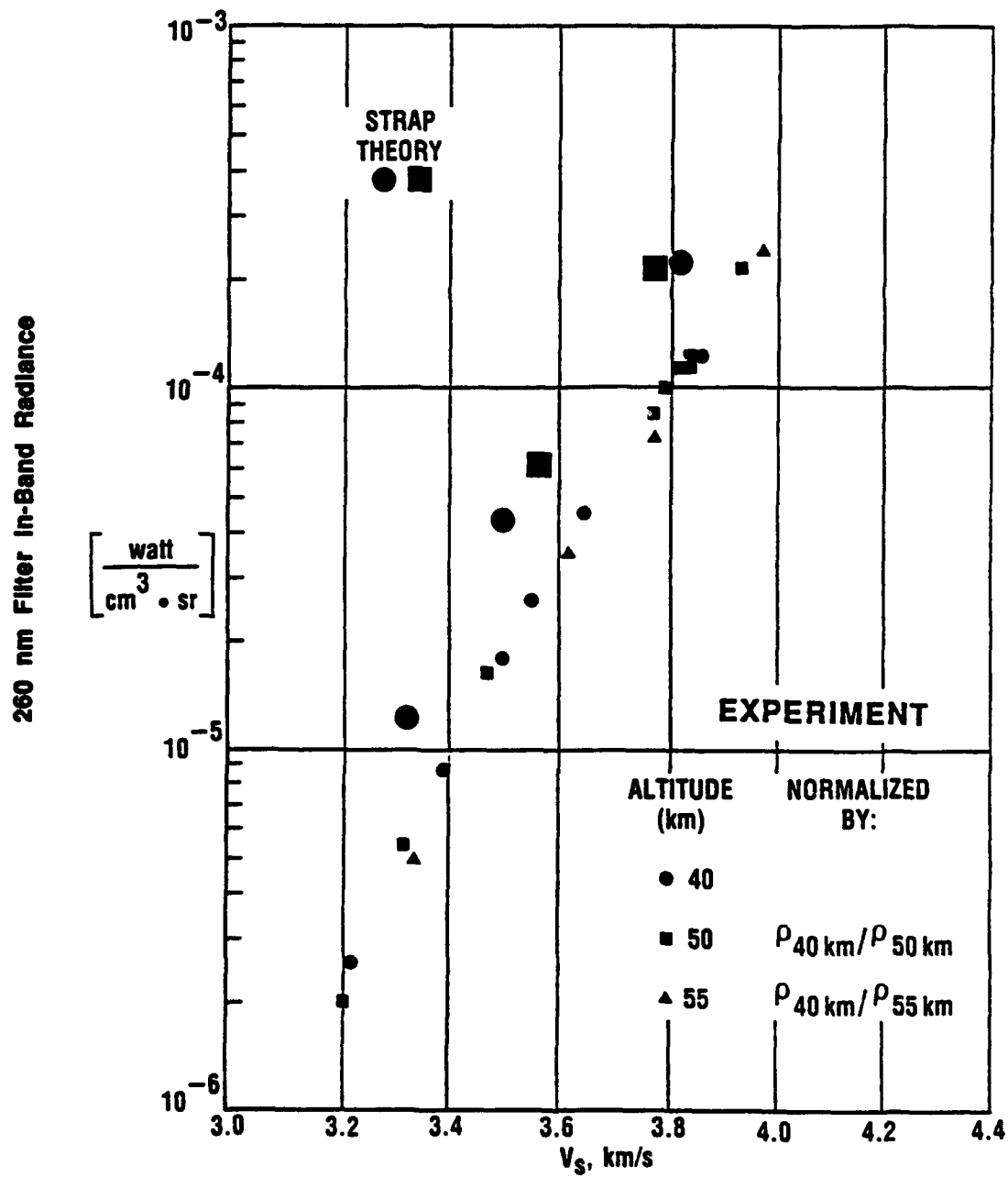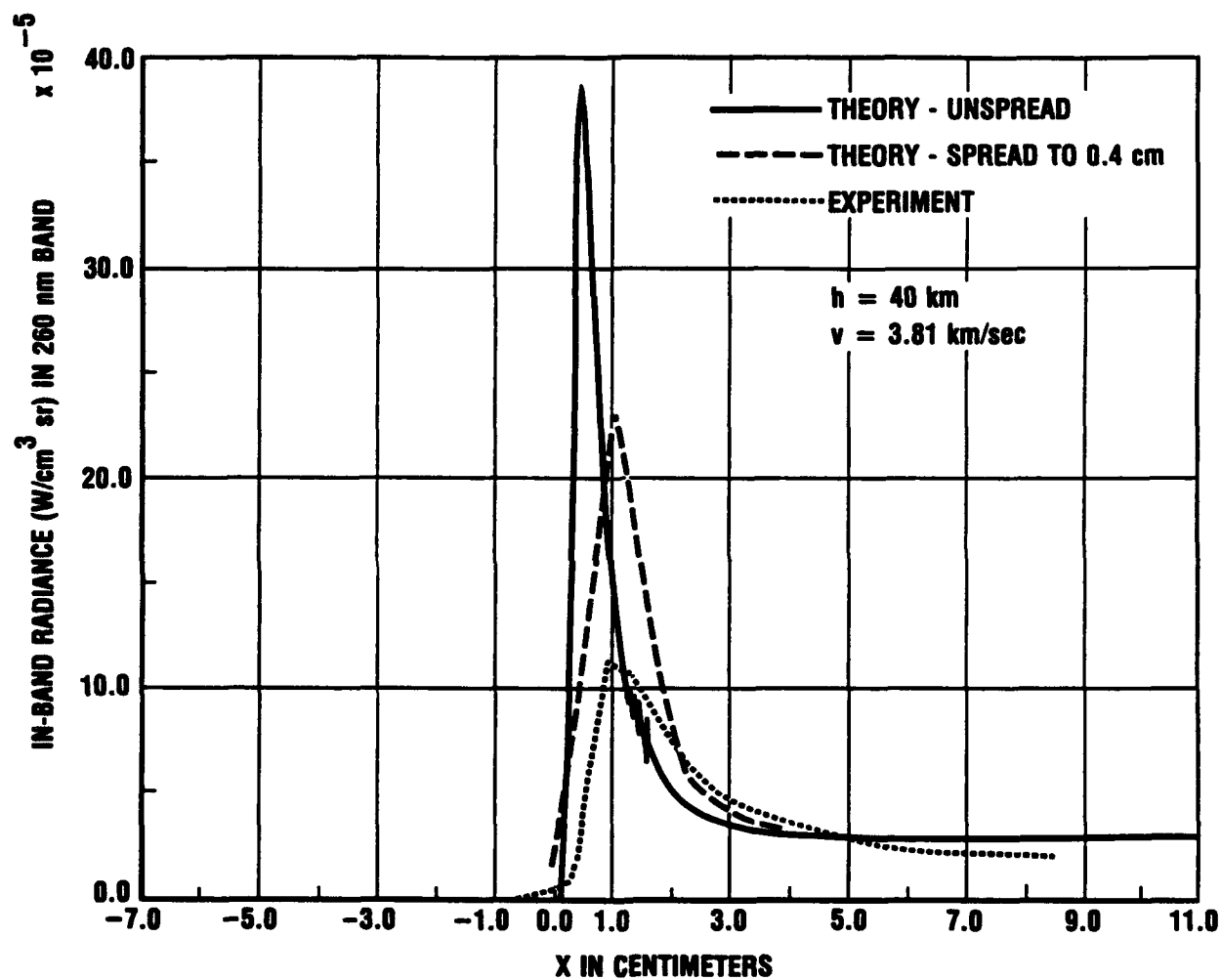
Figure II-9. Comparison of Shock Tube Experimental (CALSPAN) and Model (IDA/Ames) Results. V_s is the shock velocity, and ρ is the density.

2-15-89-4

II-38

Figure II-10. Finite Field-of-View Factor and Transformation From Laboratory Reference Frame

In Appendix B, entitled, "Comparison of Spectra and Assignment of Radiating Species in Shock Tube Measurements," we discuss calculations and analyses that were undertaken to deconvolve STRAP/NEQAIR-derived spectra quantitatively. The analyses show qualitative agreement obtained between theory and experiment with additional measurements necessary to provided quantitative verification.

3. Conclusions

The abovementioned calculations show good agreement (factor of 2-3) between theory and experiment over a range of altitudes and velocities. While the level of agreement obtained does not provide specific in-depth validation of the computational method, it suggests that important physical approximations used, such as an equilibrated vibrational and electron temperature, are correct.

The level of spectral agreement between the two calculations in the equilibrium regime is acceptable. More radiometric data or absolute OMA spectral data is required to have confidence in the relative spectral contributions in the peak radiating portion of the shock region.

REFERENCES, CHAPTER II.D

II.D-1. W.H. Wurster, "Interim Results from the CUBRC Program on Non-Equilibrium
Radiation from Shock-Heated Air," CALSPAN/CUBRC Memorandum for the
record, 23 November 1988.

II.D-2. W.H. Wurster and M.J. Williams, "Memorandum Addendum," CALSPAN/
CUBRC Memorandum for the record, 23 December 1988.

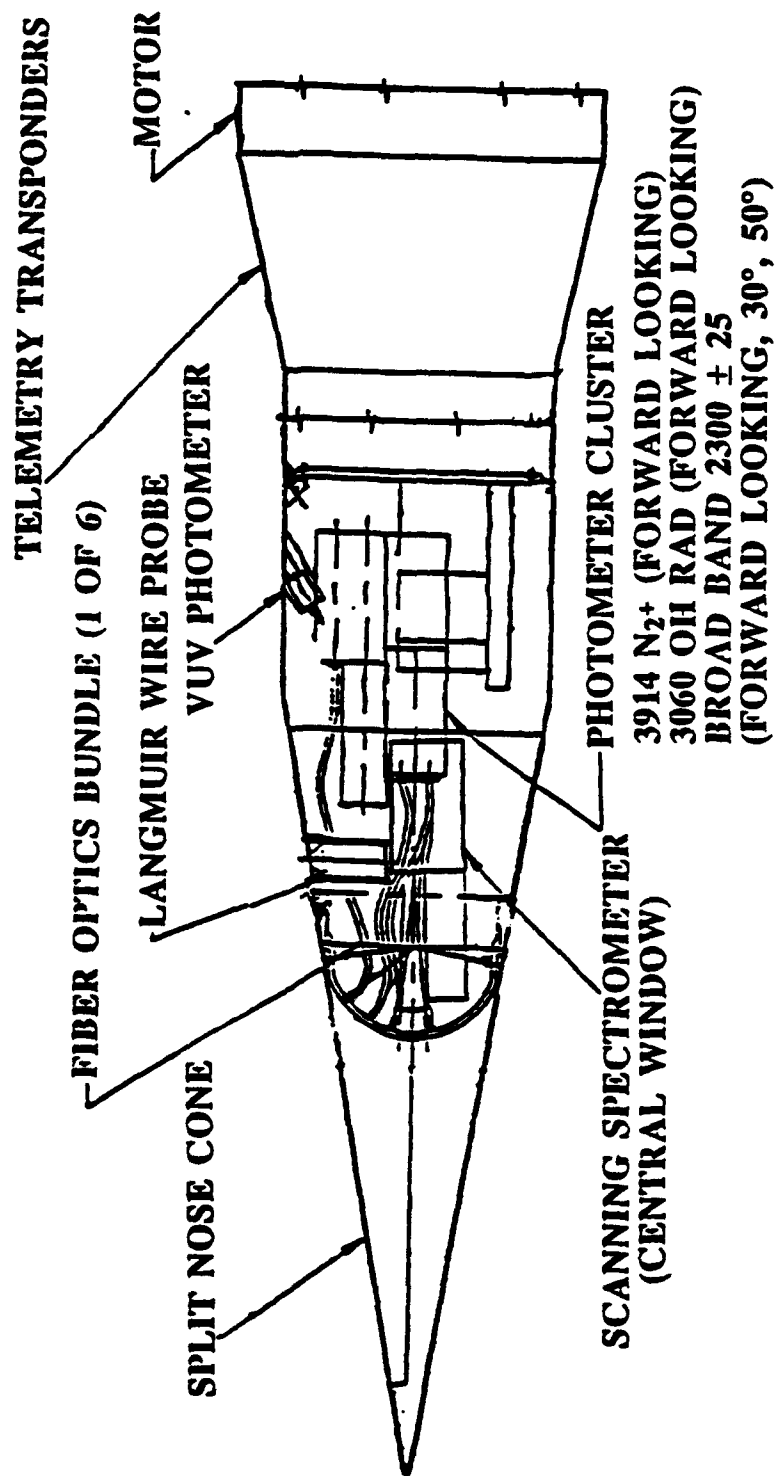## E. COMPUTATIONAL RESULTS IN SUPPORT OF BOW SHOCK FLIGHT EXPERIMENT

1. Introduction

The earlier sections in this chapter have dealt with our investigations into the critical sensitivities of the models with regard to chemical and excitation/de-excitation mechanisms. The previous section then discussed the comparison of a shock-tube version of the models (STRAP) with recent shock-tube data. In this section we use the baseline versions of the models to predict observables for the upcoming rocket-borne flight experiment mentioned in Section I.A. The results of these calculations are presented here.

The rocket-borne, bowshock UV experiment (BSUV) will be carried aboard a Terrier-Malemute launch vehicle. Figure II-11 shows a diagram of the payload layout, taken from Ref. II.E-1. The vehicle is configured to achieve a nominal velocity of 3.5 km/sec, at an altitude of 40 km, at which time the rocket is expected to burn out. At this point, a protective nose cone shroud will be ejected, exposing a four-inch radius hemispherical nose cone, containing several conformal quartz optical windows. Radiation measurements will then be taken over the altitude range of 40-80 km, on both ascent and descent. These measurements can then be compared to the theoretical CFD and radiation code predictions in this flight regime. This comparison will lead to code validation, or quantification of the discrepancies between theory and experiment.

The primary BSUV payload instrument is a rapid scanning UV spectrometer. The spectrometer can make four scans a second, covering the wavelength range from 2000-4000Å, with 10Å spectral resolution. The spectrometer views the bowshock through a window on the longitudinal axis of the payload (defined as 0 deg, refer to Fig. II-11). In addition to the spectrometer, eight quartz fiber optic coupled photometers are distributed over the dome (0 deg, 30 deg, 50 deg) to measure the spatial variation of selected spectral features. An electron density microprobe, atomic oxygen monitor, and several resistance thermometers are also included in the payload package.

In subsection 2. we discuss results, generated by SPRAP/NEQAIR, for a four-inch nose radius, a speed of 3.5 km/sec, and an altitude of 40 km. The optical filter functions for the future flight experiment, as supplied to us by Dr. Pat Espy, Utah State University, were used to calculate expected in-band radiance values.

TELEMETRY TRANSPONDERS

MOTOR

FIBER OPTICS BUNDLE (1 OF 6)

LANGMUIR WIRE PROBE
VUV PHOTOMETER

PHOTOMETER CLUSTER
3914 N₂⁺ (FORWARD LOOKING)
3060 OH RAD (FORWARD LOOKING)
BROAD BAND 2300 ± 25
(FORWARD LOOKING, 30°, 50°)

SPLIT NOSE CONE

SCANNING SPECTROMETER
(CENTRAL WINDOW)

Figure II-11. BSUV Payload Layout

In subsection 3., the 2-D code/NEQAIR combination was used to derive radiances over the NO gamma band spectral region, at the stagnation point, as a function of speed and altitude. These calculations were made for a three-inch nose radius vehicle because of the convenience of using the three-inch spatial grid originally provided to us by the author of the CFD code. Our earlier work with the SPRAP/NEQAIR model indicated that there is approximately a liner scaling of radiation with nose radius. Therefore, we suspect that the results for a four-inch nose radius vehicle would only change the three-inch numbers by a factor of 4/3. Subsequent to this paper, new calculations were undertaken for a four-inch nose radius. To bound the theoretical uncertainty in the radiation modeling, the 2-D flowfield code was also run in an equilibrium mode. In that form, all aspects of the model remained identical, except the combined heavy particle-rotational temperature, T, was set equal to the combined vibrational-electronic excitation temperature, T_v. Comparisons of the radiance values for non-equilibrium versus equilibrium modeling will be shown below.

2. SPRAP Runs in Support of Bow Shock Flight Experiment

Figure II-12 presents SPRAP/NEQAIR spectra calculated for the conditions given in the figure caption. The spectra were calculated using 0.6Å resolution and represent radiation reaching the windows on the nose cone surface, i.e., the spectral contributions have been integrated over the stagnation streamline from the shock to the nose. The spectra have been convoluted with the filter functions in Fig. II-12(b)-(d). The Gaussian half widths and center wavelengths of the filters are given on the respective curves. When the spectra are summed over the appropriate filter weighting functions, the in-band radiances given in Table II-7 are obtained. The values given in Table II-7 are larger than the minimum signals measurable by the photometers.

The 3090Å filter, designed to measure emission contributions from the OH radical, has been included in the BSUV flight experiment. However, OH reactive chemistry and excitation/deexcitation mechanisms are not currently modeled in the CFD and radiation codes used here. Thus, we were unable to obtain an in-band radiance prediction for that filter.
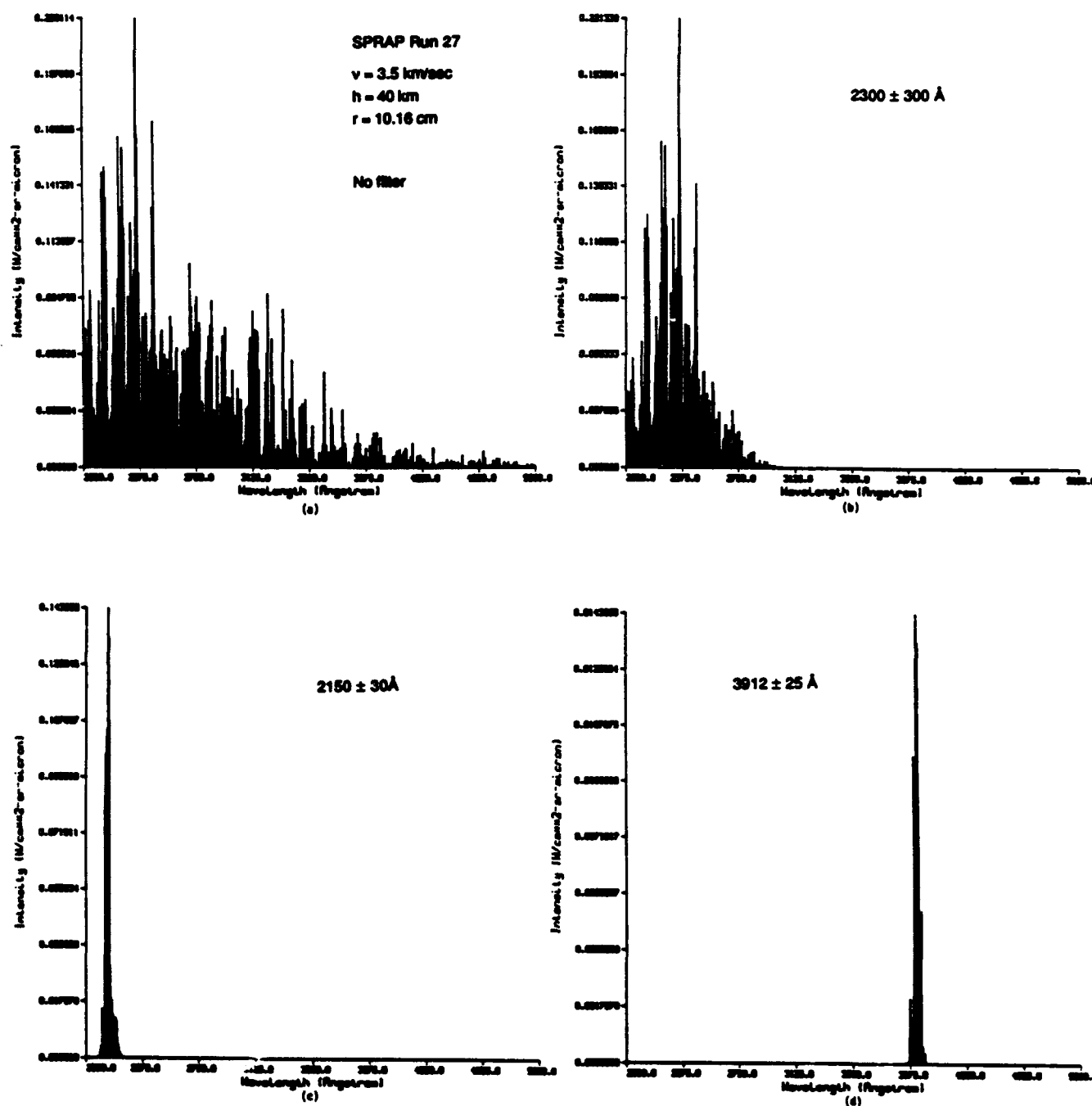
SPRAP Run 27

v = 3.5 km/sec
h = 40 km
r = 10.16 cm

No filter

2300 ± 300 Å

2150 ± 30Å

3912 ± 25 Å

**Figure II-12. Spectral Intensities for a 4-in. Nose Radius at
3.5 km/sec, 40 km Altitude**

Table II-7. Summary of SPRAP-Bow Shock Experiment Radiometer Filter Calculations[a]

Band (Å)	In-band Radiance (W/cm²sr)
2000 - 5000[b]	1.6×10^{-3}
2150 ± 30	1.05×10^{-4}
2300 ± 300	8.27×10^{-4}
3090 ± 40[c]	N/A
3912 ± 25	9.65×10^{-6}

[a] v = 3.5 km/sec, h = 40 km, r = 10.16 cm (nose radius).

[b] Assumes a rectangle filter with 100 percent transmission.

[c] No OH chemistry in codes.

3. Three-Inch Two-Dimensional Flowfield Results

Figure II-13[6] shows an expanded view of the 2-D computational grid in the vicinity of the nose for the three-inch nose radius case examined. The grid used actually goes aft (+ X direction) on to the cone of a spherical-cone shaped body, although it is not shown in the figure. The figure shows that there is a concentration of grid points nearer the body and closer to the stagnation stream line, where the chemical and relaxation processes are changing more rapidly. The shock itself lies roughly midway between the outer curve and the wall (compare Fig. II-13 and II-14).

The first set of results shown are for 3.5 km/sec, 40 km altitude, which corresponds to the earliest point at which it is anticipated that data will be obtained in the flight experiment's trajectory. Figures II-14 and II-15 show contour plots of the heavy particle temperature, T, and the combined vibrational-electronic temperature, T_v, respectively. The 2-D aspect of these calculations is summarized by these figures. For both temperatures, the peak values occur long the stagnation stream line; however, the vibrational temperatures are generally lower than the heavy particle translational temperature. Downstream, the heavy particle temperature values have almost dropped by a factor of two. The vibrational temperatures, however, are not observed to drop as rapidly.

Figures II-16 and II-17 show the amounts of NO and O produced in terms of percent mass fraction. These are the two largest concentrations of chemically produced species in the flow. Density maps of other chemical species can also be generated from the flowfield data.

---

[6] The figures shown were made using the software package "PLOT3D," Pieter G. Buning, Ames Research Center.
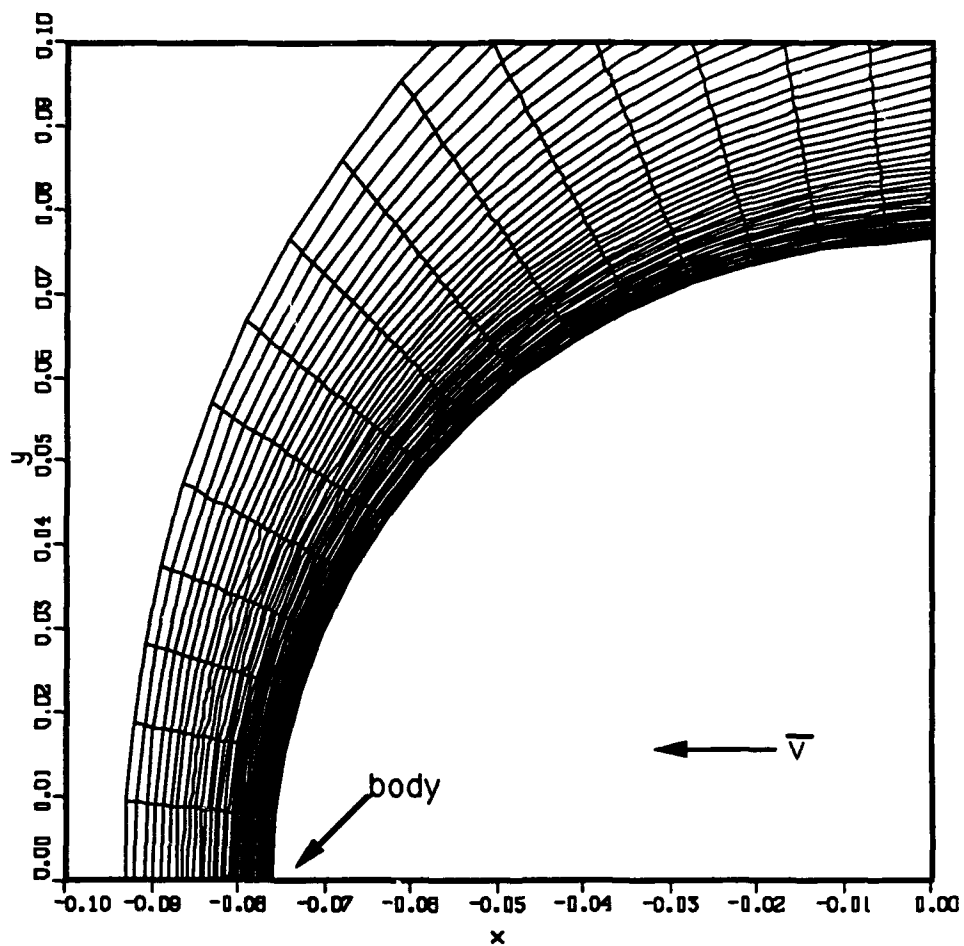
Figure II-13. Three-inch Nose Radius Grid. Nose Region Expanded View. The x and y axes are in meters. The vehicle velocity vector would be along the - x direction.

II-47

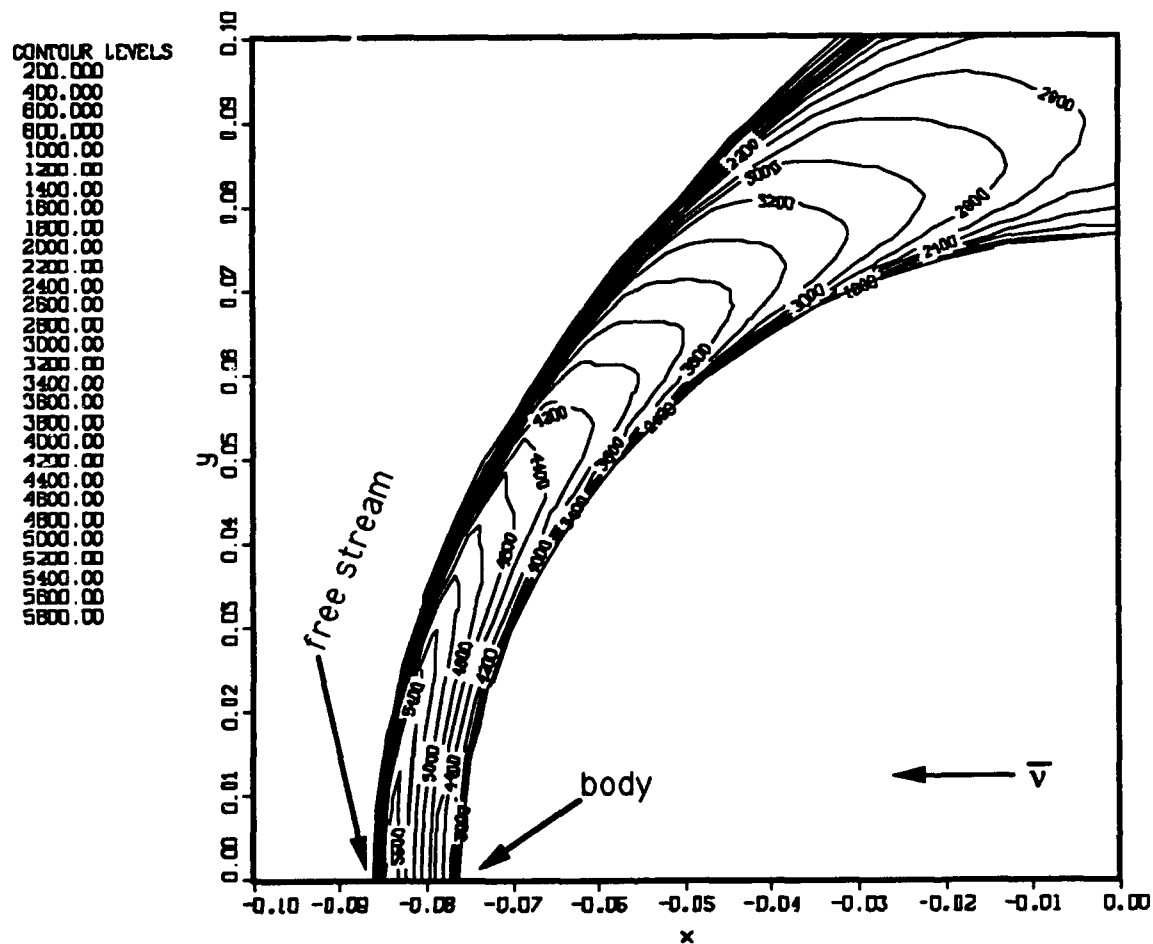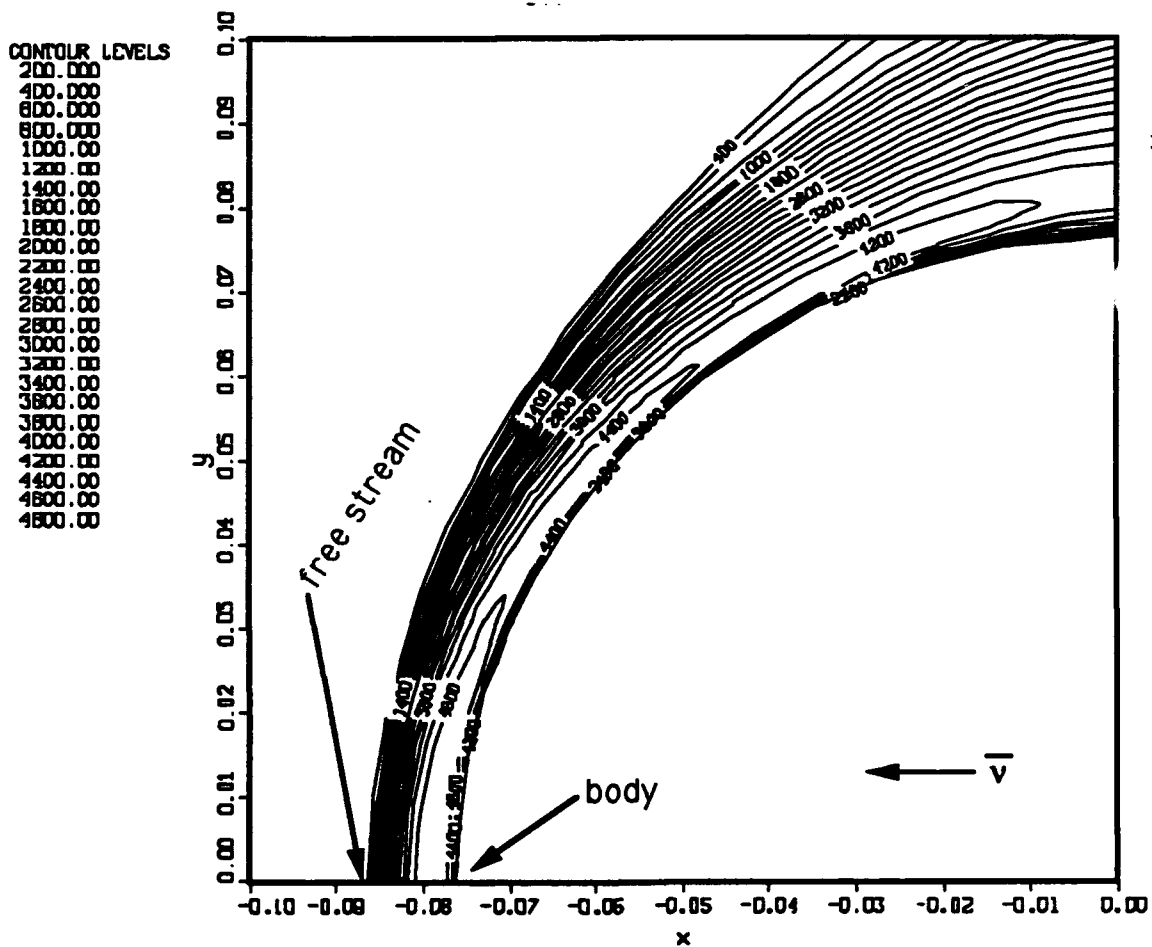**Figure II-14. Heavy Particle Temperature, T, Contours for the Multi-Temperature Model at 3.5 km/sec, 40 km Altitude. The x and y axes are in meters. The vehicle velocity vector would be along the - x direction.**
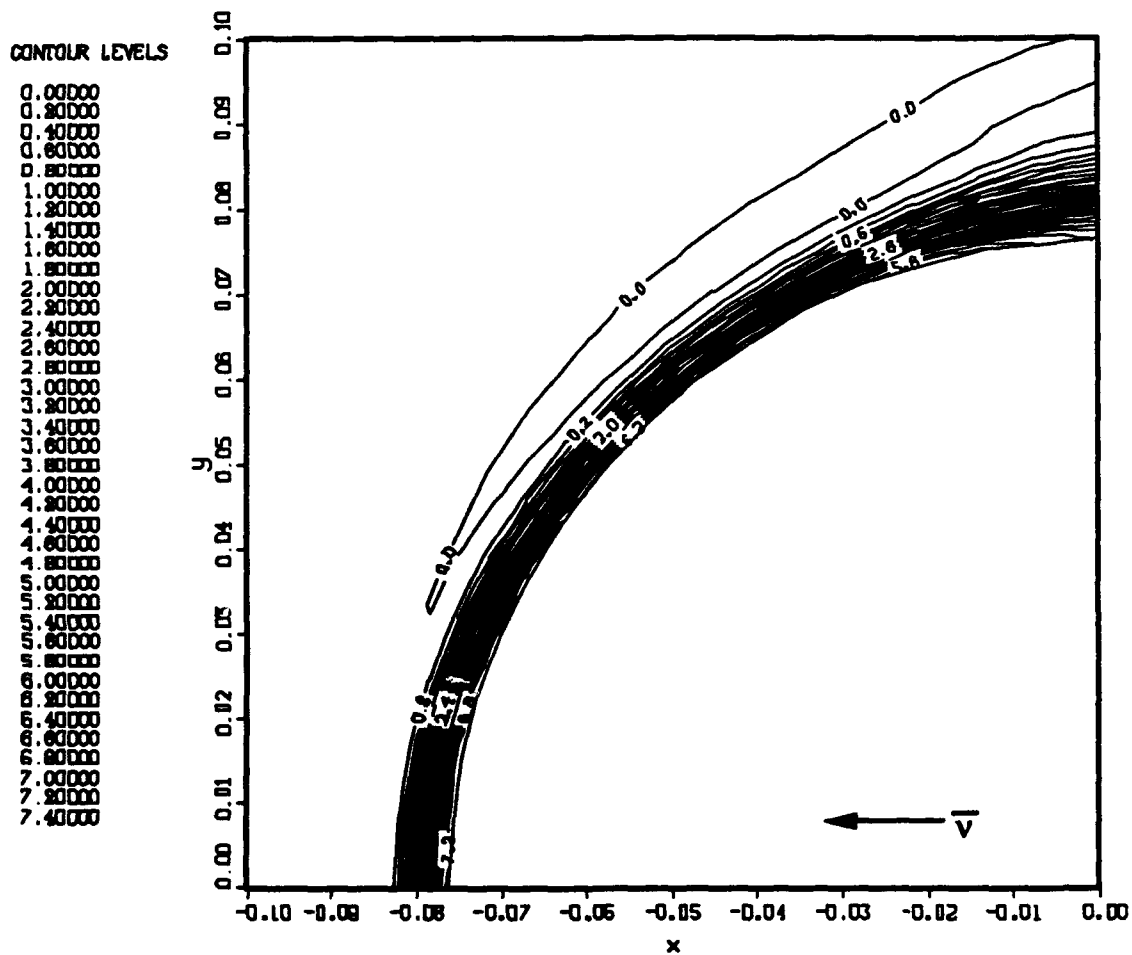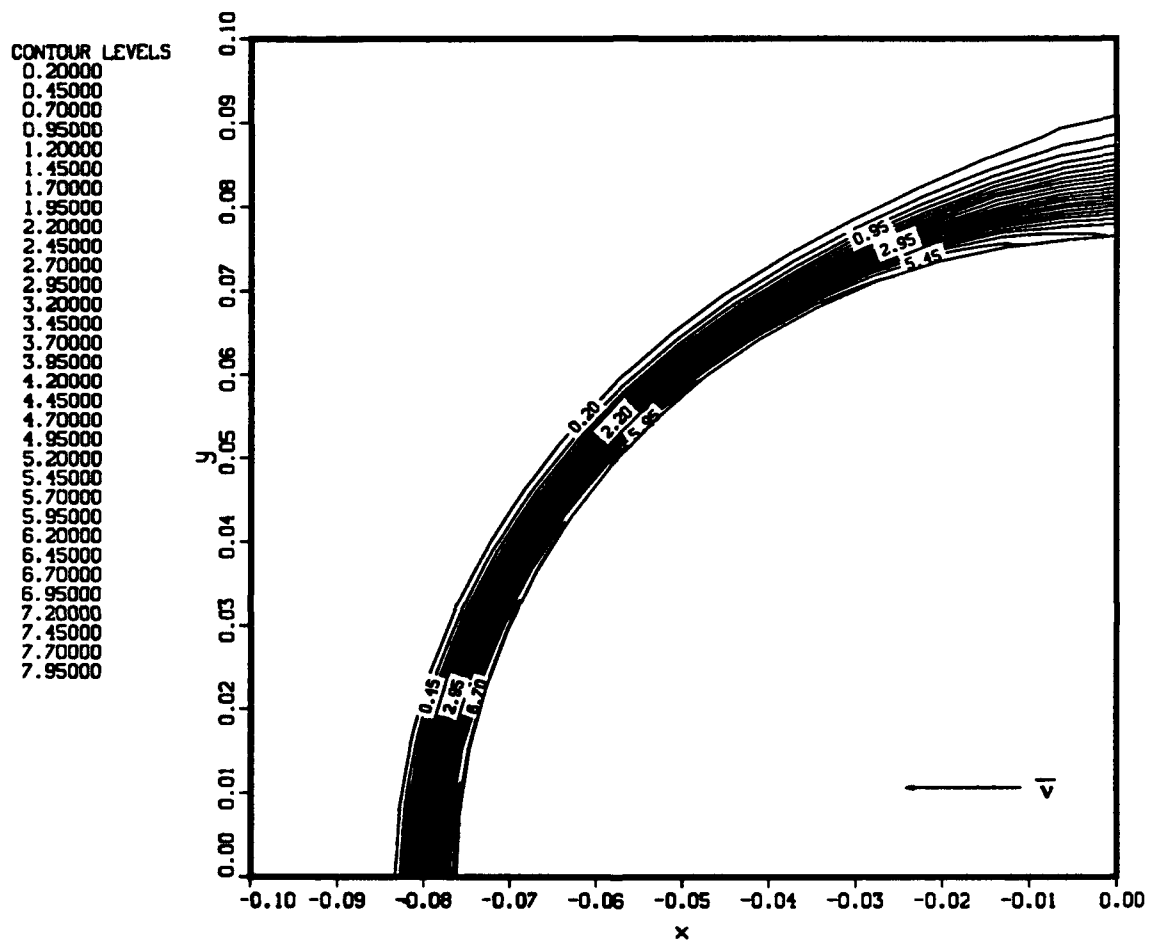
II-48

Figure II-15. Vibrational Temperature, T_v, Contours for the Multi-Temperature Model at 3.5 km/sec, 40 km Altitude. The x and y axes are in meters. The vehicle velocity vector would be along the - x direction.

Figure II-16. NO Percent Mass Fraction Contours for the Multi-Temperature Model at 3.5 km/sec 40 km Altitude. The x and y axes are in meters. The vehicle velocity vector would be along the - x direction.

II-50

Figure II-17. Present Mass Fraction Atomic oxygen Contours for the Multi-Temperature Model at 3.5 km/sec 40 km Altitude. The x and y axes are in meters. The vehicle velocity vector would be along the - x direction.

The spatial distribution of radiation falling in a 2250-2750Å band is shown in Fig. II-18. Contour values of 1.5-3.5 indicate the brightest spatial regions of the flow. The radiation is seen to drop off as one moves off the stagnation stream line (x axis). Values of 8 and 9 in Fig. II-18 basically correspond to the free steam.
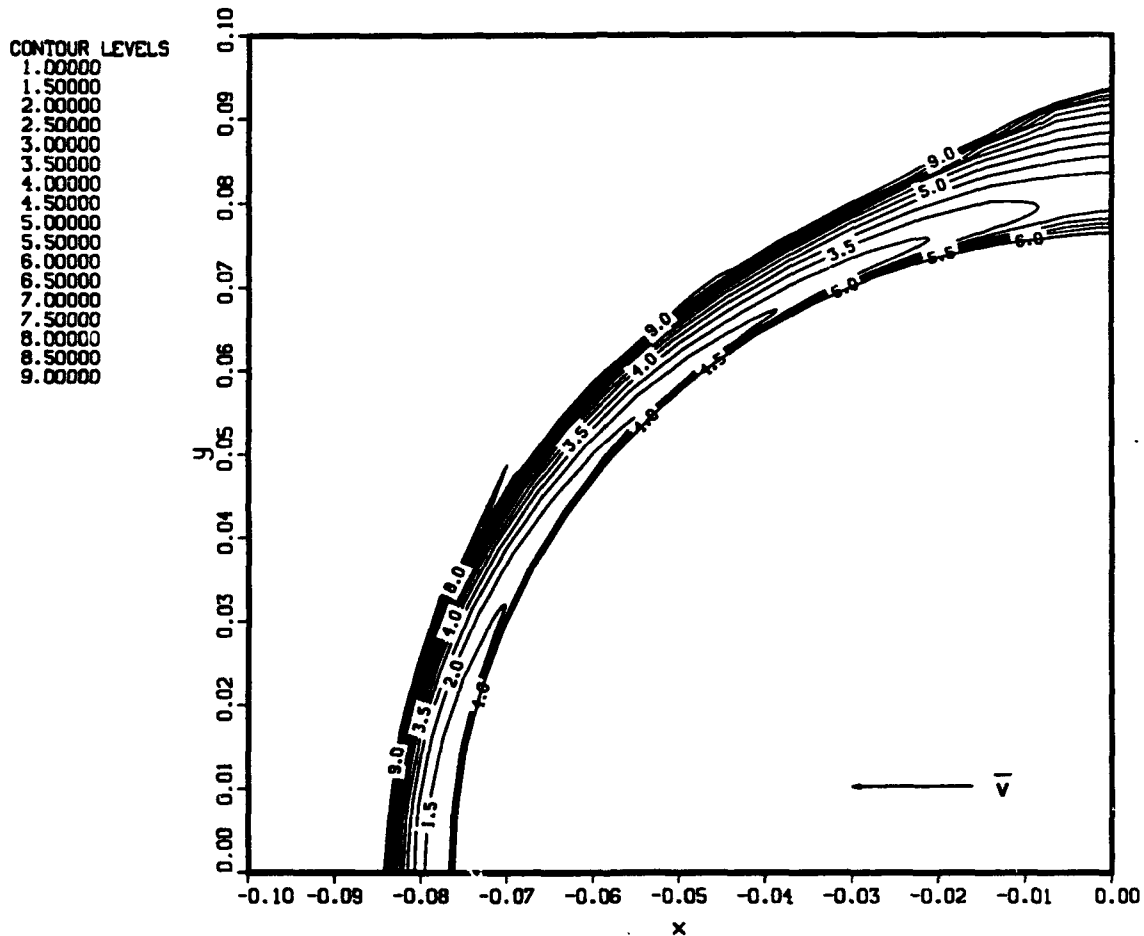

Figure II-18. Radiance (W/cm³μsr) produced for a three-inch nose radius, 3.5 km/sec, 40 km altitude calculation. Values given are the *negative logarithm* of the radiance in a 100% transmittance, square wave filter covering 2250-2750Å. X and Y axes are in meters.

II-52

As was mentioned in earlier sections, the nonequilibrium modeling is an important aspect of the codes used here. The nonequilibrium (multi-temperature) modeling prediction of the radiation will produce a lower value than that of the equilibrium ($T = T_v$) model. This is because $T_v \leq T$ in the multi-temperature model. Thus, the multi-temperature model should provide a lower limit to the amount of radiation within the framework of the present case, vis a vis chemistry and transport. Uncertainties in vibrational-translational energy transfer mechanisms are eliminated in a one-temperature model because the two temperatures are equal throughout the flow, although such a model is not physically correct.

A detailed comparison was made for a 3.7 km/sec, 60 km altitude case where, as shown in Fig. II-19, there is a radiance spread of about three orders of magnitude for the multiple versus single-temperature model. Two factors account for the lower radiance value obtained with the multi-temperature model. As expected, that model gives lower values for T than the single-temperature model. Also, since the concentration of radiating species is dependent upon chemical rates that use the lower value of $(T \cdot T_v)^{1/2}$ instead of T, almost an order of magnitude less NO is produced than for the single-temperature model. Evidence of less reactive chemistry is also observed for atomic oxygen. Figure II-19 shows a summary of irradiance levels, as a function of velocity, for 40, 50 and 60 km, for the multiple and single-temperature models at the stagnation point. Comparison of the multiple versus single-temperature results shows that at higher velocities and lower altitudes the two model results tend to merge. In both limits there are a greater number of collisions in the flow, which lead to equilibrium. By 50 km and 3.5 km/sec, however, there is about an order of magnitude discrepancy, with the single-temperature model over-predicting the amount of radiation produced. At 60 km the single-temperature model would overestimate the radiance by many orders of magnitude. In fact, the 60 km multi-temperature result is also probably optimistically high due to combination of the electron-vibrational temperature assumed here.

The values in Fig. II-19 will be used to help set instrument sensitivity levels for the BSUV experimental flight, and it is hoped that the experimental measurements will provide insight as to which temperature model best agrees with the real physical situation. The horizontal lines in the figure indicate the minimum signal measurable by the spectrometer and photometers, as presently configured for the BSUV flight experiment, using a (S/N) ratio of ten. For a 3.5 km/sec vehicle, the radiometers are expected to provide adequate

sensitivity at 60 km altitude. Multiple spectrometer scans may have to be co-added to provide enough signal by 60 km altitude.
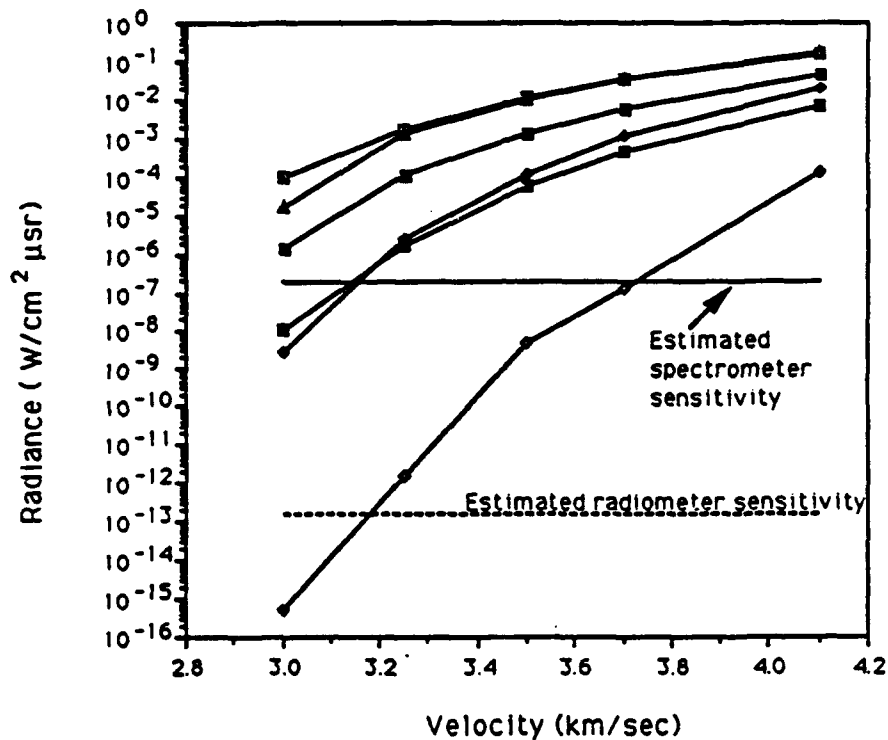
Figure II-19. Summary of Three-Inch Nose Radius Calculation. Comparison between thermal equilibrium and non-equilibrium modeling is shown as a function of speed and altitude. Radiances shown are at the stagnation point on the vehicle nose.

─▲─ 40km, Multi- T	─□─ 40km,Single-T	─◆─ 50km,Multi-T
─■─ 50km,Single-T	─◆─ 60km,Multi-T	─■─ 60km,Single-T

Thermal equilibrium is Single-T, and Non-equilibrium is Multi-T. Radiances are calculated from 2250Å to 2750Å assuming a rectangular filter with 100% transmittance.

REFERENCES, CHAPTER II.E

II.E-1. R. Kolebar, *Bowshock UV (BSUV) Experiment Program Introduction Document.* Space Data Corporation Technical Memorandum TM-4702, February 1990.

III. SUMMARY AND REMAINING ISSUES

The calculations and analyses discussed in this report have gone a long way toward providing the quantitative information necessary to validate the concept of bow shock radiation as a viable signature. Although far from complete, our understanding of the relevant modeling requirements, as well as necessary confirming experiments, has improved considerably in a period of about one year. This has been achieved primarily through our ability to exercise the relevant computational tools and interact with scientists at the various institutions mentioned throughout the paper. In this chapter we summarize what were the key results, and discuss the remaining needs.

In Section II.A we discussed our "shakedown" of the SPRAP/STRAP and 2-D CFD tools for use in the boost phase velocity-altitude parameter space (i.e., velocities of 3-4 km/sec and altitudes of 40-80 km). The result was the ability to identify whether these codes could be used in this boost phase regime where the temperatures, predominant species, excitation mechanisms, and Knudsen numbers were different. It was found (Appendix A) that the SPRAP code can only be used reliably down to speeds of about 3.5 km/sec at 40 km type free stream conditions because of difficulties with modeling of the boundary layer in that code. The STRAP code, however, would not be affected by this problem and gave a factor of two agreement with new shock tube results obtained by CALSPAN/CUBRC. Because of its improved boundary layer modelling, the 2-D code therefore became our primary bow shock flowfield tool. Figure II-19 showed a summary of these results for a three-inch nose radius. Calculations assuming thermal equilibrium, with a modified version of the 2-D code, showed that at slower speeds and higher altitudes the flow is considerably out of thermal equilibrium (Section II.E). The kinetic analysis (Section II.B) showed that the differences in rate data observable in the literature, as well as between SPRAP and the 2-D codes, is not likely to affect the final radiation values seriously. It showed that the flow is out of chemical equilibrium as well. The analyses of the NEQAIR module (Section II.C) showed that at 40 km and 3.5 km/sec, and under conditions in the flow where the maximum radiation is produced, the radiation magnitude appears to be close to that obtained in the Boltzmann limit. It was our assessment that the electron and neutral particle excitation/de-excitation mechanistic modeling appeared to be

adequate. The use of the quasi-steady state approximation, in conjunction with the same level of modeling as presently exists in the code, was not investigated for weaker shock conditions than the boost phase conditions considered here. Under those conditions, the decrease in the number of collisions introduces much greater uncertainty in the reliability of NEQAIR, and needs further investigation.

The calculations of Sections II.D and E show that theory and instrumental design are well grounded to permit a high probability of mission success for the BSUV rocket experiment. Additional calculations are in progress with the 2-D/NEQAIR code to accurately calculate the signal levels for the proposed optical instrument layout, in a four-inch nose radius vehicle. Although greater than five orders of magnitude instrumental dynamic range will be available, the calculations done here are necessary to set a reasonable threshold limit for the instruments.

The remaining issues and work are outlined below. Regarding the results presented in Chapter II, the adequacy of the assumption of an equilibrated electronic and vibrational temperature needs to be resolved, particularly for weaker shock conditions (i.e., 3.7 km/sec, 60 km altitude conditions). The electron temperature model in the 2-D code should be reevaluated to include non-resonance background contributions. Recently, low energy electron temperature measurements have been obtained for N_2 at energies closer to 0.5 eV. These measurements should be reviewed. The formalism presently utilized in NEQAIR needs to be generalized to account for inter-species electronic excitation processes, and may need to be recast in a more generalized form than the quasi-steady state. The analyses of the shock tube data given in section II.D points out the need for absolute intensity spectrometer data to resolve quantitatively the relative importance of the NO gamma, and the O_2 Schumann-Runge bands. The 2-D code calculations also need to be repeated for a four-inch nose radius vehicle, with a sufficiently detailed grid that the optical instrument responses can be adequately modeled.

The coordination, and possible use, of present SDIO UV satellite assets for bow shock radiation phenomena will provide assessment of the actual versus theoretical capabilities of present detectors in a space environment. These assets should also be used to view bow shock phenomenon at faster speeds, a region where there is less uncertainty in the signature modeling.

Finally, the system utility of bow shock radiation in terms of acquisition and tracking requirements and the coordination of other possible sources of UV signatures due to solar scattering and plume radiation will be addressed in the future.

APPENDIX A

CODE VALIDATION AND INITIAL USAGE

APPENDIX A
CODE VALIDATION AND INITIAL USAGE

This Appendix discusses our earliest use and validation of the 1-D code of Park, which also provided our first radiance estimates. Comparison of the 1 and 2-D codes is also given.

In an earlier paper (Ref. A-1), we discussed Park's validation of his 1-D model with AVCO/Everett shock tube data and the PAET reentry probe experiment. Figure A-1 shows a plot of the data (curves labeled "measured total" and "measured backgrounds") and Park's calculated result using the SPRAP/NEQAIR code (see triangles). From Table II-5 of Ref. A-2, the power at the detector, in the 3910Å filter band, after background subtraction, was found to be 1.87×10^{-7} W for an altitude of 50 km (562.6 seconds from launch). The velocity at this altitude was 6 km/sec. The corresponding radiometer field of view (FOV) of 0.077 sr, filter half width of 31.2Å, and peak transmission of 0.215 implies an experimental source radiance, I, of 0.453 $W/cm^2\mu sr$. The atmospheric air encountered by the PAET experimental probe contains carbon dioxide, which contributes to CN production behind the shock wave. When convoluted with the transmission curve of the filter, the CN radiation was believed to contribute 60 percent of the signal in the filter band width, with N_2^+ radiation contributing 40 percent (Ref. A-3). Since NEQAIR does not model CN radiation (but does model N_2^+) the experimental source radiance value given above must be reduced by a factor of 0.4 for proper comparison to the theoretical (SPRAP) prediction. This gives an experimental value of N_2^+ radiance of 0.181 $W/cm^2\mu sr$. Park calculated a radiative surface flux value of 3.2×10^{-3} $W/cm^2\mu sr$, into 2π steradians using SPRAP. This implies a theoretical N_2^+ radiance of 0.163 $W/cm^2\mu sr$, or an agreement of theory and *experiment* of 11 percent. Our calculation of this variable for the same conditions gave and N_2^+ source radiance of 0.159 $W/cm^2\mu sr$, which was considered to be good agreement, since we approximated the filter bandwidth as a square wave, versus the true, approximately Gaussian bandshape used by Park in his calculation.
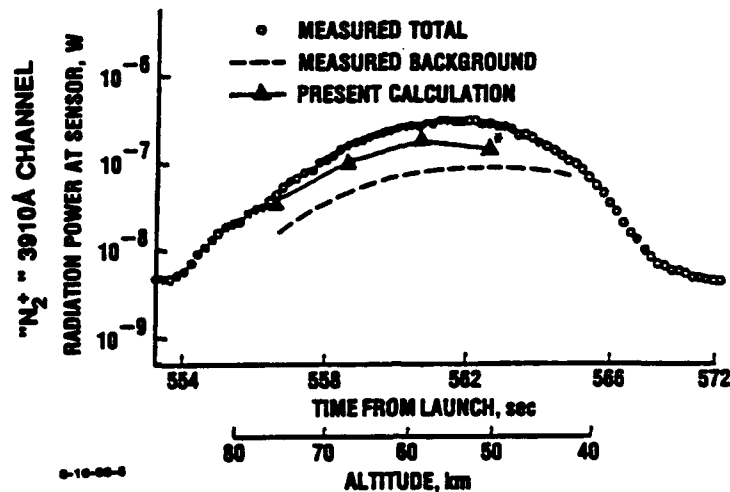
Note: Verified at IDA using C. Park's Two-Temperature CFD Code.

Figure A-1. Comparison Between Calculated and Measured Radiation Intensities at 391 nm in PAET Experiment (Ref. A-3).

The above SPRAP calculation was done to ensure that we were properly interpreting the code results. Next, a series of SPRAP runs, identified in Table A-1, were undertaken. The trajectory conditions for a three-inch nose radius sphere cone were obtained in part from Ref. A-1. The column designated τ_e is the time required to reach equilibrium and was obtained for this table by extrapolating Fig. 4 of Ref. A-3. It is the time that it takes the flow to equilibrate or reach a single temperature and for species concentrations to remain constant in the absence of a cool wall. The table shows that we experienced difficulty in running the code under conditions where the distance necessary for the flow to equilibrate, x_e (cm), was much larger than the shock stand-off distance. As can be seen from the table, the problem gets worse as the velocity is reduced and the altitude increases. Figures A-2a, b, c and A-3 a, b, c show cases that produced, and failed to produce, a physical solution, respectively. The series of plots show temperatures, NO, mole fraction and radiated power in a 500Å band centered at 2500Å, as a function of distance along the stagnation stream line. Very notable is the equilibration of the two

A-4

temperatures in Fig. A-2a but lack of equilibration in Fig. A-3a. As will be explained later, this difference in relaxation behavior is correct. In fact, a "forced" temperature relaxation or a "single temperature" solution will overestimate the amount of radiation in the flow. The flow predictions in Figs. A-3b and c, however, are in error, and show evidence of the calculation being terminated prematurely due to lack of adequate modeling in the relatively large boundary layer region (note that the NO concentration is held constant in the boundary layer). The source irradiance of 2.5×10^{-13} W/cm^{2}μsr can be seen to be too low since it is the linear spatial integration of the curve in Fig. A-3c.

Table A-1. Computational Results with SPRAP[a]

Worked	V (cm/sec)	ρ_∞ (gm/cm^3)	Standoff h (km)	Distance (cm)	(W/cm^{2}μsr)	τ_e (μsec)[b]	x_e (cm)[c]
No	3×10^5	1.027×10^{-6}	50	0.3	2.528×10^{-13}	95.3	4.77
No	4×10^5	3.992×10^{-8}	75	0.4	3.043×10^{-9}	1270	84.7
Yes	4.1×10^5	3.996×10^{-6}	40	0.7	0.3896	10.2	0.697
No	6×10^5	3.992×10^{-8}	75	0.4	1.310×10^{-3}	212	21.2
Yes	6.3×10^5	3.996×10^{-6}	40	0.5	1.473	1.41	0.148
Yes	7.3×10^5	8.324×10^{-7}	51.7	0.5	0.7028	2.67	0.325
No	9×10^5	8.283×10^{-8}	70	0.4	8.384×10^{-3}	7.76	1.16
Yes	9×10^5	3.996×10^{-6}	40	0.45	1.472	0.141	0.0212
Yes	10.5×10^5	1.027×10^{-6}	50	0.4	0.3616	0.114	0.110
Yes	12×10^5	3.097×10^{-7}	60	0.5	0.1559	0.0923	0.0185

[a] r_n = 7.62 cm (nose radius used for all runs).

[b] time to reach chemical equilibrium (see text).

[c] x_e, distance needed to reach chemical equilibrium.

$$x_e \cong \left(\frac{V}{6}\right)\tau_e , \; V = \text{velocity} .$$

The inadequate boundary layer modeling in the 1-D code over portions of our altitude-velocity profile of interest was one of the factors that led us into using the 2-D code. The first run that was made with the 2-D code used input conditions equivalent to the third 1-D code run in Table A-1, i.e., 4.1 km/sec velocity, 40 km altitude, and a three-inch nose radius. Figures A-4 and A-5 show a comparison of those results along the stagnation

A-5
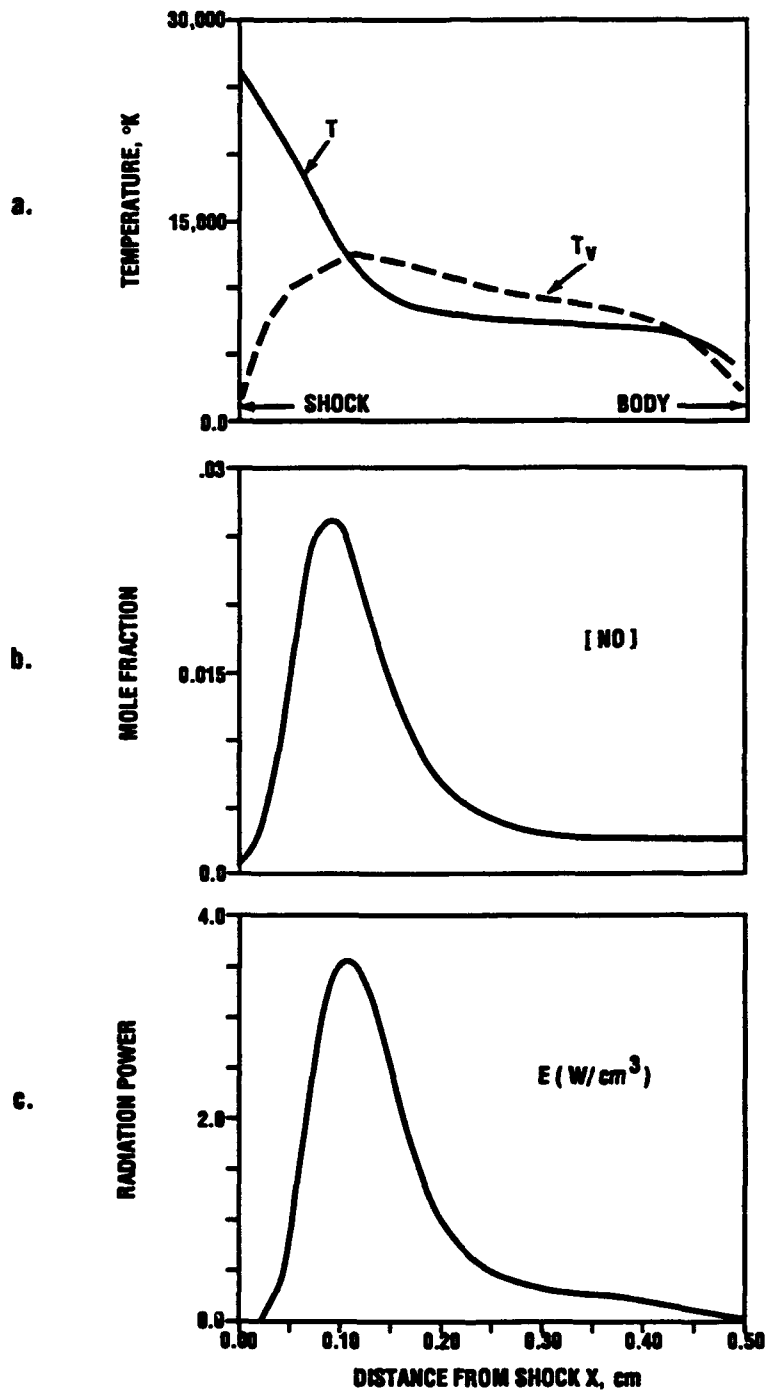
Figure A-2. Flowfield Conditions at 6.3 km/s, h = 40 km, r_n = 7.62 cm.

1-29-91-2

A-6
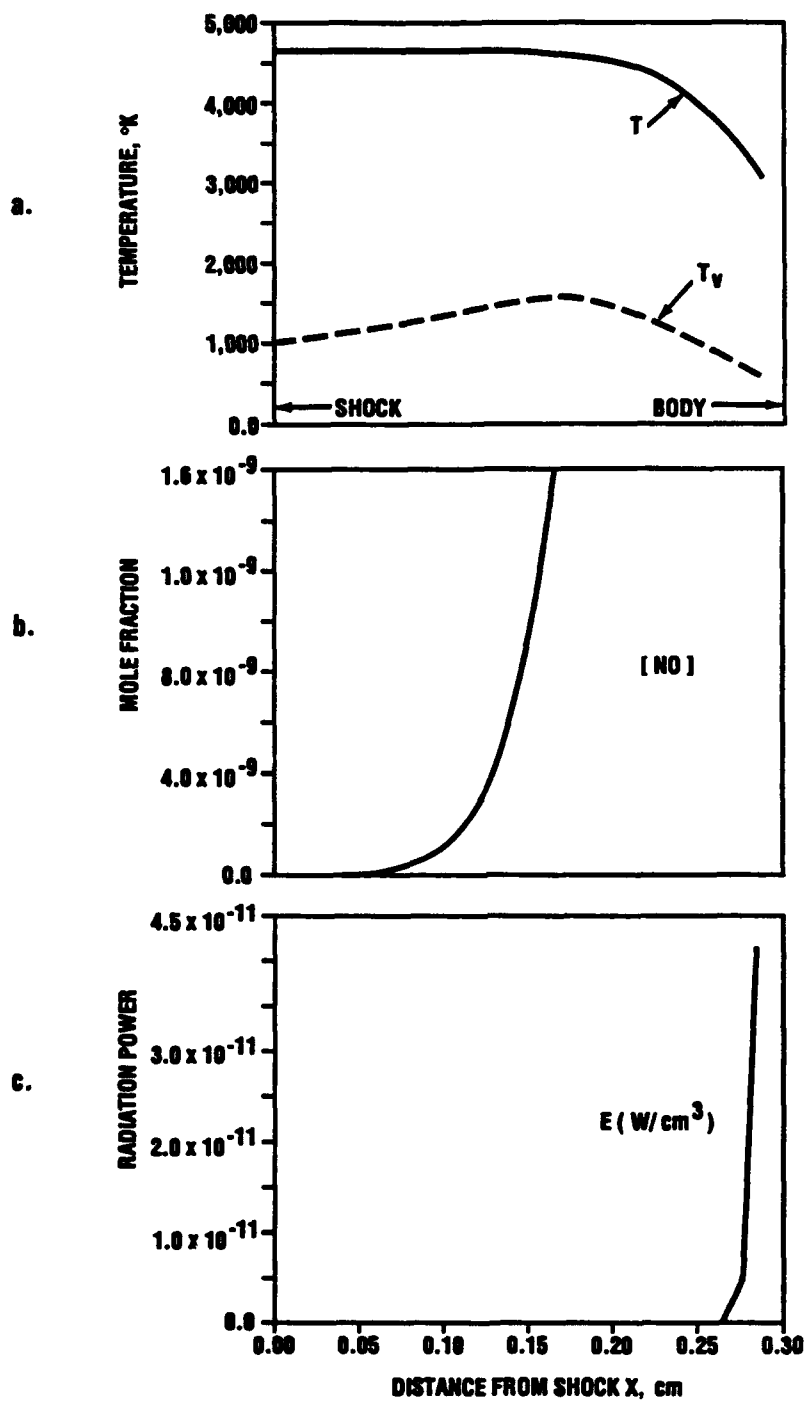
Figure A-3. Flowfield Conditions at 3 km/s, h = 50 km, r_n = 7.62 cm.

stream line with the comparable ones for the 1-D code. Examination of Fig. A-4 shows many features in common between the two sets of results, e.g., qualitative agreement in terms of translational and vibrational temperatures as well as distance from the shock at which the two temperatures equilibrate is shown. There are important distinctions evident from the figure as well. The modeling of the finite thickness of the shock with chemical reactions in the 2-D code shows that the shock temperatures as well as those in the shock layer are lower than the 1-D results. The curve labeled "TV AVG" represents the average of the individual molecular species' vibrational temperature in the flow. It is essentially that of N_2 since that species exists in the flow with the highest mass fraction, and can be directly compared to T_v for the 1-D, SPRAP data. The third temperature, T_e, is the electron temperature and observed not to equilibrate with the other two temperatures. Since T_e should be directly used in the computation of the population of excited state species in the radiation portion of the calculation (NEQAIR), an assessment of the degree it should be out of equilibrium is crucial. Its influence on the magnitude of T and T_v, however, is not likely to be large for the conditions used to produce these figures, because the fraction of energy in the flow tied up in electronic modes is relatively small.

Figure A-5 shows a comparison under the same free stream condition as Fig. A-4 for the mole fraction of O and NO formed in the shock stand-off region. Again, the two codes appear to be in reasonable agreement in spite of the modeling distinctions discussed in Section II.A.

Figures A-6 and A-7 show similar comparisons for a stronger shock condition. It corresponds to the fifth 1-D code run in Table A-1. In contrast to the results at 4.1 km/sec, 40 km altitude, here both codes show the trends of higher temperatures, faster temperature equilibration, and earlier onset of production and destruction mechanisms of NO. The production of NO, in contrast to weaker shock conditions, peaks substantially ahead of the boundary layer region. Figure A-7 shows, however, that the mole fraction of NO formed as predicted by 2-D code is about a factor of 2.75 higher than the 1-D code. A separate kinetics analysis (discussed in Section II.B) showed comparable agreement of NO concentrations when the chemical rate data used in the 2-D code was compared with the comparable subset used in the 1-D code. It is, therefore, likely that this difference is due to the fewer number of reaction (7 versus 31, see Table II-1) in the 2-D code. The missing reactions potentially are a source of destruction for NO and production of N_2^+ at the higher temperatures associated with the data in Fig. A-7. Since these flight conditions were not of primary interest to us, we noted this discrepancy in passing.
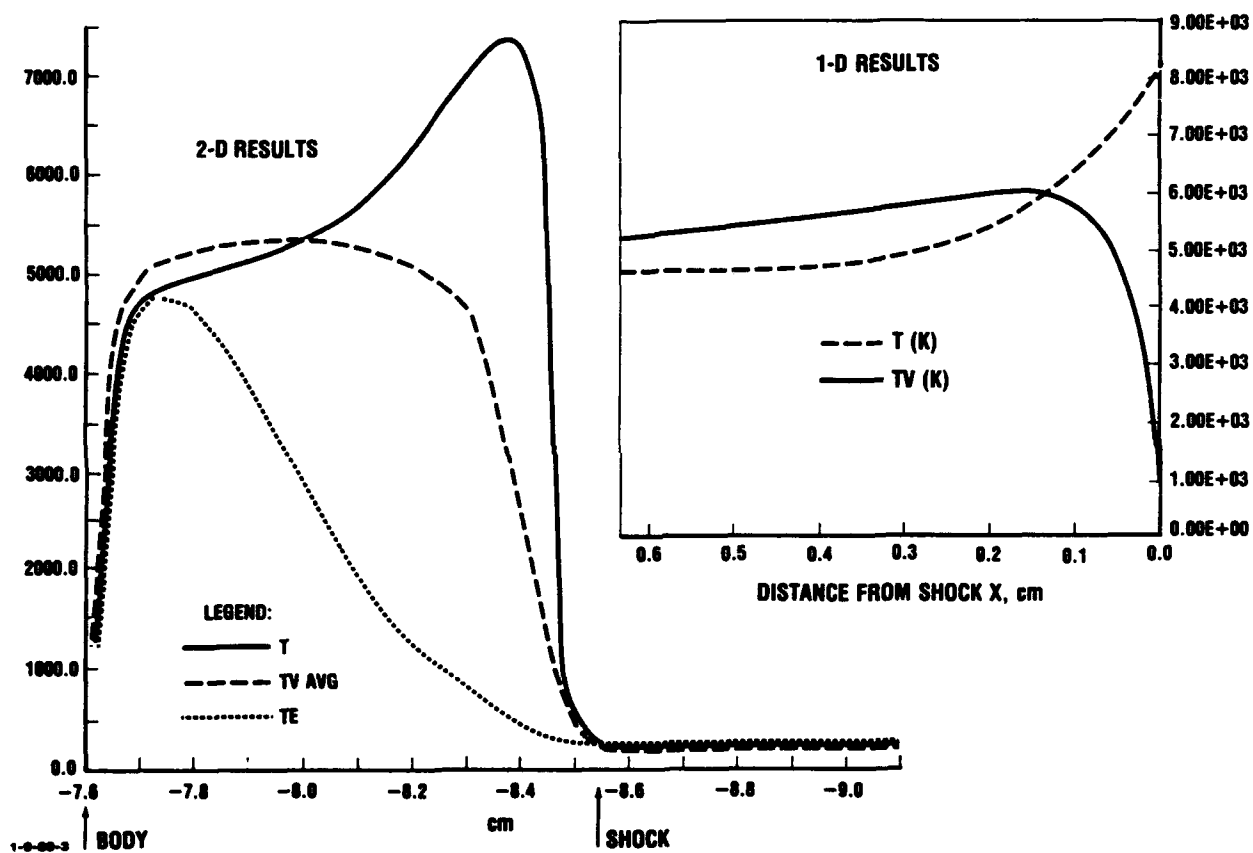
$v = 4.1$ km/sec, $h = 40$ km, $r_n = 7.62$ cm

Figure A-4. Comparison of Temperature Profiles Between SPRAP (1-D) and the 2-D codes at 4.1 km/sec, 40 km altitude, and a three-inch nose radius.
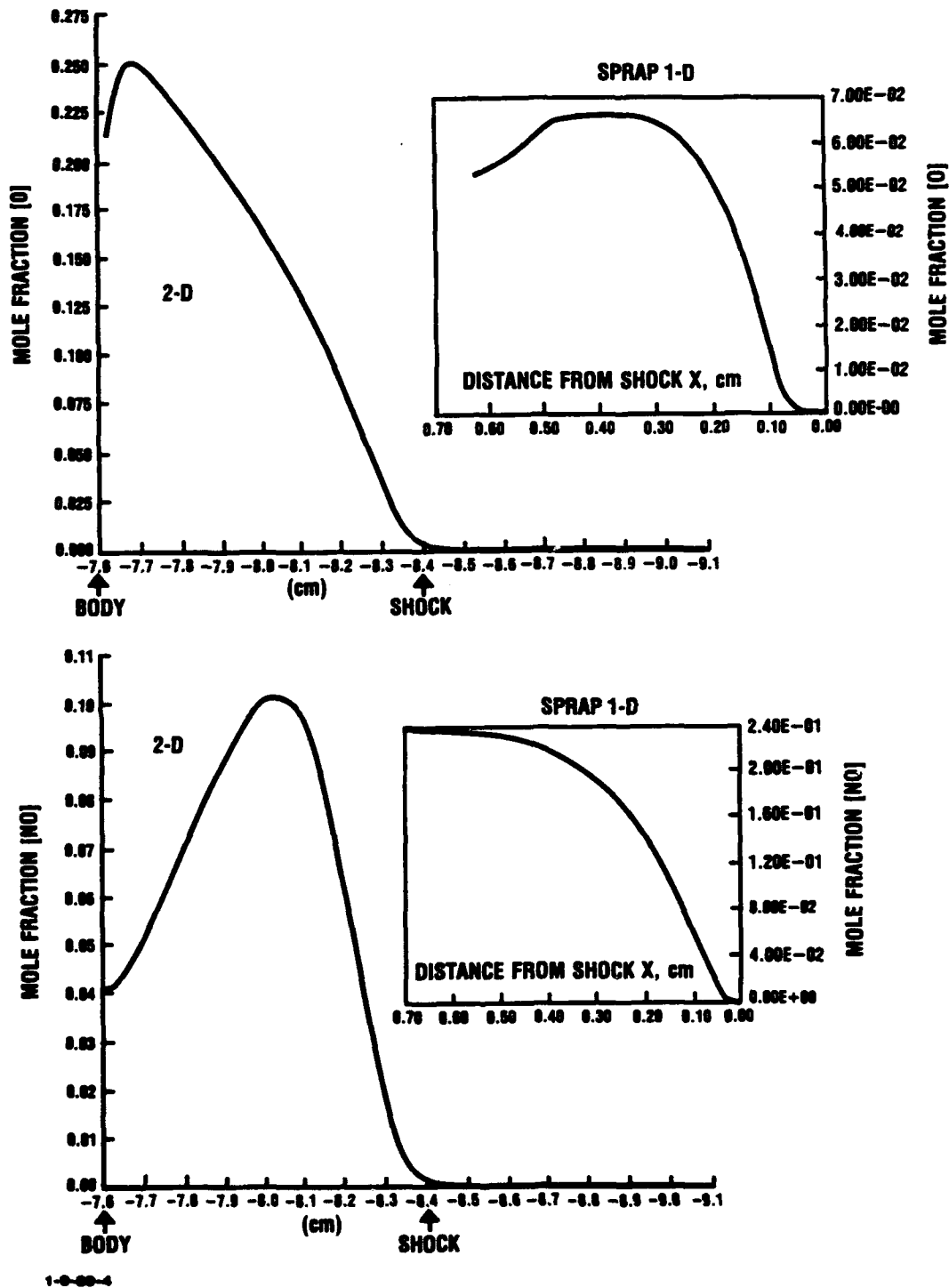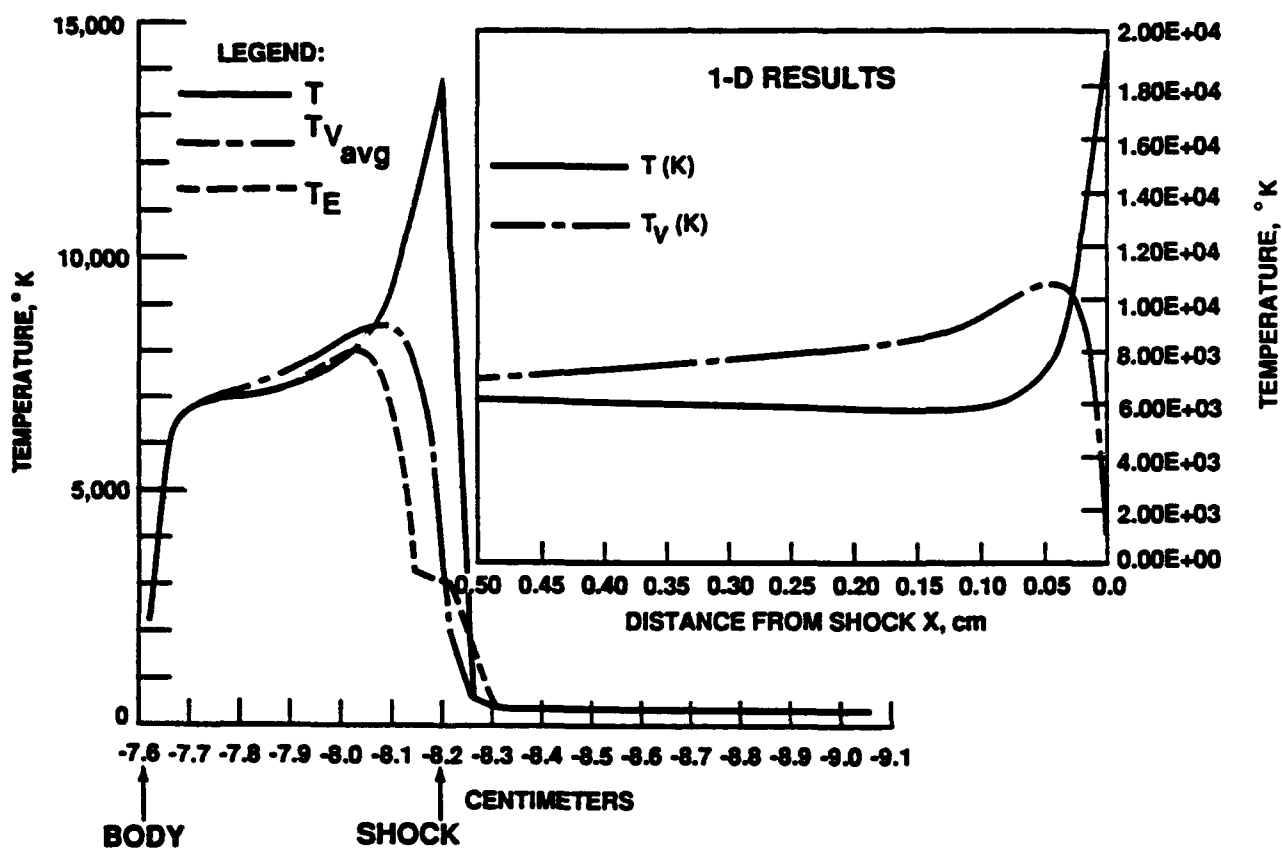
Figure A-5. Comparison of Species Mole Fraction Profiles Between the SPRAP (1-D) and the 2-D codes at v = 4.1 km/sec, h = 40 km, r_n = 7.62 cm.

Figure A-6. Comparison of Temperature Profiles Between the SPRAP (1-D) and the 2-D Codes at 6.3 km/sec, 40 km altitude, and a three-inch nose radius.
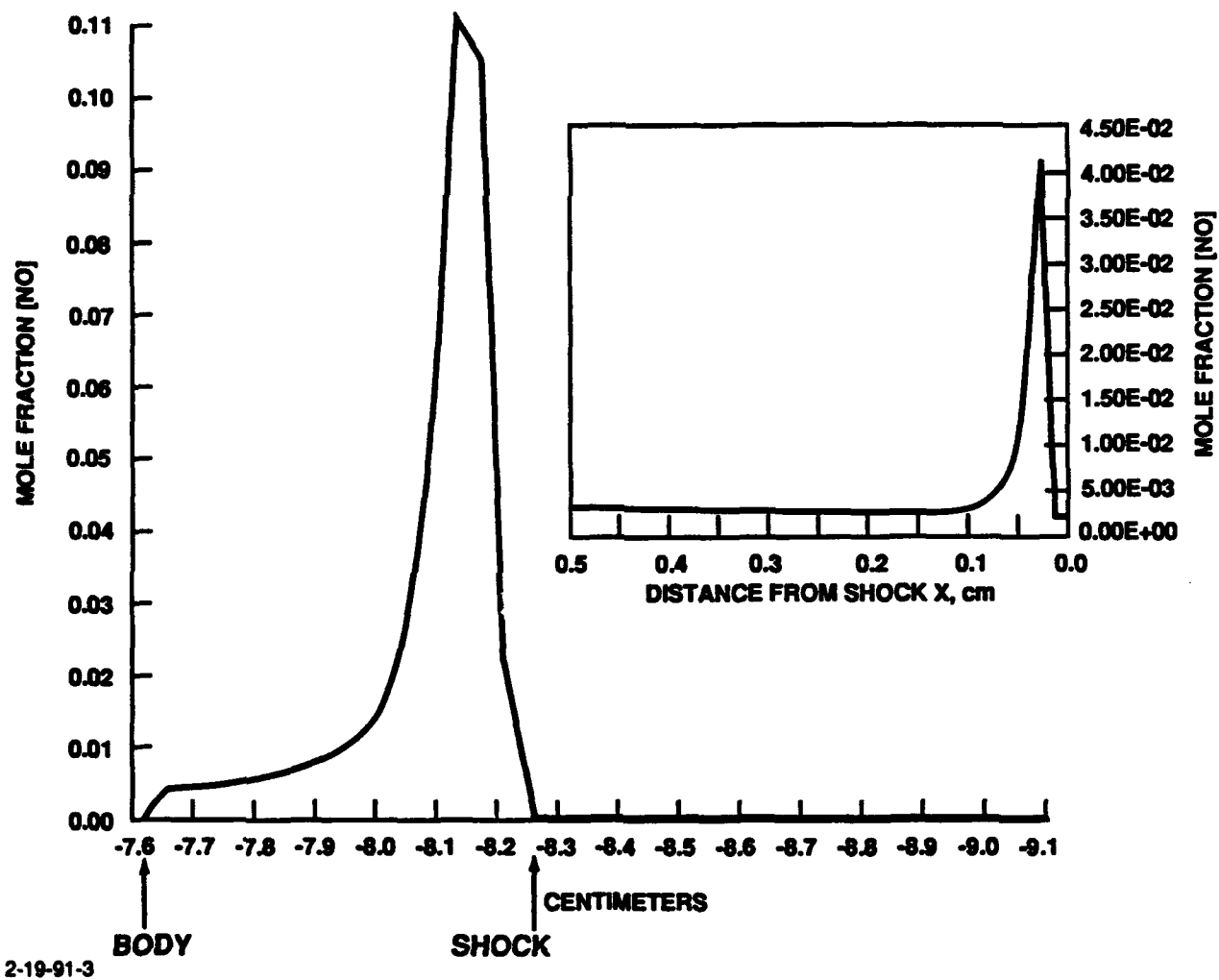
Figure A-7. Comparison of Species Mole Fraction Profiles Between the SPRAP (1-D) and the 2-D codes at V = 6.3 km/sec, h = 40 km, r_n = 7.62 cm.

2-19-91-3

A-12

In Table A-2 a comparison is given of the in-band radiance, calculated from 2250 to 2750Å using NEQAIR for the cases discussed in Figs. A-4 through A-7. Results are given for the in-band radiance when the electron temperature is used explicitly in NEQAIR to calculate the radiating state population ($T_e \neq T_v$) versus when it has been suppressed and set equal to the vibrational temperatures ($T_e = T_v$). The latter case corresponds more closely to the two-temperature model in the 1-D code. The effect of the electron temperature is seen to be significant under our conditions of primary interest, but less so at the faster speed.

Table A-2. Comparison of 1-D and 2-D Flowfield Code Radiation Predictions

Intensity ($W/cm^2sr\mu$)

Conditions	1-D	2-D ($T_e \neq T_v$)	2-D ($T_e = T_v$)
v = 4.1 km/sec h = 40 km m = 7.62 cm	0.39	0.022	0.28
v = 6.3 km/sec h = 40 km m = 7.62 cm	1.53	0.91	2.2

At the time that this work began it was not known which of the two 2-D results shown in Table A-2 was correct. The good agreement of shock tube data and theory discussed in Section II.D suggests that the last column is valid ($T_e = T_v$) and that the present electron temperature model is inadequate at speeds of about 4 km/sec or slower. The closer agreement at higher velocity is due to the onset of electron energies near 2.25 eV. Under those conditions an electron collides and vibrationally excites the N_2 molecule via a quasibound state of N_2^- to form a broad shape resonance with $2\Pi g$ symmetry. Hence, there is a dominant mechanism for vibrational and electronic energy mode exchanges. At a velocity of 4.1 km/sec the electron energies are closer to 0.5 eV. Since the background contribution to the resonance has not been modeled, the electron temperature does not equilibrate through vibrational-collisional exchange. Essentially, the only mechanism that may be available is through electron-translational exchange. The results presented in this paper, however, are obtained by equating the electron temperature to the vibrational temperature.

A-13

Because of the long computational times expected for these complex calculations involved in the 2-D code, the wavelength resolution required for convergence times of radiance values was examined. Table A-3 shows that 1Å resolution is adequate to calculate in-band radiances over a 500Å bandwidth with an accuracy of 3 percent, with a factor of two savings in time. This represents approximately 45 separate spatial grid point calculations along the stagnation stream line. Spectra presented here, regardless of the final spectrally averaged resolution quoted, were originally calculated at about 0.5Å resolution.

Table A-3. Convergence Considerations In Radiation Calculations

$\Delta\lambda$ (Å)	I (W/cm$^2\mu$sr)	CPU (sec)
0.1	0.08700	616
1.0	0.08423	346
10.0	0.041911	322

In spite of some of the boundary layer problems we encountered using the 1-D code, we found it to be an efficient tool for velocities typically greater than 3.5 km/sec at 40 km altitudes. Results derived from the SPRAP code, in support of the IST rocket experiment, were presented in Section II.E. Also, the boundary layer problems do not affect the shock tube calculations (STRAP), which were discussed in Chapter II.D.

REFERENCES, APPENDIX A

A-1.   R. Collins, A. Kim, R. Loda, and D. Levin, *An Examination of Hardbody Radiation from ICBMs*, Institute for Defense Analyses, IDA Paper P-2092, September 1988.

A-2.   E.E. Whiting, J.O. Arnold, and R.M. Reynolds, *Quant. Spectros., Radiat. Transfer*, 13, 837 (1973)

A-3.   C. Park, *Assessment of Two-Temperature Kinetic Model for Ionizing Air*, AIAA-87-1574.

APPENDIX B

COMPARISON OF SPECTRA AND ASSIGNMENT OF RADIATING SPECIES IN SHOCK TUBE MEASUREMENTS

APPENDIX B
COMPARISON OF SPECTRA AND ASSIGNMENT OF RADIATING SPECIES IN SHOCK-TUBE MEASUREMENTS

Spectral simulation work (Refs. B-1 and B-2), done at CUBRC/CALSPAN during the course of the shock-tube experiments, leads to some questions regarding the relative magnitude of the emission originating from the $O_2(B)$ state, compared to that from the NO(A) state. In this appendix, we present some spectra, calculated using NEQAIR, that have been deconvolved into their component species contributions. We also compare these to the CUBC/CALSPAN spectral simulation results, in an attempt to reconcile some of the differences observed.

In Fig. 1 of Ref. B-2 (which is given as Fig. B-1), a calculated spectrum, of the relative contributions of the NO gamma and the O_2 Schumann-Runge bands from 240 to 270 nm is presented. The CALSPAN calculation is valid under equilibrium conditions in the shock. We (IDA) were very interested in this result because it appeared to suggest that:

   (a) Our interpretation of the importance of the NO gamma bands relative to other sources might be in error, and

   (b) If we are underestimating the importance of O_2 (SR), then we may have overestimated the importance of NO as a result of the CFD codes potentially miscalculating the vibrational-electronic temperatures in the flowfield solution.

What follows here is a summary of the steps we have taken to elucidate the discrepancies and differences in our procedures (IDA versus CALSPAN). We find that we are in good agreement with the CUBRIC/CALSPAN results in terms of relative spectral assignments in the equilibrium portion of the shock. We also find that we cannot entirely resolve whether this agreement will hold in the peak, non-equilibrium radiation portion of the flow, without additional absolute intensity calibrated data for the UV wavelength regions where only the NO (gamma, beta) bands are contributing to the radiation.[1]

---

[1] For convenience we sometimes ignore the beta bands in the text discussion, although they were always included in our calculations. Dr. Wurster told us that he does not include them; however, we do not consider this to be significant because the beta bands are at least a factor of ten smaller in intensity than the gamma bands.
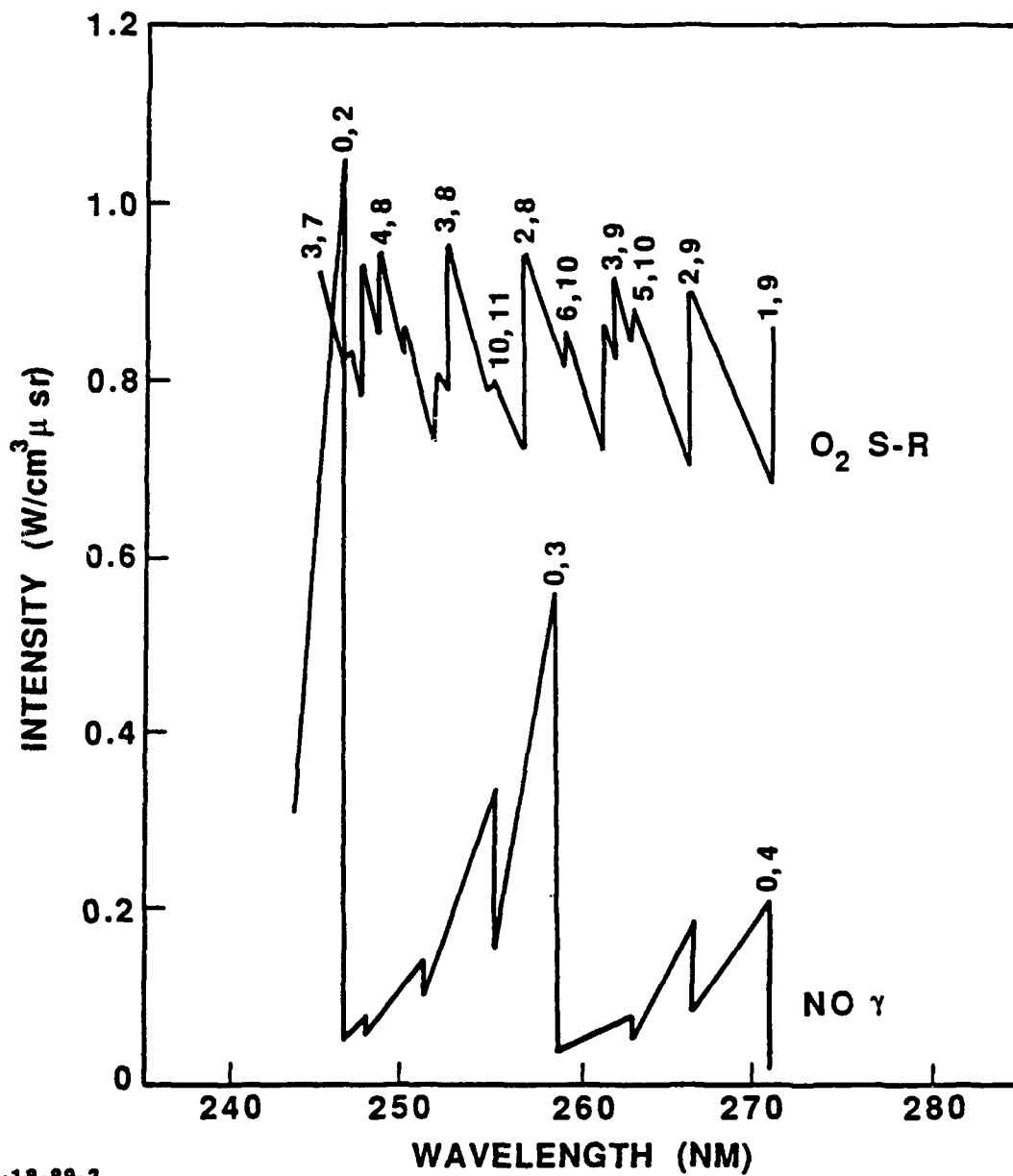
Figure B-1. Relative Contributions of NO γ and O₂ S-R Bands to Equilibrium Air Radiation at $V_s = 3.79$ km/sec, Altitude = 40 km. Calculation shown in CALSPAN 23 Dec. 1988 memo (Ref. B-2).

4-18-89-3

IDA's total, NO ($\gamma + \beta$) only, and O_2 (SR) only, spectral simulations are shown in Figs. B-2, B-3, and B-4. The spectra have been averaged over a 10Å bandwidth. The results shown in Figs. B-2–B-4 were calculated for bowshock input conditions of 40 km altitude, a nose radius of three inches, a velocity of 4.1 km/sec, and have been *spatially averaged over the bowshock stagnation stream line*. As can be seen from the figures, our total spectra is dominated by NO ($\gamma + \beta$) band radiation in contrast to Fig. B-1, which shows about a 5 to 1 relative enhancement of O_2 (SR) to NO(γ).

We next obtained the species concentrations and temperature that were used to calculate the equilibrium air radiation given in Fig. B-1, and input these values directly into NEQAIR to calculate the results shown in Figs. B-5 through B-7.

The results in Figs. B-5 through B-7 are calculated at a single spatial location, in contrast to those of Figs. B-2 through B-4. Figure B-5, compared with B-6 and B-7, is observed to be a composite of the two molecular radiators. Comparison of Figs. B-6 and B-7 shows a relative intensity of NO ($\gamma + \beta$) to O_2 (SR) of about .6 at 2700Å. Also, if one compares the maximum peak height of the O_2 (SR) to the NO ($\gamma + \beta$) spectra for wavelengths $\geq$ 2600Å a ratio of roughly 1.7 is obtained. Hence, we do not get the relative intensities shown in Fig. B-1, but the situation is much closer than the first set of comparisons, where the cool wall and boundary layer of the bowshock affect the results. When the above spectra are convoluted with the CALSPAN 260 nm filter, the O_2 (SR) contributions predominate, as can easily be seen in the figures. In Table B-1, our exact contributions as well as those of CALSPAN are given. Again, unlike their results, we do not see a factor of 4.5 enhancement of O_2 (SR) relative to NO ($\gamma + \beta$) even under equilibrium conditions using their species concentrations and temperature. The effect of the convolution to band radiance is to reduce the disagreement. The CALSPAN result can be compared to the measured total, and found to be within 20 percent agreement. The IDA total is roughly the same, but under-predicts the experiment.

We have no details regarding the program CALSPAN used to calculate the results in Fig. B-1, except that a Q-branch smearing technique was used, along with data from the high temperature equilibrium tables of Allen (AVCO/Everett Report No. 236).

.
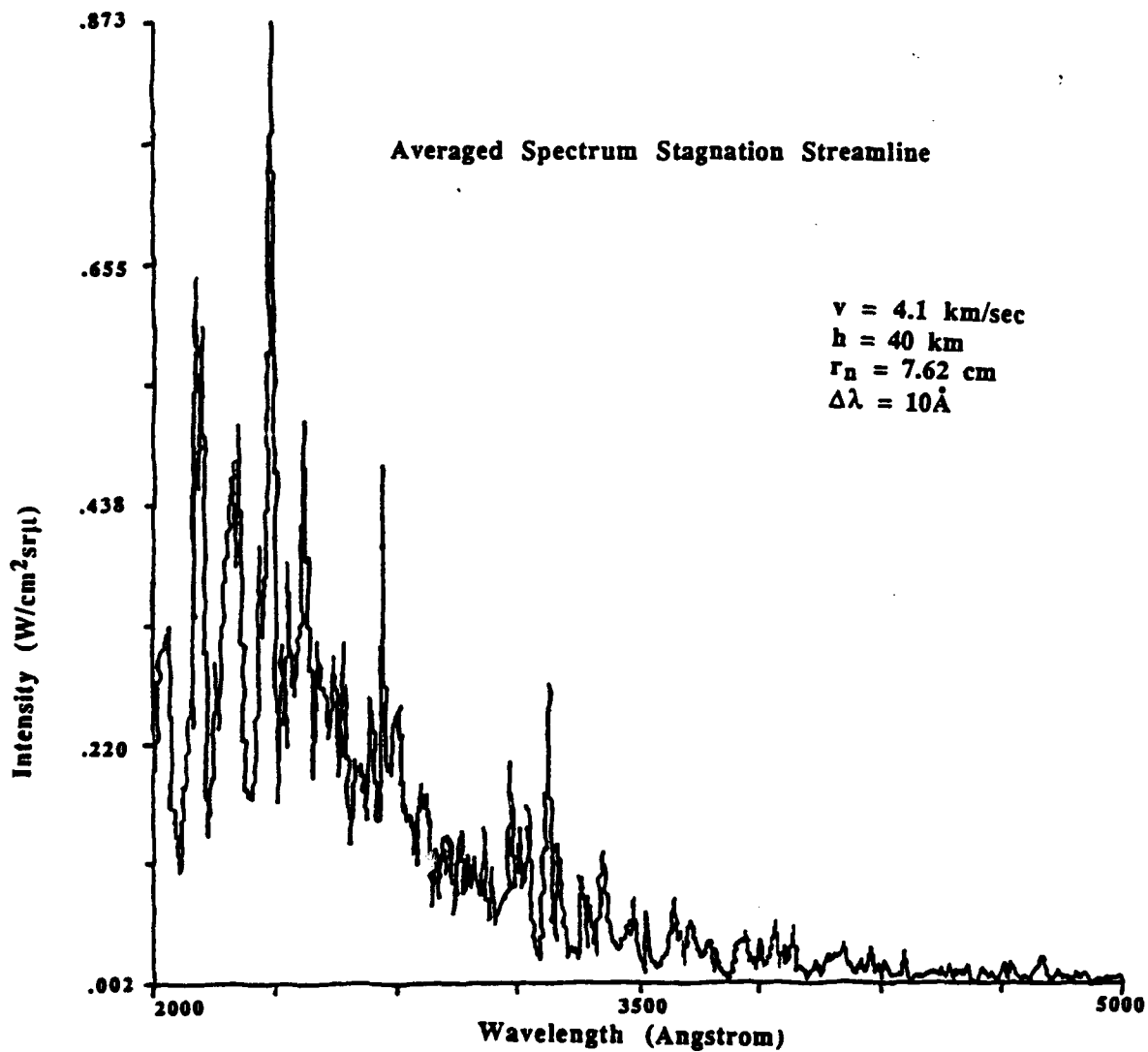
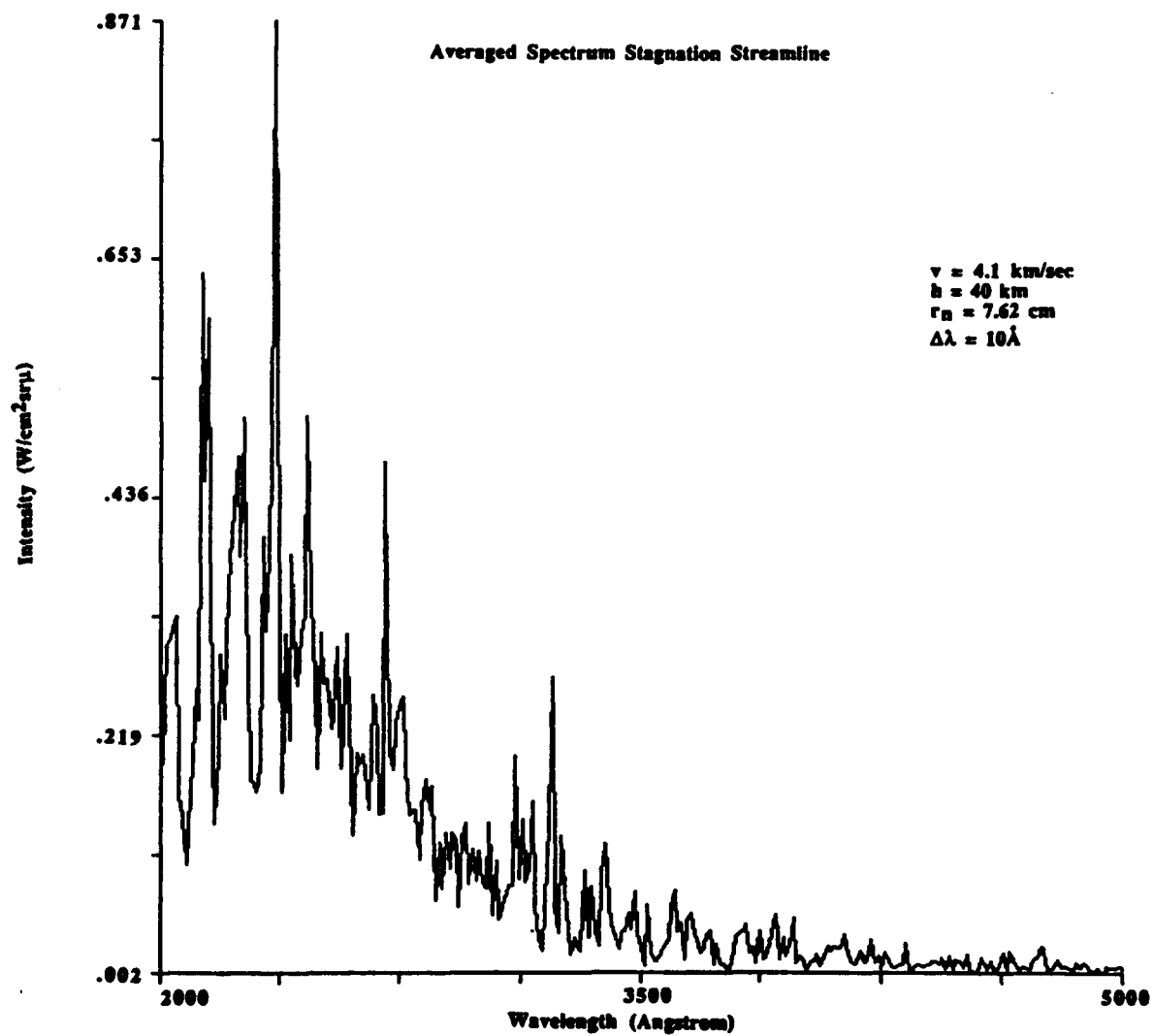**Figure B-2. Spectra With All Potential Radiating Species Included.**

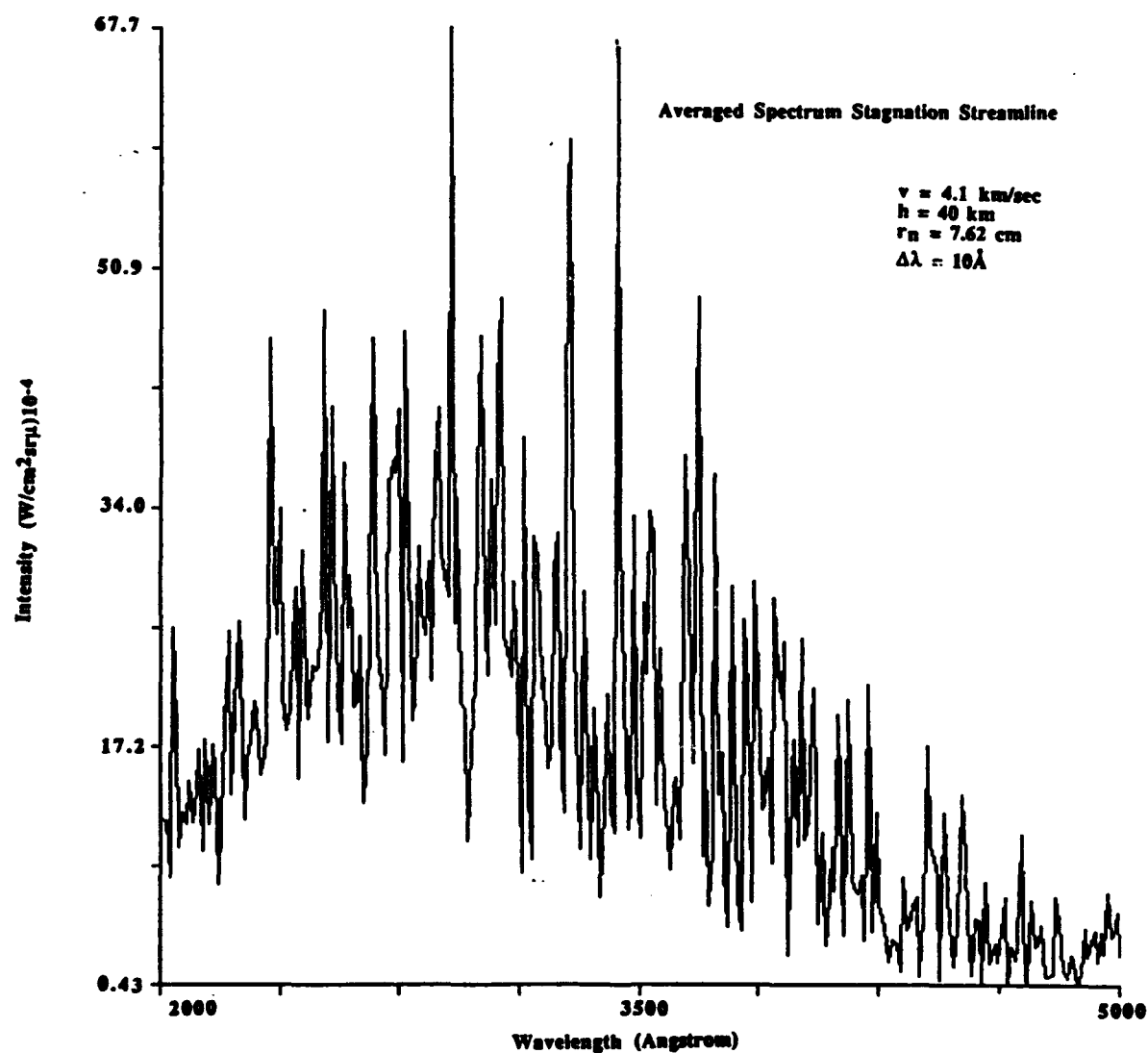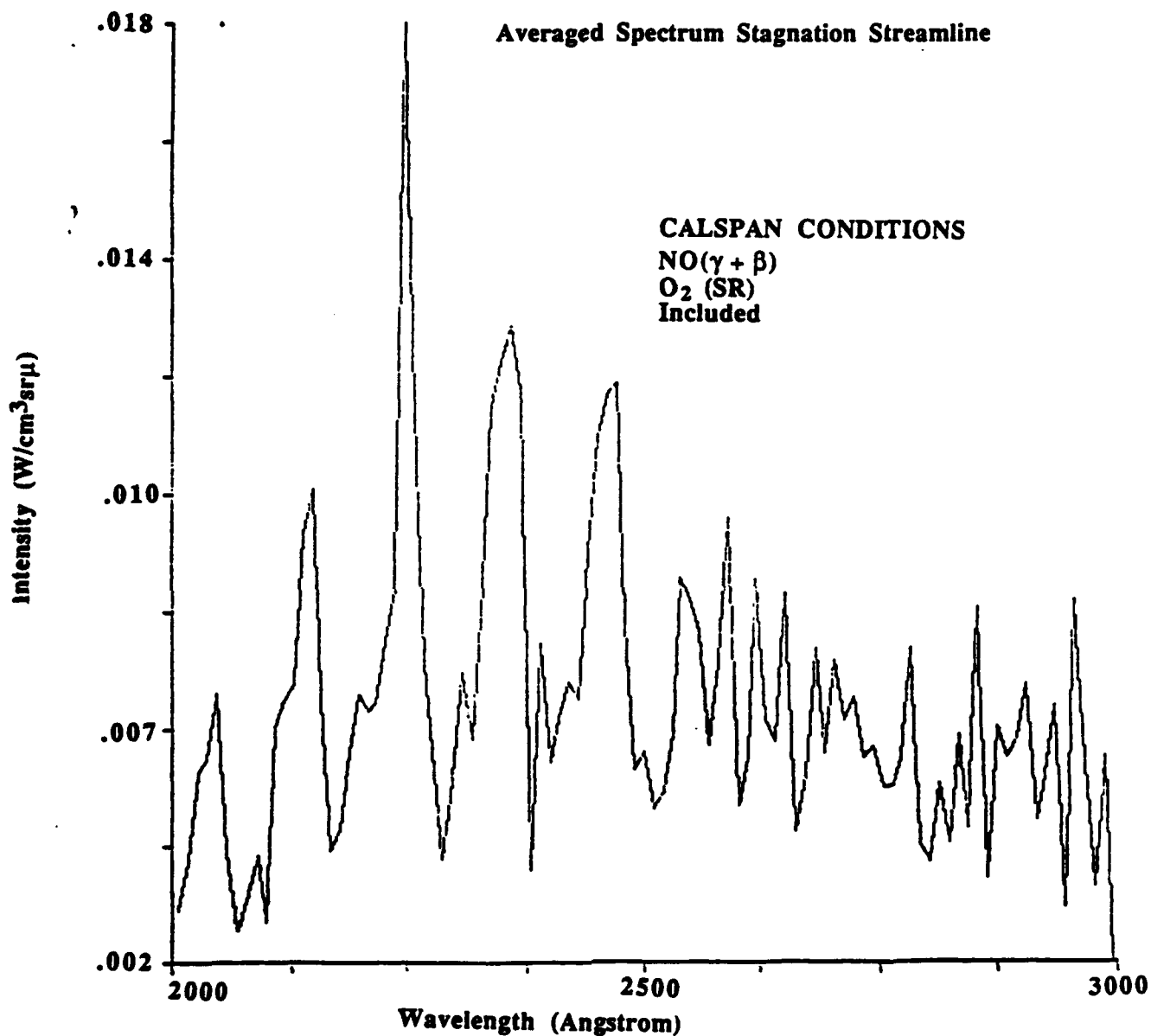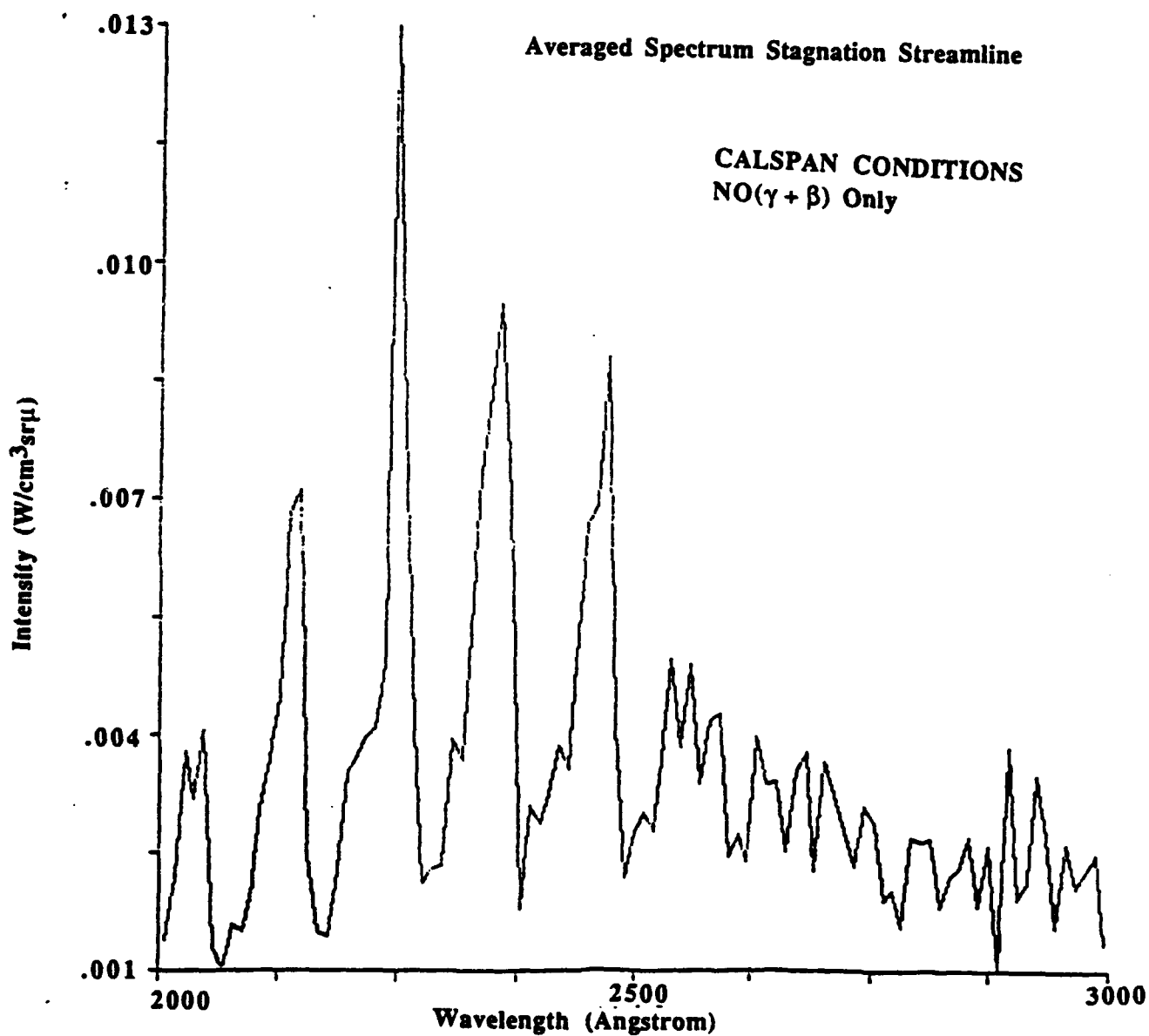Figure B-3. Spectra With Only NO ($\gamma + \beta$) Radiating Transitions Included.

Figure B-4. Spectra With Only O_2 (SR) Radiating Transitions Included.

Figure B-5. CALSPAN Conditions, Total Spectrum Calculated With NEQAIR.
T= 3890°K; [NO] ,[O$_2$], [O], [N], [N$_2$] are 3.0, 3.44, 22.3,
0.12046, 58.48 × 10^{16} molec/cc.

Figure B-6. CALSPAN Conditions, NO ($\gamma + \beta$) Transitions Only, Calculated With NEQAIR.
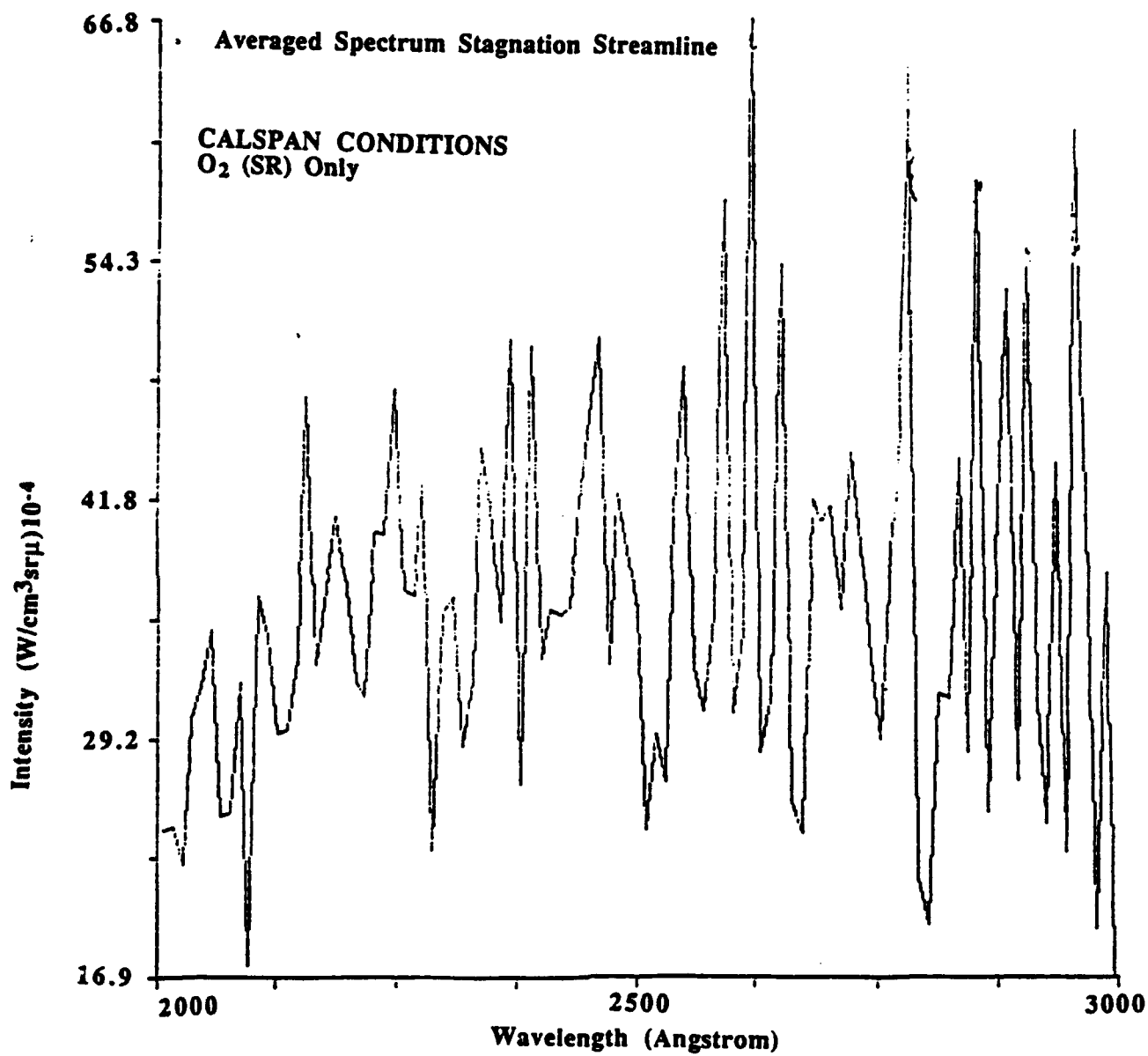
Figure B-7. CALSPAN Conditions, O_2 (S-R) Transitions Only, Calculated With NEQAIR.

B-11

Table B-1. Comparison of In-Band Relative Contributions[a]

| | CALSPAN | | IDA/Ames[b] |
	Experiment	Theory[c]	Theory
NO ($\gamma + \beta$)	–	3.2×10^{-6}	5.33×10^{-6}
O_2(SR)	–	1.45×10^{-5}	6.105×10^{-6}
Total	1.5×10^{-5}	1.8×10^{-5}	1.143×10^{-5}

[a] Intensity in W/cm^{3}sr (in the 260 nm band pass filter).

[b] Using NEQAIR with CALSPAN conditions.

[c] Results from CALSPAN/CUBRC memo of December 23, 1988.

Another potential source of discrepancy is the excitation mechanisms used to determine the upper electronic state populations. It is our understanding that the CALSPAN calculation uses a pure Boltzmann assignment to determine these populations. NEQAIR uses a series of collisional excitation mechanisms invoking the steady state approximation for NO modeled as a three-level system. Molecular oxygen is modeled in a different manner than NO in NEQAIR, due to curve crossings shown in Fig. B-8. Park considers the most likely mechanism for population of the $B^3 \Sigma_u^-$ state to occur through collisions of oxygen atoms in the ground electronic state, rather than through collisional excitation from lower electronic levels. Hence, using the principle of detailed balancing, and a probability of predissociation of one, he calculates the population of the $B^3 \Sigma_u^-$ state as

$$n_i = n_{iE} \frac{v}{v + A_{if}} \quad ,$$

(B-1)

where n_{iE} is the number density of the ith electronic state at equilibrium, A_{if} is the Einstein transition probability, and v is the collision frequency. For the temperature range of interest to us, v is on the order of 4×10^{12} and A_{if} is on the order of 10^8. Hence, $n_i \approx n_{iE}$, which implies that the above formulation is valid when there are enough collisions to be close to equilibrium. Another assumption which is also utilized in NEQAIR is that chemical equilibrium between the ground state O_2 and its dissociated products exists. From some sample conditions that have been examined (see case 1 of Table B-2), we
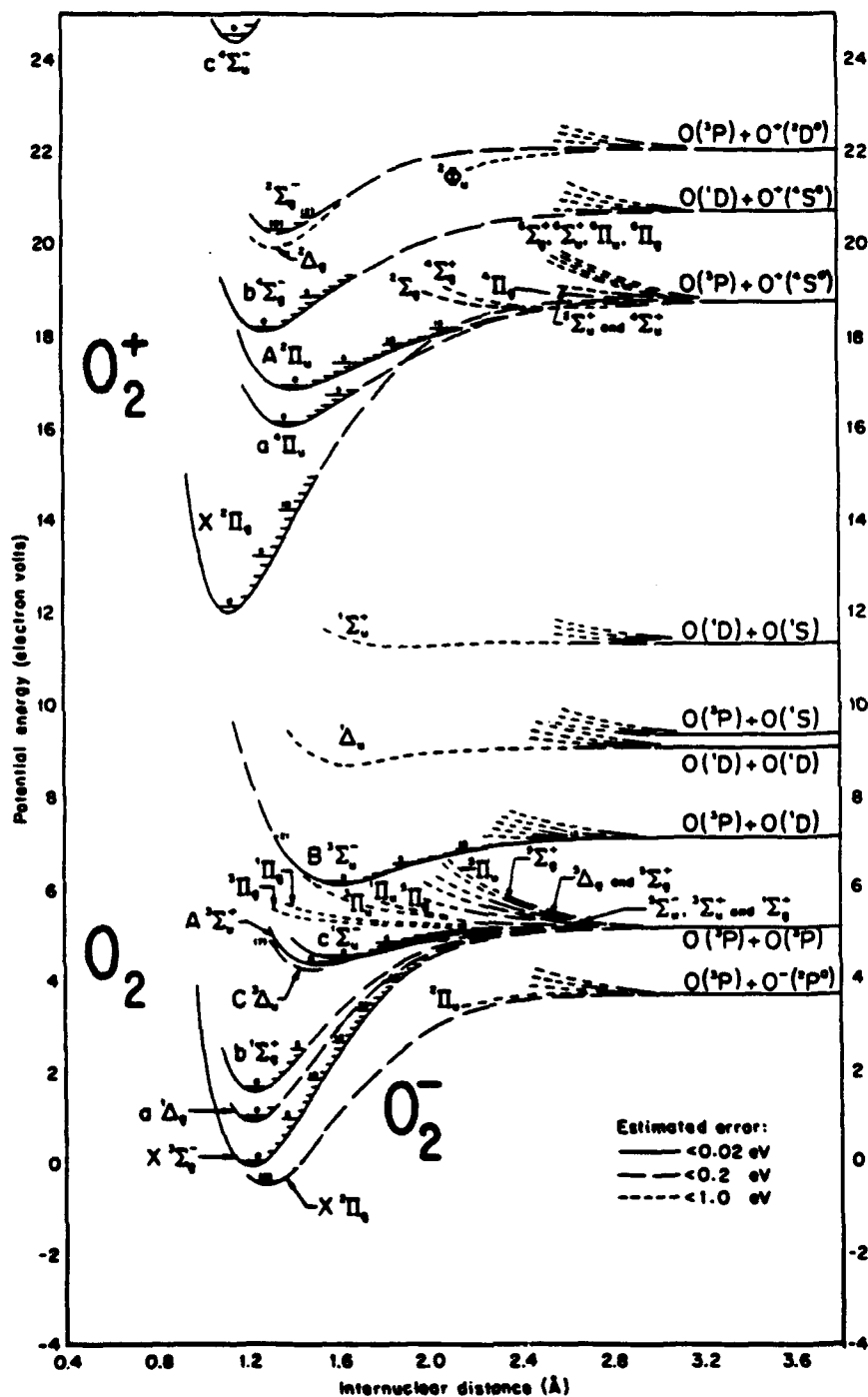
Figure B-8. Potential-Energy Curves for O_2, O_2^- and O_2^+ (Gilmore, 1964).

B-13

Table B-2 Excited State Populations

| NO(A) (molec/cm^3) | | O$_2$(B) (molec/cm^3) | | Keq | [O]^2/[O$_2$] |
QSSM	Equilibrium	QSSM	Equilibrium	(mole/cc)	(mole/cm^3)
Case 1: 2-D/NEQAIR for 40 km, 3.5 km/sec					
T = 4412°K, T$_v$ = 4761°K, location of peak radiation in the flow.					
1.401 × 10^{10}	1.781 × 10^{10}	2.39 × 10^8	1.079 × 10^{11}	5.8 × 10^{-5*}	9.6 × 10^{-8}
Case 2: CALSPAN/NEQAIR for 40 km, U$_S$ = 3.79 km/sec					
7.377 × 10^8	8.903 × 10^8	1.18 × 10^9	1.58 × 10^9	6.2 × 10^{-6}	2.4 × 10^{-6}

* Equilibrium constant for $O_2 \rightleftarrows O + O$ at $(T \cdot T_v)^{1/2}$.

found that these criteria are not always met. In that situation the implementation of Eq. (B-1) in NEQAIR produces populations which are much lower than the equilibrium values, which, in turn, would underpredict the O_2 (SR) contribution. Since the QSS equation implementations for N_2 and NO in NEQAIR were observed to produce near equilibrium populations in the spatial region of the bow shock where the radiation peaks, we have concerns that corrections may need to be added to the O_2 excitation portion of the code. For the CALSPAN conditions (case 2 of Table B-2) input into NEQAIR, it was observed, however, that the use of Eq (B-1) gave essentially Boltzmann results, since both chemical and thermodynamic equilibrium exists.

In spite of the differences that are shown in Table B-1, we asked ourselves how it would be possible to get factor of 2 to 3 agreement between experiment and SPRAP theory in the peak and equilibrium portions of the shock. To that end, we examined one of our closest corresponding STRAP runs at 3.81 km/sec, 40 km altitude. Figure B-9 shows a plot of the in-band radiance through the CALSPAN 260 nm filter as a function of location in the shock for the NO ($\gamma + \beta$) and O_2 (SR) band radiators, respectively. Apart from the magnitude difference, the figures illustrate that, with the present implementation of the Ames codes, the spatial characteristics of NO and O_2 radiation are very different. Table B-3 shows specific values taken from two spatial locations in Fig. B-9. The difference in relative magnitudes at the peak and at equilibrium may be due to the treatment of O_2 excitation to the B state presently modelled in NEQAIR.

Since we do not have absolute radiance data in a region where only a single species is radiating, we do not know whether Fig. B-9 is correct in the *peak* radiating portion of the shock (i.e., x = .98 cm). Unfortunately, this is the region of most importance for the

planned bow-shock rocket experiment. The CALSPAN calculations were not performed for this region, since their equilibrium model would not be applicable.
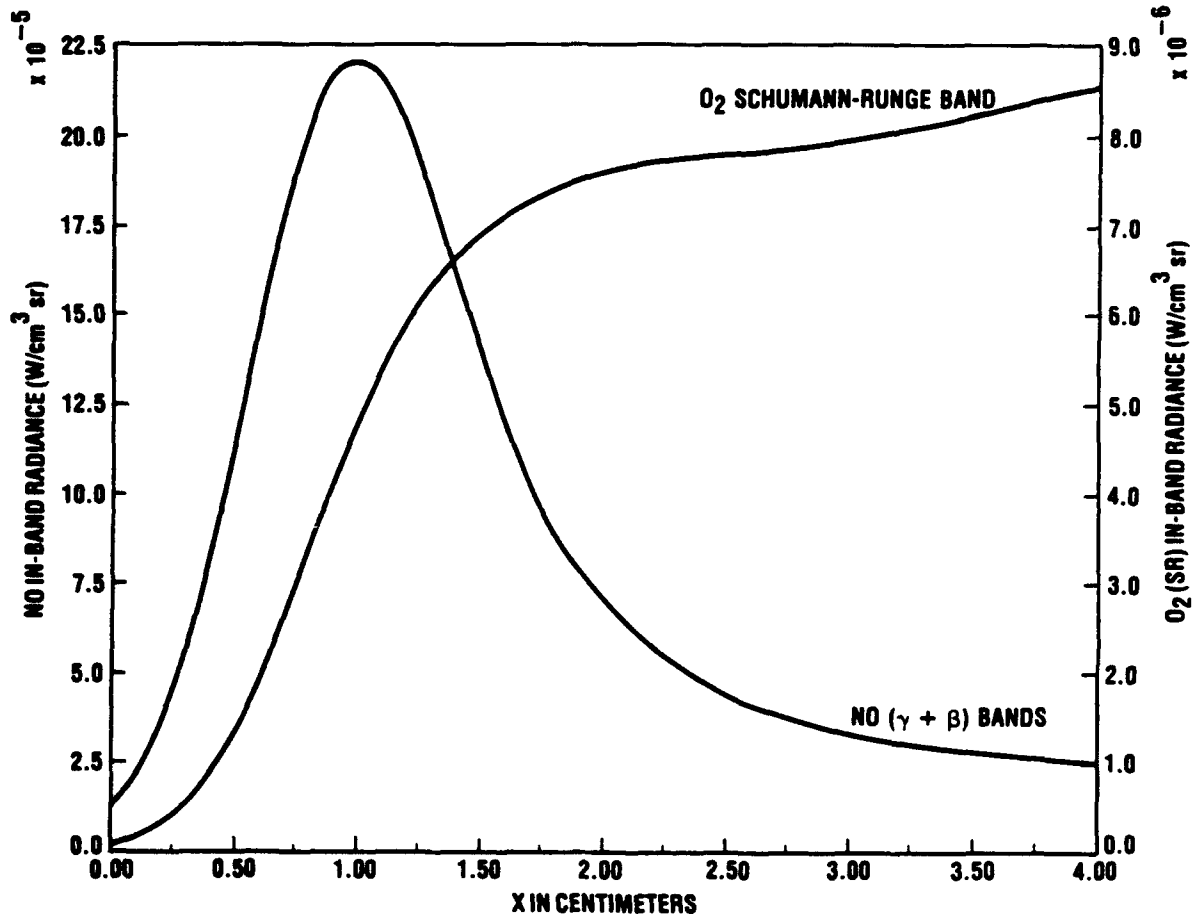
Figure B-9. STRAP Intensity In-Band for the CALSPAN 260 nm Filter at 3.81 km/sec, 40 km Altitude.

Table B-3. Factorization of STRAP 3.81 km/sec, 40 km Radiance Values

Distance along shock (cm)	Radiance (W/cm^{3}sr)		
	NO($\gamma + \beta$)	O$_2$ (SR)	Total
0.9622 (peak)	2.20×10^{-4}	4.64×10^{-6}	2.25×10^{-4}
3.909 (equilibrium)	2.49×10^{-5}	8.4×10^{-6}	3.33×10^{-5}

Therefore, we concentrated on rationalizing our STRAP run in the equilibrium portion of the shock with Fig. B-1. Table B-4 presents a summary of the relevant parameter values necessary to make this comparison. Examination of the top part of the table shows that the STRAP run predicts a factor of 9 more NO $(\gamma + \beta)$ radiation relative to the CALSPAN theory result, whereas the amount of O_2 (SR) radiation is in close agreement.

Concentrating, therefore, on the NO disagreement, we asked what are the possible sources? Examination of the effect of the spreading function on the absolute magnitude, presented earlier, showed that this is not a factor in the equilibrium portion of the shock. Differences in species concentrations, temperatures, and spectroscopic constants, for example, can account for a significant portion of the factor of 9 (in Table B-4) as seen below:

$$1.235 \quad \times \quad 2 \quad \times \quad 1.126 \quad \times \quad \chi \quad = \quad 9 \quad , \qquad \text{(B-2)}$$

factor due to   Boltzmann ρ spectroscopic
[NO]   factor ,

where the assumption has been made, and verified, that the QSS treatment is close to equilibrium. This implies a residual factor, χ, of 3.2 due to difference in Frank-Condon factors and lifetimes. The corresponding treatment for O_2 is

$$\frac{2}{3} \times 2 \times 1.126 \times \chi' = 0.933 \quad , \qquad \text{(B-3)}$$

where, in the O_2 case, $\chi' = 0.62$. Comparison of the columns entitled "Theory" and "IDA/Ames" of Table B-4 can give us the factors χ and χ'. Those are seen to be 1.9 and 0.68, respectively. The comparison of 0.68 with 0.62 is in excellent agreement. The factor of 1.9 reduces the 3.2 discrepancy of NO to 1.7 which, to us, appears to be an acceptable level of agreement.

Table B-4. Final Comparisons[a]

	CALSPAN		IDA/Ames[e]	STRAP
	Experiment	Theory[b]		
NO(g + b)	–	2.8×10^{-6}	5.33×10^{-6}	2.49×10^{-5}
O_2(SR)	–	9×10^{-6}	6.1×10^{-6}	8.40×10^{-6}
Total	1.5×10^{-5}	1.18×10^{-5}	1.14×10^{-5}	3.33×10^{-5}
T($^\circ$K)		3890[c]		4086
$[O_2]$[d]		0.039		0.026
[NO]		0.034		0.042
[O]		0.255		0.23
[N]		0.001		0.001
$[N_2]$		0.699		0.697
ρ (molec/cc)		8.7×10^{17}		9.8×10^{-17}

[a] All radiances are in W/cm^{3}sr in to 260 nm filter.

[b] These numbers which were presented at IDA on 17 Feb. differ from those given in Table II-19 and are the result of a more recent CALSPAN calculation.

[c] These are the same conditions given in Table II-18 and are common for the CALSPAN and NEQAIR with CALSPAN conditions.

[d] Species concentrations in mole fraction.

[e] Using NEQAIR with CALSPAN conditions for species concentrations and temperature.

REFERENCES, APPENDIX B

B-1.   W.H. Wurster, "Interim Results from the CUBRC Program on Non-Equilibrium
        Radiation from Shock-Heated Air," CALSPAN/CUBRC Memorandum for the
        record, 23 November 1988.

B-2.   W.H.Wurster and M.J. Williams, "Memorandum Addendum," CALSPAN/
        CUBRC Memorandum for the record, 23 December 1988.